



AFFIDAVIT

I declare that I have authored this thesis independently, that I have not used other than the declared sources/resources, and that I have explicitly indicated all material which has been quoted either literally or by content from the sources used. The text document uploaded to TUGRAZonline is identical to the present master's thesis.

Date

Signature

Abstract

The world's highest rate of forest cover loss is recorded in the tropics. Deforestation and forest degradation are the second largest source of anthropogenic greenhouse gases in the earth's atmosphere. Thus, especially countries located in the tropical domain are encouraged to participate in initiatives, such as the Reducing Emissions from Deforestation and Forest Degradation (REDD+) initiative, to reduce their greenhouse gas emissions effectively through decreasing deforestation and forest degradation. A forest monitoring system based on remote sensing satellite imagery can provide valuable information on intact and disturbed forest and can, therefore, support participating countries to successfully meet the needs of reporting requirements in the frame of forestry conservation initiatives. To assess the amount of forest cover loss, accurate reference data of the forest cover status is needed to assess the amount of forest cover loss. Considering tropical regions, the most important limitation of optical data is the influence of atmospheric conditions on image availability. Optical image time series in combination with data from all-time and all-weather radar sensors offer a great potential to provide reliable and gap-free information of the forest status. The aim of this thesis is to evaluate the added value of the combined use of optical Sentinel-2 and Landsat 8 and synthetic aperture radar (SAR) Sentinel-1 image time series to improve forest mapping in humid tropical regions. To do so, the performance of different approaches, based on either optical or SAR time series data as well as their combination, to generate a forest cover status map are conducted and evaluated. Maximum Likelihood and Random Forest classifier are applied to perform supervised classification, and results are compared. To test the methods transferability, the forest mapping approach producing the most accurate result in Peru is applied to a second study area in Gabon. Results show that a combined use of optical and SAR image time series improves forest mapping accuracies in humid tropical regions, indicating that SAR data is suitable to compensate limitations of optical data.

Zusammenfassung

Die weltweit höchste Verlustrate an Waldbedeckung wird in den Tropen verzeichnet. Da Entwaldung und Walddegradation die zweitwichtigste Quelle anthropogener Treibhausgase in der Erdatmosphäre sind, werden insbesondere die Länder in der tropischen Klimazone ermutigt, sich an Initiativen, wie z.B. der „Reducing Emissions from Deforestation and Forest Degradation“ (REDD+) Initiative zu beteiligen. Diese verfolgt das Ziel den Einfluss von Entwaldung und Walddegradation auf die Treibhausgasmenge in der Erdatmosphäre zu vermindern. Ein Waldmonitoringsystem auf der Grundlage von Satellitenbildern kann wertvolle Informationen über intakte und degradierte Waldflächen bereitstellen und dadurch die teilnehmenden Länder bei der Berichterstattung im Rahmen von REDD unterstützen. Um das Ausmaß des Waldverlustes beurteilen zu können, sind akkurate Referenzdaten der Ausdehnung der Waldfläche erforderlich. Die größte Einschränkung, welche das Nutzungspotential optischer Satellitenbilder einschränkt, ist der ganzjährig hohe Bewölkungsgrad in humiden tropischen Regionen. Die Verwendung von optischen Satellitenbildzeitreihen sowie Daten von Radarsensoren, welche nicht von Bewölkung beeinflusst werden, bietet ein großes Potential, ungeachtet von der Bewölkung zuverlässige und lückenlose Informationen über den Waldstatus zu generieren. Ziel dieser Arbeit ist die Bewertung der Eignung der Kombination optischer Sentinel-2 und Landsat 8, sowie „synthetic aperture radar“ (SAR) Sentinel-1 Satellitenbildzeitreihen zur Verbesserung der Waldkartierung in tropischen Regionen. Getestet werden unterschiedliche Kartierungsansätze, welche zum einen nur auf Zeitreihen optischer oder SAR Daten und zum anderen auf einer Kombination von Datenzeitreihen beider Sensoren beruhen. Für die Klassifikation werden sowohl der Maximum Likelihood als auch der Random Forest Klassifikator herangezogen und die Ergebnisse verglichen. Um die Übertragbarkeit der Methoden zu testen, wird der Ansatz der Waldkartierung, der für Peru das Ergebnis mit der höchsten Genauigkeit liefert, auf ein zweites Untersuchungsgebiet in Gabun angewendet. Die Ergebnisse zeigen, dass eine kombinierte Verwendung von optischen und SAR-Bildzeitreihen die Genauigkeit der Waldkartierung in tropischen Regionen verbessert, woraus abgeleitet werden kann, dass sich SAR Daten dazu eignen, Einschränkungen der optischen Daten zu kompensieren.

Content

Abstract	i
Zusammenfassung	ii
1 Introduction	1
1.1 Thesis Background	1
1.2 Study Objectives	3
2 State of the Art	5
2.1 Characteristics and Limitations of Satellite Data Time Series.....	5
2.1.1 Optical Time Series Data	5
2.1.2 SAR Time Series Data	6
2.2 Optical and SAR Data Combination Approaches.....	8
2.3 Multi-temporal Image Classification	9
2.3.1 Input Features	9
2.3.2 Classification Algorithms.....	10
2.4 Tropical LCLU and Forest Mapping Applications	13
3 Study Areas	16
3.1 Peru.....	16
3.2 Gabon	18
4 Data Source	19
4.1 Sentinel Data	19
4.1.1 Sentinel-1	19
4.1.2 Sentinel-2	20
4.2 Landsat 8.....	22
4.3 Validation Data Sets	23
5 Applied Methodology	26
5.1 Data Pre-processing	28

5.1.1	Optical Data.....	28
5.1.2	SAR Data.....	30
5.2	Training Data Selection.....	31
5.3	Tropical Forest Mapping Approaches.....	32
5.3.1	Optical Time Series Approach.....	32
5.3.2	SAR Time Series Approach.....	36
5.3.3	Combined Optical-SAR Time Series Approach.....	36
5.4	Accuracy Assessment.....	37
6	Results and Discussion	39
6.1	Peruvian Study Area.....	39
6.1.1	Data Pre-Processing	39
6.1.2	Training Sample Selection and Evaluation.....	44
6.1.3	Forest Mapping Results.....	50
6.2	Gabonese Study Area.....	61
6.2.1	Data Pre-processing	61
6.2.2	Training Sample Selection and Evaluation.....	63
6.2.3	Forest Mapping Results.....	66
7	Conclusion.....	69
	References.....	72

List of Figures

Figure 3-1: Peruvian area for forest mapping.....	16
Figure 3-2: Gabonese study area for forest mapping	18
Figure 4-1: Sentinel-2 band characteristics (Fletcher, 2012).....	21
Figure 4-2: Comparison of Landsat 7, Landsat 8 and Sentinel-2 band characteristics (Source: https://landsat.gsfc.nasa.gov/sentinel-2a-launches-our-compliments-our-complements/).....	23
Figure 4-3: Validation data set for accuracy assessment for the Peruvian study area.....	24
Figure 4-4: Validation data set for accuracy assessment for the Gabonese study area	25
Figure 5-1: Workflow diagram of the applied approaches.....	27
Figure 5-2: Schematic diagram of the result-based approach	33
Figure 5-3: Classification example showing a forest regeneration pattern	34
Figure 6-1: Results of atmospheric correction and cloud-masking of S2 data (10.03.2016; R: NIR, G: red, B: green): (a) Level 1C TOA, (b) Level 2A BOA. Both images have the same look up table stretch (black pixels: cloud mask)	39
Figure 6-2: Comparison of Sentinel-2 and Landsat 8: (a) prior and (b) after geometric adjustment	40
Figure 6-3: Sentinel-1 pre-processing: (a) ingested image, (b) converted to gamma naught and speckle filtering (Modified Frost filter), (c) multi-temporal filtered and orthorectified image.....	41
Figure 6-4: S1 (12.03.2016) speckle noise reduction: (a) ingested image (a) image filtered with modified Frost filter, (b) image filtered with the multi-temporal filter and orthorectification.....	42
Figure 6-5: S1 (a) mono-temporal backscatter image (12.03.2016) and temporal metrics: (b) minimum, (c) maximum, (d) mean, (e) median, (f) standard deviation.....	43
Figure 6-6: Examples of training samples	47
Figure 6-7: Feature spaces with land use data considering B12 combined with B2, B3, B4, B5, B8a, B11	49
Figure 6-8: Example forest/non-forest map for a subset of the study are: (a) input not radiometrically calibrated, (b) input relative calibrated, (c) S2 image from 22.10.2015 (R: SWIR1, G: NIR, B: red), (d) Esri basemap (World View 02, 20.06.2015).....	51
Figure 6-9: Forest/non-forest map of the L8 scene from 25.03.2015: (a) L8 image (R: NIR, G: red, B: green), (b) forest/non-forest map of S2 10.03.2016, (c) input not calibrated, (d) input calibrated	51
Figure 6-10: Temporal median of the red band (red: no-data areas)	54
Figure 6-11: Temporal median of the blue band of a subset of the study area (black areas: no-data).....	54
Figure 6-12: Subset of forest status map produced with S1 temporal statistics: (a) S2 10.03.2016 (R: SWIR1, G: NIR, B: red), (b) S1 temporal mean 03/2015-03/2016, (c) forest status map	58
Figure 6-13: Final forest status map of the Peruvian study area	60
Figure 6-14: Examples of optical L8 and S2 data available for forest mapping.....	62
Figure 6-15: Temporal median of the red band (subset of the Gabonese study area)	63
Figure 6-16: Examples of training samples for each LU class	65
Figure 6-17: Forest status maps of the study: (a) optical approach, (b) combined approach, (c) S2 02.04.2017.....	67
Figure 6-18: Forest mapping results for a subset of the study area: (a) temporal median of the red band, (b) optical approach, (c) combined approach	67

Figure 6-19: Classification results over the plantation in the southeast part of the study area: (a) S1 image 26.12.2016, (b) L8 06.03.2017, (c) optical data-based approach, (d) combined data-based approach..... 68

List of Tables

Table 1-1: Objects of investigation within the development of the forest mapping approach .	4
Table 2-1: Radar band characteristics (Lillesand et al., 2015)	7
Table 2-2: Most common multi-temporal classification algorithms.....	11
Table 3-1: Forest definitions used in the EOMonDis project.....	16
Table 4-1: Key characteristics of the Sentinel-1 mission (Torres et al., 2012)	19
Table 4-2: Key characteristics of the Sentinel-2 mission (Drusch et al., 2012).....	21
Table 4-3: Key characteristics of the Landsat 8 mission (Roy et al., 2014).....	22
Table 5-1: Classes of the scene classification map (Mueller-Wilm, 2017).....	28
Table 6-1: Classification key and number of training samples per LU class.....	44
Table 6-2: Separability JMD S2 10.03.2016.....	48
Table 6-3: Separability analysis using different band combinations.....	48
Table 6-4: Separability measure with all bands.....	48
Table 6-5: Separability analysis of the classes forest2 and plantation using different band combinations	50
Table 6-6: Accuracy measures and their 95% confidence interval of the optical result-based approach using ML and RF classifier	53
Table 6-7: Accuracy measures and their 95% confidence interval of the optical data-based approach using ML and RF classifier	56
Table 6-8: Accuracy measures and their 95% confidence interval of the SAR data-based approach using RF classifier	57
Table 6-9: Overview of the tested combined optical-SAR approaches.....	58
Table 6-9: Accuracy measures and their 95% confidence interval of the combined data-based and result-based approaches	59
Table 6-10: Classification key and number of training samples per land use class	63
Table 6-11: Accuracy measures and their 95% confidence interval of the optical and combined data-based approaches.....	66
Table 0-1: Acquired Sentinel-1 Scenes	84
Table 0-2: Acquired Sentinel-2 Scenes.....	85
Table 0-3: Acquired Landsat 8 Scenes	85
Table 0-4: Acquired Sentinel-1 Scenes.....	86
Table 0-5: Acquired Sentinel-2 Scenes.....	86
Table 0-6: Acquired Landsat 8 Scenes	87

List of Acronyms

ALOS	Advanced Land Observing Satellite
BOA	Bottom-Of-Atmosphere
COP	Conference of Parties
DEM	Digital Elevation Model
ESA	European Space Agency
EO	Earth Observation
EOMonDis	Bringing Earth Observation Services for Monitoring Dynamic Forest Disturbances to the Users
ETM+	Enhanced Thematic Mapper Plus
FAO	Food and Agricultural Organization
FMask	Function of Mask
GOFC-GOLD	Global Observation of Forest Change and Land Cover Dynamics
GLCM	Grey-level Co-occurrence Matrix
IPCC	Intergovernmental Panel on Climate Change
JMD	Jeffries-Matusita Distance
JR	Joanneum Research
LCLU	Land Cover/Land Use
ML	Maximum Likelihood
MODIS	Moderate-resolution Imaging Spectroradiometer
MSI	Multi Spectral Instrument
NDSI	Normalized Difference Snow Index
NDVI	Normalized Difference Vegetation Index
OA	Overall Accuracy
OLI	Operational Land Imager
PA	Producer Accuracy
PALSAR	Phased Array type L-band Synthetic Aperture Radar
REDD	Reducing Emissions from Deforestation and Forest Degradation
RF	Random Forest
SAR	Synthetic Aperture Radar

SIRS	Systèmes d'Information à Référence Spatiale
SRTM	Shuttle Radar Topography Mission
TM	Thematic Mapper
TOA	Top-Of-Atmosphere
UA	User Accuracy
UNFCCC	United Nations Framework Convention on Climate Change
USGS	U.S Geological Survey
VHR	Very High Resolution
ZD	Zero Deforestation

1 Introduction

1.1 Thesis Background

In 2015, 3.99 billion hectare (ha) was covered with forests, which corresponds to approximately 30.6% of the entire earth's terrestrial surface. Almost half of this area (1.77 billion ha) is located in the tropical domain (FAO, 2015; Keenan et al., 2015). Furthermore, the tropics are the climate domain recording the highest loss of forest cover. According to the Food and Agricultural Organization (FAO), tropical forest area decreased by an average of 5.52 million hectares per year between 2010-2015 (FAO, 2015). Causes for deforestation and forest degradation are numerous and vary not only geographically, but also on different spatial scales (FAO, 2015). Generally, they can be divided into direct (proximate) drivers and indirect (underlying) drivers (Kissinger et al., 2012). The proximate driver with the greatest impact is agricultural expansion (Hosonuma et al., 2012). According to Hosonuma et al. (2012), agricultural expansion accounts for about 80% of global deforestation. Besides, mining activities, urban expansion, infrastructure expansion, timber extraction and logging function as direct drivers. Underlying causes of deforestation and forest degradation are for example population growth, national policies, poor governance, lack of land-tenure security, poverty and global commodity market competition (Kissinger et al., 2012). The major problem is that especially underlying drivers rarely appear in isolation. Rather, they build complex synergies and reinforce proximate drivers of deforestation and forest degradation (Geist and Lambin, 2002).

Considering the facts that tropical rainforests are native to at least two-third of the global biodiversity and that they are essential for the quality of life of local communities by providing economic goods and ecosystem services (Gardner et al., 2009), it is obvious that deforestation and forest degradation are issues of great relevance. Furthermore, tropical forests supply huge carbon stocks and sinks, hence playing a crucial role in the global carbon cycle (Pan et al., 2011). According to van der Werf et al. (2009) deforestation and forest degradation account for 6-17% of the global anthropogenic CO₂ emissions, making it second in the ranking of anthropogenic sources of greenhouse gases in the earth's atmosphere. Thus, it is indisputable that forest loss contributes to global climate change. To overcome this issue, the United Nations Framework Convention on Climate Change (UNFCCC) launched the Reducing Emissions from Deforestation and Forest Degradation (REDD) initiative at the Conference of Parties (COP) in Montreal in 2005. Primary idea of REDD is to financially compensate developing countries that are reducing their greenhouse gas emissions effectively through decreasing deforestation and forest degradation (Parker et al., 2009; Scholz and Schmidt, 2008). At the COP in Bali 2007 the REDD initiative was extended (REDD+) by the integration of conservation and enhancement of forest carbon stocks as well as sustainable forest management (Parker et al., 2009; UNFCCC, 2007). Within the last view years the awareness of the importance of the reduction of forest loss also grew within the corporate sector, leading to a lot of companies committing to Zero-Deforestation (ZD) initiatives to eliminate deforestation from their supply chain (Lambin et al., 2018).

For the successful implementation of REDD+ policy processes and ZD commitments, sufficient and reliable information on intact as well as disturbed forest areas is needed. In the last two to three decades a great number of satellite missions have been launched, which

carry different sensors that record either reflected (optical sensors), emitted (thermal sensors) or scattered (active radar sensors) energy. Therefore, they provide data of a wide range of spatial and temporal resolution. Due to the implementation of open data policies along with recent developments of new hardware and software to process a large amount of data, remote sensing can deliver the required information efficiently and cost-effectively (GOFC-GOLD, 2014; Joshi et al., 2016; Turner et al., 2007). Therefore, in order to assess and report progress in the implementation of REDD+ activities, countries are encouraged to build up national forest monitoring systems that integrate remote sensing applications as well as in-situ field measurement approaches to measure forest cover and carbon stock changes (GOFC-GOLD, 2014; IPCC, 2006). The Global Observation of Forest and Land Cover Dynamics (GOFC-GOLD) working group, which was launched in 2005, developed “[...] *a sourcebook of methods and procedures for monitoring and reporting anthropogenic greenhouse gas emissions and removals associated with deforestation, gains and losses of carbon stocks in forests remaining forests, and forestation*” (GOFC-GOLD, 2016) to support countries in the implementation of forest monitoring systems by, among other things, providing information about the contribution and use of remote sensing data, methods and tools. To evaluate the performance of REDD+ activities, reference levels of emissions are needed as these are used for comparison with future emissions and removals. GOFC-GOLD recommends generating a forest benchmark map showing the initial forest cover status. With this map monitoring of deforestation and forest degradation as well as the assessment of forest cover loss can be reduced to the relevant area of interest. For each new analysis date, the forest benchmark map can be updated by subtracting the detected deforested areas from the benchmark map (GOFC-GOLD 2016).

Instead of generating a new forest benchmark map, the forest status can also be derived from one of the various existing, freely available global land cover/land use (LCLU) or forest cover products (Achard et al., 2010). The greatest limitation of most of the global LCLU products is their coarse spatial resolution (ranging from 250m to 1km) as well as different forest definitions (Achard et al., 2010). Regarding global forest maps, currently, there are two products, one based on optical and the other one based on synthetic aperture radar (SAR) imagery, at high spatial resolution available. The optical tree cover product provided by the Global Forest Watch (GFW) project is generated at 30m spatial resolution using all available Landsat 7 Enhanced Thematic Mapper Plus (ETM+) for 2000 and 2010 (Hansen et al., 2013). The SAR-based global forest/non-forest products are based on mosaics of Advanced Land Observing Satellite (ALOS) Phased Array type L-band Synthetic Aperture Radar (PALSAR) sensor imagery and provided at 25m spatial resolution for all years between 2007 and 2010 (Shimada et al., 2014). However, their usability to serve as forest benchmark map for national forest monitoring systems might be limited due to differences in forest definitions (Achard et al., 2010). Within the GFW project, for example, “tree cover” is defined as all vegetation higher than 5m, including natural forests as well as tree plantations (Hansen et al., 2013). For their SAR-based global forest map Shimada et al. (2014) used the forest definition of the FAO, according to which all areas greater than 0.5ha with a crown cover of greater than 10% are forest (FAO, 2000). On that account, generating a forest benchmark map that meets the needs of a national forest monitoring system in term of forest definition might be necessary (Achard et al., 2010).

It needs to be mentioned that the use of remote sensing data has some inherent limitations regarding data availability and accessibility as well as the spatial scale of the required

information (GOFC-GOLD, 2014). The limitations regarding data accessibility have been greatly reduced with the opening of the large data archives, e.g. the Landsat data archive or Sentinel missions of the European Space Agency (ESA), that providing free access to a vast amount of satellite imagery (Wulder et al., 2012) and the launch of new satellite missions with open data policies. The latter does not only provide satellite imagery from different sensor types, but also reduces the issue that high spatial resolution usually comes at the expense of low temporal resolution and vice versa (Lillesand et al., 2015) as two satellites carrying identical sensors operating in the same orbit provide satellite imagery with 10m spatial resolution at a revisit interval up to 5 days (Drusch et al., 2012). An additional strategy to overcome remaining issues of data availability is the integration of remote sensing data from different sensors and the combination of their information in one application (Joshi et al., 2016). To successfully combine data from different sensors, new data pre-processing as well as fusion and analysis methods need to be developed to effectively and efficiently deal with multi-temporal data sets and dense image time series (Joshi et al., 2016). These progresses are expected to enable the improvement of mapping and monitoring of tropical regions where optical data availability has been limited so far due to persistent cloud cover (Asner, 2001).

One recent project which aims to integrate the above-mentioned developments to support REDD+ and ZD initiatives through providing operational services for Earth Observation (EO) based monitoring of the tropical humid and dry forests is the EOMonDis project (Bringing Earth Observation Services for Monitoring Dynamic Forest Disturbances to the Users). The project is focusing on test sites in Peru, Gabon, Malawi and Cameroon. It is, funded by the European Commissions within the frame of the Horizon 2020 programme and provides four different map products to users: land use maps, forest/non-forest maps, forest disturbance maps and forest biomass maps. All maps are produced using time series data of freely available optical (Sentinel-2 and Landsat 8) and SAR (Sentinel-1 and ALOS PALSAR) satellite imagery (www.eomondis.info). This thesis is generated within EOMonDis at JR, who is the partner responsible for the development of a tropical land use mapping and forest monitoring approach using optical time series data.

1.2 Study Objectives

This thesis aims to evaluate if and to what extent the combined use of remote sensing satellite image time series of optical (Sentinel-2 and Landsat 8) and SAR (Sentinel-1) imagery can contribute to the generation of an improved humid tropical forest benchmark map. For this purpose, two different mapping approaches are investigated: (1) a **data-based approach**, where the time series data is combined before the classification and (2) a **result-based approach**, where the combination is done on a semantic level in a post-classification step. The data-based approach is performed with optical and SAR time series data separately as well as with a combined time series. The result-based approach is performed with optical and combined time series data. It is not carried out with SAR time series data because no reasonable forest mapping result can be produced with a mono-temporal SAR scene as backscatter signals from different land use types are very similar. The optical result-based approach involves mono-temporal supervised classification of all images. To reduce the time that is spend on training data selection the applicability of a classification model of one reference scene to classify all other scenes will be investigated. In order to achieve an

accurate result proper data pre-processing is really important. To examine the benefits of the use of time series data, the time series mapping result will be compared to mono-temporal classification results.

Moreover, the impact of the length of the acquisition period used to generate the time series on mapping results will be examined. Regarding input data for classification, Sentinel-2 and Landsat 8 bottom of atmosphere (BOA) reflectance values and the temporal median of each spectral band will be used. Considering an optical image time series where each image possesses 10 spectral bands, the temporal median of, for example, band 1 of a single pixel corresponds to the middle term of the band 1 grey values of all images of this pixel when they are sorted in ascending order. SAR input data sets will be Sentinel-1 backscatter values and a selection of their temporal metrics. This selection includes minimum, maximum, mean and median of backscatter values, standard deviation and coefficient of variation. Furthermore, the performances of Maximum Likelihood (ML) and Random Forest (RF) classifier will be investigated within the optical data-based and result-based approaches by comparing classification results by means of unbiased error matrices. The classifier producing the most promising classification result, measured in terms of overall accuracy, will be employed in the SAR and combined approaches. Finally, in order to test the method's transferability, the forest mapping approach with the highest overall accuracy produced for a study area in Peru will be applied to a second test site in Gabon. Table 1-1 provides a compact overview of the different above-mentioned parameters that are investigated.

Table 1-1: Objects of investigation within the development of the forest mapping approach

Classification component	Objects of investigation
Sensor data	Optical versus SAR Single-sensor versus multi-sensor use
Temporal component	Mono-temporal versus multi-temporal Time series extent
Input data	Optical: BOA reflectance versus temporal median SAR: SAR backscatter versus temporal metrics
Classifier	Maximum Likelihood versus Random Forest
Data combination level	Data-based versus result-based

In the end, answers to the following main research questions are provided:

- Does the use of satellite image time series improve tropical forest mapping compared to mono-temporal classification with the proposed methods?
- Does the integration of optical Sentinel-2, Landsat-8 and SAR Sentinel-1 time series data in a multi-temporal classification approach improve humid tropical forest mapping?
- Is the proposed approach that achieves the more promising results transferable to a different study area located within the humid tropical domain?

2 State of the Art

The two core elements of this thesis are the use of (1) satellite image time series as well as the (2) combination of optical and SAR data for forest mapping applications within the tropical domain. Hence, an overview of the characteristics and limitations of optical and SAR satellite image time series is given in the first subsection 2.1. The following chapter 2.2 deals with the combination of optical and SAR data in general.

The literature review revealed that recent time series based remote sensing applications for the humid tropical forest domain either pursue the objective to generate of more accurate LCLU maps or the development of effective algorithms to detect deforestation and/or forest degradation. As the goal of this thesis is to develop and evaluate methods that integrate time series data from different sensor for the generation of an accurate forest benchmark map, the focus of chapter 2.3 lies on currently most used input variables and algorithms for multi-temporal LCLU classification and will not consider forest change detection methods based on image time series. Similar, the last subsection 2.4 summarizes a selection of recent tropical LCLU and forest mapping applications and projects also not considering aspects of change detection.

2.1 Characteristics and Limitations of Satellite Data Time Series

2.1.1 Optical Time Series Data

Generally, optical data is provided as multi-spectral images consisting of multiple bands sensitive to different regions of the electromagnetic spectrum, ranging from visible to near and short-wave infrared wavelength domain (Lillesand et al., 2015). Hence, optical products capture comprehensive information about reflexion characteristics of the earth's surface which makes them highly suitable and robust for the delineation of LCLU information (Joshi et al., 2016). The first Landsat mission which dates to 1972 marks the beginning of the era of optical satellite remote sensing. Since then, a great number of satellite missions, such as Satellite Pour l'Observation de la Terre (SPOT), Advanced Very High-Resolution Radiometer (AVHRR), Moderate-resolution Imaging Spectroradiometer (MODIS) or Sentinel-2 have been launched, providing an extensive optical satellite image data base of coarse to very high spatial, spectral and temporal resolution (Joshi et al., 2016; Kuenzer et al., 2015). With the opening of large data archives, e.g. the Landsat data archive of the U.S. Geological Survey (USGS) in 2008 (Wulder et al., 2012) and new satellite missions with an open data policy, e.g. ESA's Sentinel Missions (Berger et al., 2012), the basis for optical remote sensing time series analysis which provides high spatial as well as high temporal resolution has been created (Kuenzer et al., 2015). With the two satellites of Sentinel-2 mission (Sentinel-2A and Sentinel-2B) optical data at 10m spatial resolution is provided up to every 5 days for the same region (more information is given in chapter 4.1.2). Although Sentinel-2 Multi Spectral Instrument (MSI) and Landsat 8 Operational Land Imager (OLI) bands are not fully compatible (see Figure 4-2), the fact that data from both sensors are provided for free (Mandanici and Bitelli, 2016) offers a great opportunity of using them in a combined time series. Together they can provide up to 8 images every month and therefore increasing the time series image density enormously. Investigation of radiometric consistency between the two sensors revealed a

high correlation between corresponding bands under clear conditions (Mandanici and Bitelli, 2016) leading to the assumption that a combined use is feasible. The increasing availability of dense optical image time series has not only provoked the development of new LCLU mapping approaches but made it necessary to development of novel methods to detect dynamic and gradual as well as long-term change processes which has significantly improved monitoring systems (Joshi et al., 2016).

However, the greatest limitation which constrains the availability of optical data is persistent cloud cover, especially in humid tropical or northern regions, where mean annual cloud cover may exceed 80% (Asner, 2001; Hansen et al., 2008a; Herold, 2009). To fill the data gaps caused by clouds and to solve the problem of reduced image density various algorithms to combine optical data from multiple-dates and/or multiple sensors have been developed (Joshi et al., 2016). Currently, two different approaches to produce gap free information based on image time series are used: (1) image compositing and (2) temporal interpolation. The first approach involves splitting of the entire time series into so-called compositing periods. All images within a compositing period are subsequently used to generate one cloud-free image using certain compositing criteria (White et al., 2014). The extent of a compositing period depends on the aim of the study as well as on the temporal resolution of the used sensor. However, it needs to be mentioned that using a certain time interval to generate an image composite, the resulting image serves as representative for the whole compositing period (White et al., 2014). Moreover, it is possible that in image composites of regions with frequent cloud cover data gaps remain (Roy et al., 2010). To overcome this issue and increase the image density, the temporal interpolation approach generates continuous gap-free optical image time series. In order to estimate the grey value of a pixel at any given time, available non-cloud and non-cloud shadow observations are used to generate a mathematical model that best fits the temporal trend of the observed pixel values (Gao et al., 2008). Several of these algorithms combine data from high-revisit moderate spatial and medium-revisit high spatial resolution sensors, for example MODIS and Landsat data (Gao et al., 2006; Sedano et al., 2014; Zhu et al., 2010).

In addition to the presence of clouds, information extraction from optical images is also limited by similarities in spectral characteristics of different land cover and land use types at a certain point in time. For example, different crop types or tree plantations may appear similar to natural forests at a specific point of time. However, as different types of vegetation show a different behaviour in their temporal vegetation cycle, time series data can enable their discrimination (Joshi et al., 2016).

2.1.2 SAR Time Series Data

The first radar-based EO satellites that provide a sufficient basis for time series analysis are the two European Environmental Satellites ERS-1 and ERS-2 which were launched in 1990 (operated until 2000) and 1995 (still operating) respectively. More satellite missions have followed since the beginning of the new millennium, for example ENVISAT Advanced Synthetic Aperture Radar (ASAR), ALOS PALSAR and ALOS PALSAR 2, Radarsat, COSMO-SkyMed, TerraSAR-X or Sentinel-1 (Kuenzer et al., 2015).

In contrast to optical systems that measure reflectance, radar systems record the intensity of the backscattered signal. Hence, they contain information about geometric and dielectric

characteristics of the reflecting object. SAR sensors operate at one wavelength range in the microwave domain of the electromagnetic spectrum (see Table 2-1) and two polarizations. Polarization refers to the ability of electromagnetic waves to oscillate in different geometric planes. Regarding radar systems, signals typically are transmitted and received either parallel (horizontal, H) or perpendicular (vertical, V) to the antenna axis. This leads to four possible polarization combinations, which are referred to as co-polarizations, if transmitted and received signals have the same polarization (e.g. HH and VV) and cross-polarizations, if the polarization of transmitted and received signal is different (e.g. HV and VH). Nevertheless, it provides a limited spectral feature space compared to most optical sensors (Joshi et al., 2016; Lillesand et al., 2015).

The biggest advantage compared to optical systems is that the radar signal is not sensitive to atmospheric conditions, e.g. cloud cover and haze, and, as it is an active system, it operates independently at any time of the day (Lillesand et al., 2015). Furthermore, considering forest cover, while optical sensors only record signals from the treetops, the SAR signal can penetrate the canopy. The depth depends on the wavelength the system is operating at. L-band signals penetrate deeper than C-band signals (Reiche, 2015). The impact of different wavelengths on land cover mapping in tropical regions has recently been under great investigation. For example, Hagensieker and Waske (2018) evaluated the impact of multi-temporal L-band (ALOS PALSAR 2), C-band (RADARSAT-2) and X-band (TerraSAR--X) images on tropical land cover classification results in the Brazil Amazon. Results show that, when comparing mono-temporal classification L-band SAR data is most suitable for land cover classification (Hagensieker and Waske, 2018). This very well corresponds to the results of previously conducted studies which focused on the comparison of L-band ALOS PALSAR and C-band RADARSAT-2 for land cover classification in tropical regions (Li et al., 2012).

Table 2-1: Radar band characteristics (Lillesand et al., 2015)

BAND	WAVELENGTH [CM]	BAND	WAVELENGTH [CM]
K _A	0.75-1.1	C	3.75-7.5
K	1.1-1.67	S	7.5-15
K _U	1.67-2.4	L	15-30
X	5.4-3.75	P	30-100

Two important limitations affect the use of SAR time series data. First, the signal is disturbed by speckle noise which leads to an irregular pattern of brighter and darker pixels in the image. This effect is caused by slight differences in the measured distances of the signals backscattered by objects that are located within a single image pixel. Considering their representation, radar signals form sinusoidal waves with a cyclic pattern of peaks and troughs. The position of a signal along this cycle is called *phase*. Depending on the phases of the received signals, the intensity of the combined signal is either amplified or reduced. Thus, homogeneous surfaces very often show an inhomogeneous pattern in the image. This speckle effect can be reduced by the application of certain spatial or temporal filters. However, it cannot be completely eliminated (Lillesand et al., 2015).

The second limitation is caused by radar inherent geometric characteristics (Joshi et al., 2016). Most radar systems are side-looking systems, which means that the signal is not transmitted

orthogonal to the earth's surface, but with a certain angle (look angle). Considering a very steep terrain slope within a mountainous area, the transmitted signal first reaches the top of the mountain. Hence, the sensor first receives the backscattered signal from the top, consequently leading to a "lay over" of the signal from the mountain base in the image. However, if the terrain is less steep and the transmitted signal reaches the base first, the slope will not necessarily be represented in their true size but shortened. This effect is called foreshortening. A third phenomenon that appears in radar images of mountainous regions is the shadow effect, which is caused by the fact that the transmitted signal cannot reach steep slopes facing away from the antenna. Therefore, no information can be obtained from those areas and they appear dark in the image (Lillesand et al., 2015).

2.2 Optical and SAR Data Combination Approaches

Considering the characteristics and limitations of optical and SAR sensor types described in the previous chapters, the conclusion can be drawn that they provide complementary information, each with its own important limitations, but except shadow effects caused by topography, these limitations do not overlap. Therefore, they even may compensated one another (Joshi et al., 2016).

One crucial issue regarding the use of multi-sensor data fusion within multi-temporal mapping approaches is proper data pre-processing to ensure data consistency. Sensor specific as well as general pre-processing steps must be performed to enable an appropriate combined use. Optical specific data pre-processing may include geometric and radiometric correction. Geometric adjustment to correct geometric distortions is essential when images from different sensors are combined in one time series to ensure that the overlapping pixels of different images represent the same area on the ground. Radiometric correction regarding optical data can be divided into absolute and relative correction. Absolute radiometric adjustment is performed to eliminate atmospheric influence on the received signal and transform pixel values from Digital Numbers (DN) to surface reflectance values. The idea of relative radiometric adjustment is to choose one reference scene and adjust the pixel values of all other scene to that scene. Radiometric adjustment is a really important step when a time series of optical images is involved to ensure temporal radiometric consistency. If the study area is located within a mountainous region, also topographic normalization should be performed. Regarding tropical regions with frequent presence of clouds, a cloud masking pre-processing step is usually applied. SAR specific pre-processing includes speckle noise reduction, either using spatial and/or temporal filtering algorithms, as well as the reduction of geometric and radiometric effects due to topography. For a combined use, geocoding to a common reference system and resampling to a common pixel size is essential. If these pre-processing steps are performed insufficiently or inaccurately, poor quality of analysis results is to be expected (Banskota et al., 2014; Hirschmugl et al., 2017b; Joshi et al., 2016; Kuenzer et al., 2015; Pohl et al., 2015).

Combining optical and SAR data within remote sensing applications has been performed since many years (Joshi et al., 2016; Zhang, 2010). However, as observed grey values of optical and SAR images do not correlate, combination methods on a data-level that preserve spectral as well as spatial characteristics of both sensors are difficult to design. Furthermore, these methods should provide a simultaneous reduction of the effects of their limitations and they should minimize computational costs (Alparone et al., 2015; Zhang et al., 2010). The

combination of SAR and optical data on a result-level avoids this problem by classifying each source individually. Results are then combined using various methods of for instance probabilistic theory, evidence theory, fuzzy, theory, neural networks, or ensemble learning classifiers. This way, characteristics of both sensors can successfully be preserved (Zhang, 2010). Various studies confirm the possibility to increase classification accuracies by a combination of optical and SAR data on result level (Waske and van der Linden, 2008; Zhang et al., 2015). However, it needs to be mentioned that the success of result-based combination methods depends on its effectiveness (Fernandez-Beltran et al., 2018). Generally, it can be stated that within most studies, the objective of the combination of optical and SAR data is to enhance the features that are relevant for a specific application. This leads to the development of application-specific methods, rather than general combination methods (Alparone et al. 2015).

2.3 Multi-temporal Image Classification

In a multi-temporal classification approach, the data time series can be integrated at two different phases: (1) prior to the classification and (2) in a post-classification analysis. The latter includes mono-temporal classification of each image and the subsequent combination of the time series of single-date maps via a certain ruleset. Integrating the time series before the classification may involve the extraction of spatio-temporal features as input for the classification. The input features are combined in one image stack that serves as input data for classification. In chapter 2.3.1 input feature extraction in the context of time series data is discussed in more detail. An overview of classification algorithm with the focus on the ones used in this thesis is provided in chapter 2.3.2.

2.3.1 Input Features

Regardless of method, sensor and input data, at least one feature serves as input for classification. Typically, these features are image bands, such as top-of-atmosphere reflectance (TOA), BOA reflectance or, in case of SAR data, backscatter or intensity values. Also, dimensionless index variables derived from the above-mentioned bands, for example band ratios, the NDVI, the enhanced vegetation index (EVI), the soil water index (SWI), the normalized difference snow index (NDSI), Tasseld Cap components (Brightness, Greenness and Wetness), etc. are used very frequently. If digital elevation models (DEM) are available, measurements like height, slope, aspect or surface roughness can be integrated. Furthermore, texture variables including object size, object shape, compactness, homogeneity and heterogeneity, neighbourhood relationships and connectivity can serve as input variables to classification (Kuenzer et al., 2015).

An image time series provides a multi-temporal feature space that captures comprehensive information about the temporal behaviour of different thematic classes (Gómez et al., 2016). Currently, the most common applied method for the purpose of LCLU classification is to summarize this multi-dimensional feature space by calculating various statistical metrics, such as minimum, maximum, mean, median, standard deviation, trend etc. (Zhai et al., 2018). Like image compositing for the generation of gap free images, either the entire available time series or only images of a specific period can be used to calculate these metrics. The derived temporal features then serve as input data for supervised or

unsupervised classification. Using only a certain period may reveal some information which an annual time series for example might suppress. For instance, using images of the growing season allows capturing the certain temporal behaviour of a specific crop type. Nevertheless, considering humid tropical regions, using temporal metrics instead of spectral bands of each image of a time series minimizes the problem of data gaps due to clouds. Various studies have already proven the suitability of temporal metrics of optical data as well as SAR data for LCLU classification and forest change detection (Broich et al., 2011; Clark et al., 2010; Deutscher et al., 2017; Franklin et al., 2015; Gebhardt et al., 2014; Hirschmugl et al., 2017a; Hirschmugl et al., 2018; Jia et al., 2014; Waldner et al., 2015).

Instead of calculating temporal metrics, the multi-dimensional feature space can be projected into lower dimensional data with the purpose of capturing maximum information content while minimizing noise (Scott, 2015). Dimensionality reduction (DR) methods are for example Principal Component Analysis (PCA), Linear Discriminant Analysis (LDA), projection pursuit (PP), minimum noise fraction (MNF), independent component analysis (ICA), spatial-spectral eigenvector derivation (SSEVD) and Laplacian Eigenmaps (LE). Recently, efforts have been made to develop DR methods that can handle missing data in image time series. For example, Yan and Roy (2015) proposed a DR method based on LE that can handle large areas of missing data within multi-temporal Landsat data and used the derived features for LCLU classification with RF classifier. For comparison, they also calculated various temporal metrics for the same time series and used them as classification input variables. Results show that their DR technique performs better than integrating temporal metrics (Yan and Roy, 2015).

2.3.2 Classification Algorithms

Up to now, most remote sensing LCLU applications using time series data are employing the same classification algorithm that are used within mono-temporal approaches (Gómez et al., 2016; Zhai et al., 2018). The selection of the classifier depends on multiple parameters, for example data type, statistical distribution of classes, target accuracy, ease of use, speed, scalability and interpretability of the classifier (Gómez et al., 2016). Within this thesis, the Maximum Likelihood (ML) and Random Forest (RF) classifiers are utilized. Therefore, only these two classifiers will be described in detail.

Table 2-2 provides an overview of the most important automatic image classification algorithms that are used in the context of multi-temporal image classification, as identified in the literature. Basically, there are two large groups of classification algorithms, unsupervised and supervised classifiers. Unsupervised refers to the fact that no a priori human knowledge is integrated in the classification. Pixels that share the same spectral characteristics are grouped to a pre-defined number of clusters. As automatically generated clusters are not labelled and do not necessarily correspond to (desired) thematic classes, accurate classification post processing is important (Lillesand et al., 2015).

Table 2-2: Most common multi-temporal classification algorithms

UNSUPERVISED	SUPERVISED		
	Parametric	Non-parametric	Non-Metric
k-means			
Iterative Self-Organizing Data Analysis (ISODATA)	Maximum Likelihood	Artificial Neural Networks	Decision trees
Self-Organizing Maps		Support Vector Machines k-Nearest Neighbour	Random Forest

In contrast to unsupervised algorithms, supervised classification methods integrate a priori knowledge of the study region. For each thematic class training samples that represent ground truth need to be derived, either from field work, visual interpretation of aerial or very high resolution (VHR) satellite images or already existing thematic maps. In theory, spectral characteristics of target classes should not overlap, and a training sample should represent a thematic class unambiguously. In practise, it is hardly possible to achieve this, on the one hand, due to internal spectral variance of thematic classes and on the other hand due to effects of haze, topography, system noise and mixed pixels (Campbell, 1996). This might have a critical negative effect on classification results, especially when the statistics of the training samples are used to parameterize the classifier because parametric classifiers, such as Maximum Likelihood, Minimum Distance or Mahalanobis Distance, require multivariate normal frequency distribution. To effectively assign pixels that fall into these overlapping regions, the **Maximum Likelihood (ML)** classifier, which is used in this thesis, uses spectral mean and variance values of each class to calculate class membership probabilities to assure classification result for each pixel (Lillesand et al., 2015).

Given the fact that time-series data is involved in the classification process, data dimensionality increases considerably. Due to correlation between spectral features, a multi-dimensional data set most likely contains redundant information (Glanz et al., 2014; Joshi et al., 2016). To reduce the amount of data without losing any information, either dimensionality reduction and/or calculation of temporal metrics can be performed (as described in the previous chapter 2.3.1) or alternative classification methods that do not rely on training sample statistics can be used. Although some of these so-called non-metric classifiers are computationally intense, they are attractive alternatives because of their ability to handle high dimensional data (Gómez et al., 2016). That is why the group of ensemble classifiers and among them, the **Random Forest (RF)** classifier, due to high accuracies and speed of processing, have recently gained popularity within remote sensing image classification (Belgiu and Drăguț, 2016; Rodriguez-Galiano et al., 2012). In contrast to parametric classifiers such as ML, the RF classifier does not need to use training data statistics to parameterize the classification model. Instead it integrates a set of independent decision trees to model the relationship between predictor (e.g. surface reflectance, NDVI, temporal metrics, etc.) and response variables (e.g. LCLU classes). Each decision tree consists of a set of binary rules based on predictor variables, nodes and branches which connect the nodes. At each node one binary decision rule is evaluated, leading either to a branch that ends in a terminal node or in another binary decision rule. When all branches end in a terminal node, the tree stops to grow. To classify a single pixel, it is modeled down each decision tree generating a response value. The final classification result corresponds to the majority value of all response values. To train the classifier, only a subset of all training

samples is used. The ones omitted are used to estimate the error rate by calculating the out-of-bag (OOB) error (Breiman, 2001; Horning, 2010; Liaw and Wiener, 2002).

The strength of the RF classifier lies in the fact that it does not use all training samples to build a decision tree and does not use all predictor variables to define the split criterion in each node. Rather, a defined subset of training samples and predictor variables is selected randomly with replacement. Consequently, the correlation between decision trees is low. However, if the number of predictor variables is too low, the predictive power of the model decreases. Thus, quality of classification results depends strongly on a well-chosen number of predictor variables that minimize tree correlation and guarantee high predictive power that decreases forest error rates (Breiman, 2001; Horning, 2010; Liaw and Wiener, 2002; Oshiro et al., 2012).

Regarding the sensitivity of the RF classifier to training data sampling design and imbalanced training samples it needs to be mentioned that different studies reveal contradictory results. According to Dalponte et al. (2013) an unbalanced number of training samples negatively affects classification accuracies as the model tends to favor the most representative one. Contrary, Mellor et al. (2015) found out that mislabeled and imbalanced training samples do not have an impact on RF classification. In his extensive study Colditz (2015) investigated the sensitivity of RF to different settings of sampling design, such as random sampling, area-proportional allocation and the allocation of an equal number of samples per class. The results show a strong impact of the expected area of the classes on training sample allocation as area-proportional allocation received the best classification accuracies (Colditz, 2015). Furthermore, also the size of training data affects the classification. Within the before mentioned study, Colditz (2015) identifies a training sample size of approximately 0.25 % of the study area to be suitable.

Different parameters need to be set when applying a RF classification. First, the number of decision trees to generate the forest must be defined. Generally, no limit for the number of trees exists. However, the higher this value is set, the more computationally intensive the classification becomes (Belgiu and Drăguț, 2016). The second parameter is the number predictor variables to define the split rule in each node. By default, this value is set to the square root of the number of input variables. Similar to the number of trees, increasing the number of variables increases the computational time (Belgiu and Drăguț, 2016). Moreover, the user can define the minimum number of samples in each node and the maximum tree depth. Both parameters function as termination criteria. If the number of samples in a node is smaller than the defined minimum, the node will not be split. Concerning the maximum tree depth, as long as the tree depth is smaller than the defined value, the algorithm will attempt to split each node (ORFEO Toolbox, 2018).

In general, ML and RF classifiers as well as the other methods mentioned in Table 2-2 have proven to perform very well when using DR or statistical metrics of temporal trajectories as input features. However, to fully exploit the entire information temporal trajectories are providing, new methods to map LCLU classes need to be developed (Gómez et al., 2016). First attempts have already been made to integrate spectral, temporal and spatial features in the classification process, but their performance on different datasets as well as applicability in different geographic locations regions is yet to be tested and evaluated (Gómez et al., 2016; Liu and Cai, 2012; Schäfer et al., 2018; Zhai et al., 2018).

2.4 Tropical LCLU and Forest Mapping Applications

The free access of large data archives triggered the extensive use of image time series for remote sensing applications within tropical forest regions. However most of them focusing on the detection of forest changes to estimate forest cover loss and/or regrowth rather than LCLU applications. A lot of studies utilizing optical time series data to assess forest cover changes, use MODIS and Landsat imagery due to a large amount of available data. Various studies have proven their usability for reconstructing tropical forest change history (DeVries et al., 2015; Hansen et al., 2008b; Hirschmugl et al., 2014; Langner et al., 2018; Lu et al., 2017; Müller et al., 2016; Schneibel et al., 2017; Shimizu et al., 2017; Souza et al., 2013) as well as to develop near real-time monitoring systems (Hansen et al., 2016; Shimabukuro, 2006). As clouds are reducing the amount of available optical images, some studies focused on detecting forest disturbances using only SAR time series data (Almeida-Filho et al., 2007; Antropov et al., 2015; Delgado-Aguilar et al., 2017; Deutscher et al., 2017; Joshi et al., 2015; Mermoz and Le Toan, 2016; Motohka et al., 2014). Within a couple of studies the potential of the combination of optical and SAR sensors for tropical forest monitoring was investigated (Hirschmugl et al., 2017a; Reiche et al., 2018, 2015b, 2015a; Verhegghen et al., 2016)

The possible benefits of fusion of optical and SAR imagery for tropical LCLU applications was investigated in various studies in the last two decades. However, a lot of them rely on a single-date or bi-temporal data basis (Carreiras et al., 2017; Clerici et al., 2017; Erinjery et al., 2018; Hame et al., 2013; Hoan et al., 2013; Kuplich, 2006; Sothe et al., 2017; Sukawattanavijit et al., 2017; Vaglio Laurin et al., 2013; Walker et al., 2010). For example, Vaglio Laurin et al. (2013) used multi-spectral Landsat 5 Thematic Mapper (TM) data and Advanced Visible and Near Infrared Radiometer 2 (AVNIR-2) in combination with L-band ALOS PALSAR (HH and HV polarization) data for forest and land cover mapping in tropical West Africa. Atmospheric correction and haze removal were applied on optical imagery prior to classification. Additionally, orthorectification of the AVNIR-2 image was performed using the DEM from the ASTER derived Global Digital Elevation Map mission and cloud pixels were masked out. PALSAR data pre-processing included the application of multi-looking, terrain-correction and geo-coding to a spatial resolution of 15m. AVNIR-2 as well as PALSAR data were co-registered to the Landsat TM image. A set of texture variables including mean, entropy, correlation, variance, and second moment, based on Grey-level Co-occurrence Matrix (GLCM) was calculated. Regarding optical data sets, only bands 4 (red), 5 (NIR) and 7 (SWIR) for Landsat and bands 3 (red) and 4 (NIR) of AVNIR-2 were used to calculate the texture variables as they are sensitive to vegetation. Prior to classification, the amount of texture features was reduced using the training data set within a wrapper approach to select those features that contribute most to classification accuracies. Two classifiers, the parametric ML and non-parametric Neural Networks (NN) classifier, were used to perform the land cover classifications using the following different classification input settings. Classification was conducted using only optical and only SAR features as well as a combination of both. However, TM and AVNIR-2 were not combined. The best overall accuracy was obtained with the NN classifier using the combination of AVNIR-2 reflectance plus texture variables and PALSAR backscatter plus PALSAR texture (97.5%) and increased the classification accuracy compared to the best optical only result by about 3.10%. Furthermore, the authors concluded that using only mono-temporal PALSAR data for land cover classification is not sufficient to distinguish between selected land cover classes (75.70% best OA), thus SAR data cannot fully replace optical data within a mono-temporal

approach. But it provides valuable input, especially to fill data gaps in optical imagery due to persistent cloud cover (Vaglio Laurin et al., 2013).

More recently, Clerici et al. (2017) investigated the combined usability of multi-spectral Sentinel-2 and SAR Sentinel-1 data (VV and VH polarization) to improve basic LCLU classification in Colombia, incorporating the classes *forest, water, crops, pastureland, build* and *secondary vegetation/shrubs*. SAR data was pre-processed using the Sentinel-1 toolbox provided by ESA and included thermal noise removal, TOPSAR deburst, image mosaicking, resampling to 10m spatial resolution, application of multi-looking and Speckle noise reduction using a Refined Lee low-pass filter (5 x 5 kernel). Pre-processing of S2 data included the calculation of surface reflectance values using Sen2Cor processor provided by ESA and resampling of 20m spatial resolution image bands to 10m resolution using bi-linear interpolation. Both sources were terrain corrected using a 30m SRTM digital elevation model. Variance and contrast texture features of both SAR polarizations were calculated using GLCM algorithm. Furthermore, four vegetation indices (NDVI, S2REP red-edge index, MSAVI and GNDVI) were derived using the S2 image. Together with S1 amplitude images and S2 surface reflectance images (excluding 60m spatial resolution bands), the SAR textures and optical indices served as input variables for RF, SVM and kNN classifications. Classification was performed using three different sets of input variables: optical features only, SAR features only and a combination of both. Results indicated that the use of single-sensor features does not lead to acceptable results. The best single-sensor classification was produced using optical features and SVM (72.5%). Regardless of used classification method highest accuracies were always achieved when all features are used for classification. The best result was obtained when with SVM classification algorithm with all SAR and optical input features (88.75%) (Clerici et al., 2017).

As the sensors have been operating for three to four years, several studies have been published recently that investigate the usability of either S1 or S2 time series data. Mapping approaches focus on agriculture (Clauss et al., 2018; Kontgis et al., 2017; Lambert et al., 2018; Rozenstein et al., 2018; Torbick et al., 2017), flood monitoring (Martinis et al., 2018), monitoring of waterbodies (López-Caloca et al., 2018; Ottinger et al., 2017) or vegetation (Jönsson et al., 2018; Niculescu et al., 2018). However, up to date, only a limited number of studies have been conducted to investigate the added value of a combined use of S2 and/or L8 and S1 time series data for LCLU classification in tropical regions. One example is the study published by Hagensieker and Waske (2017), who used Landsat OLI and S1 time series data within a land cover classification approach of the Brazilian State of Mato Grosso. All L8 surface reflectance products and S1 images acquired in 2016 were considered. Pre-processing of S1 data included calculation of γ^0 , multi-looking and image co-registration. To eliminate the impact of clouds on temporal metrics values of optical L8 data, the cloud masks delivered with the L8 surface reflectance product were used to eliminate cloudy pixels. Annual as well as seasonal statistics (minimum, maximum, mean, standard deviation, range and median) were calculated and served as input for RF classification. The use of all available temporal features of L8 as well as the combination of all temporal features of L8 and S1 produced the same classification result (about 95%). Results achieved with SAR data only were 88%. This led to the conclusion that optical time series data might be sufficient for LCLU classification in the humid tropics. However, the authors emphasized that SAR data is of great assistance if the optical data availability is limited due to clouds (Hagensieker and Waske, 2017).

The combined use of optical S2 and SAR S1 time series data to improve forest and LU mapping in a dry tropical region in Malawi was exploited by Hirschmugl et al. (2018). Within this study the differences in using mono-temporal and multi-temporal data as well as the impact of acquisition date (dry season versus rainy season) were investigated extensively. Pre-processing of S2 data included atmospheric correction, cloud masking and topographic normalization. Only BOA reflectance images were used as input variables for RF classification, no additional features were calculated. Pre-processing steps of S1 data included radiometric calibration to gamma naught, multi-looking, speckle noise reduction through the application of a modified Frost filter and a multi-temporal filter, image stacking and orthorectification. Temporal metrics of the multi-temporal backscatter image stack (mean, minimum and maximum backscatter, standard deviation, coefficient of variation and trend between first and last three images) were calculated for the S1 image stack. Classification was based on two different approaches, a data-based and a result-based approach. The data-based approach utilized different image stacks as input variables for RF classification, whereas the result-based approach combines two separately generated probability maps within a Bayesian combination framework. As both approaches are similar to the ones used within this thesis, the reader is referred to chapter 5.3 for detailed information on pre-processing as well as the applied methodology. The added value of time series data in comparison to mono-temporal classification approaches was only evaluated using optical S2 data. Results for forest mapping showed a significant increase of OA when multi-temporal data was used within the data-based approach. However, using only SAR time series features achieved a worse result regarding forest/non-forest classification compared to optical mono-temporal classification. Furthermore, OA increased when images from dry and rainy season were combined compared to mono-temporal as well as multi-temporal classification utilizing observations from the dry season only. The combination of optical-mono-temporal and SAR time series data achieved similar mapping accuracies to optical multi-temporal results (83.64% versus 83.10%). Due to this the authors concluded that a time series of SAR data can replace optical time series data to map dry tropical forest if only a limited number of clear optical observations are available. The combined use of S2 and S1 time series within the data-based approach slightly increased the OA to 85.26%. This is also the best result achieved within the study, as compared to the proposed result-based approach the OA is about 2% higher. Additionally, a comparison of the results of forest mapping with freely available maps (Global Forest Watch and CCI Land Cover) revealed that an increase of OA of more than 10% can be obtain with the application of the proposed approaches and data (Hirschmugl et al., 2018).

3 Study Areas

Two of the EOMondis project study regions will be considered in this thesis. The Peruvian study area is used to investigate the performance of all developed approaches and their different settings. The approach that produces the best mapping result is then be applied to the Gabonese study area. The forest definition for the two study areas that are used within the project are given in Table 3-1.

Table 3-1: Forest definitions used in the EOMonDis project

	GABON	PERU
Minimum area	1ha	0.5ha
Potential height at maturity	5m	5m
Minimum tree crown cover	30%	10%

3.1 Peru

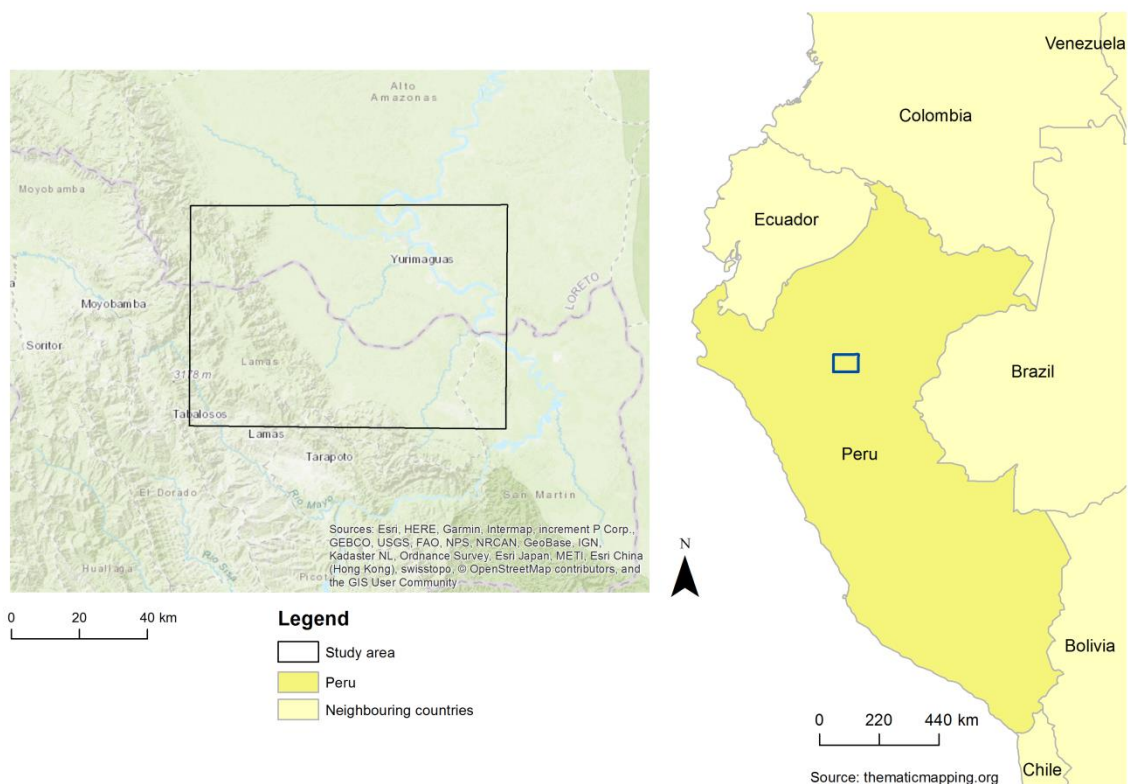


Figure 3-1: Peruvian area for forest mapping

The Peruvian study (see Figure 3-1) site extends an area of approximately 6000km² around the city of Yurimaguas (76°05'W, 5°45'S) which is located at the river Huallaga near the

border between Loreto and San Martín regions. Referring to the global ecological zones defined by FAO (2001) for the Global Forest Resources Assessment Report, most of the study area lies within the tropical rainforest zone which is characterized by a mean temperature of all months over 18°C, an annual precipitation of at least 1500mm and at most three dry months during winter. In Yurimaguas the mean long-term temperature is 26°C and the mean annual rainfall is 2200mm (Nicholaides, et al., 1985; Palm et al., 2002). Only in June, July, August and September the mean monthly rainfall is lower than 200mm (Nicholaides, et al., 1985). According to the FAO definition tropical evergreen forests are characterized by vegetation that *“[...] is lush, with tall, closely set trees that often form a continuous multi-layered canopy and emergent trees reaching a height of 50 to 60 meters. Most diverse terrestrial ecosystem, with a large number of tree species”* (Simons, 2001). The mountainous region in the western and south-western parts of the study area, which belongs to the Peruvian Central Andes, is in the ecological zone of tropical mountain systems. In contrast to tropical evergreen forests this ecological zone is affected by great climatic variability depending on altitude. Thus, this zone is native to *“[...] a high variety of vegetation types along altitudinal belts, ranging from evergreen submontane rainforest, cloud forest up to alpine grassland”* (Simons, 2001).

The area around Yurimaguas has a long agricultural history of shifting cultivation and is used as test site for multiple research projects on developing continuous crop management systems for the Amazon Basin. Although a lot of research projects on how to implement continuous cropping systems and agroforestry systems, have been conducted since the 1970s, rainforest is still cleared by farmers using traditional shifting cultivation methods (Nicholaides, et al., 1985; Sanchez and Nureña S., 1972). However, it is still an ongoing discussion if these rotational farming methods either negatively affect tropical rainforests and its ecosystem or if they support sustainability and biodiversity as well as providing food and livelihood security for small-scale farmers and the local community (Padoch and Pinedo-Vasquez, 2010).

According to U.S. Agency for International Development (2015), another big issue regarding deforestation and forest degradation in the Amazon rainforest is large-scale crop plantation, especially palm oil plantation, and plantation management. Palm oil is one of the most promising crops that may have a positive effect on economic growth. However, since this sector lacks governmental regulation, not only large natural forest ecosystems are released for cultivation of oil palm, but also participation of large-scale producers and small-scale producers is unbalanced, leading to an unequal distribution of benefits among large companies and local stakeholders. Land area used to cultivate palm oil plantations significantly increased from 14.600 ha in 2000 to more than 58.000 ha in 2013 in the whole Peruvian state. Since 2006, the year of its initiation, a palm oil plantation has been growing completely at the expense of natural forest to the south of Yurimaguas. By 2013 the production area of this plantation was 15.910 ha. To ban deforestation due to insufficient palm oil plantation management and to promote a sustainable expansion of the palm oil sector, ecological optimization of palm oil production on existing plantations would be one step into the right direction. Furthermore, cultivating new palm oil plantations should be limited to already deforested or degraded areas to ensure conservation of biodiversity and of permanent forest reserves U.S. Agency for International Development (2015).

3.2 Gabon

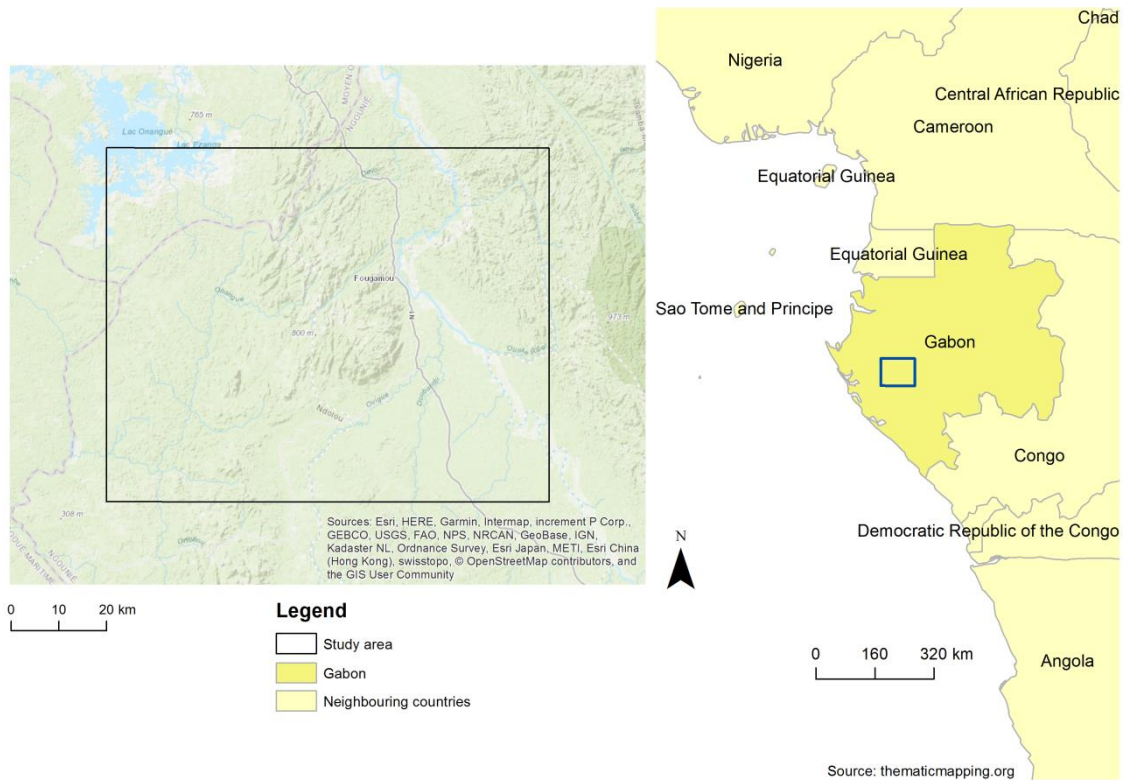


Figure 3-2: Gabonese study area for forest mapping

The Gabonese study area (see Figure 3-2) is approximately 6830 km² large and extends over parts of the provinces of Ngouine, Ogooue-Maritime and Moyen-Ogooue. It completely lies within the ecological zone of tropical rainforests. In Fougamou (10°35'E, 1°13'S), the largest city in the study area, the climatic conditions are very similar to Yurimaguas with a mean long-term temperature of 26°C and a mean annual precipitation of 1995mm with the dry season between June and September where precipitation does not exceed 100mm (<https://de.climate-data.org/location/32332/#climate-graph>).

Prior to the turn of the millennium, economic pressure on forest in Gabon was low due to great substantial deposits of non-renewable resources like petroleum, manganese and uranium. However, with the depletion of these deposits Gabon's economy became heavily reliant on timber export, leading to an increase in forest logging activities. This does not only affect tree species composition, densities and size-class frequency distribution, but also facilitated illegal hunting activities due to easier accessibility of forests as most logging roads are not controlled properly. Besides logging, also the growing worldwide demand of palm oil drives deforestation in Gabon. In the southern part of the study area a palm oil plantation has been growing since 2014 and covers an area of 11.500 ha (Collomb et al., 2000; Laurance et al., 2006; Medjibe et al., 2011).

4 Data Source

4.1 Sentinel Data

Within the frame of the Copernicus Programme, ESA is developing the space component, a series of long-term operational satellite missions, called Sentinels, to provide reliable EO data for environmental and security monitoring services (Aschbacher and Milagro-Pérez, 2012; Berger et al., 2012). Each mission consists of two identical satellites to provide data continuity with a high revisit frequency. Regarding to data policy, users can access Sentinel data from all missions for free. With the aim of consistent distribution, all Sentinel data is available in the Sentinel Standard Archive Format for Europe (SAFE) (Aschbacher and Milagro-Pérez, 2012; Suhet, 2013). Within this master thesis, data from the Sentinel-1 (SAR) and Sentinel-2 (optical) missions are used.

4.1.1 Sentinel-1

The Sentinel-1 mission has been developed to systematically acquire radar-images of oceans, terrestrial surfaces, coastal areas, sea-ice and polar areas to provide long-term data continuity and improvement for all operational SAR related services and applications. More specifically, it should support and enhance polar sea-ice mapping and monitoring, marine surveillance and security services and terrestrial motion risk area monitoring services (due to earthquakes, landslides, etc.) to ensure fast reaction and improve disaster management to prevent extensive crisis situations. Both Sentinel-1 satellites were launched successfully, the first one, Sentinel-1A, on 3 April 2014 and the second one, Sentinel-1B, on 25 April 2016. Table 4-1 shows the most important key features of the mission. The day-and night, all-weather radar system of the Sentinel-1 mission with its high temporal resolution of six days is designed to be able to combine its data with ERS1/2 and Envisat SAR data in one image time series (Aschbacher and Milagro-Pérez, 2012; Suhet, 2013; Torres et al., 2012).

Table 4-1: Key characteristics of the Sentinel-1 mission (Torres et al., 2012)

Mission characteristics	Data
Mission lifetime	15 to 20 years
Number of satellites	2
Nominal in-orbit satellite lifetime	7 years with consumables for additional 5 years
Orbit	Near-polar sun-synchronous at 693km (mean altitude), 175 orbits per cycle 18:00 LTDN
Nominal flight attitude	Right looking
Land Coverage	45°S to 45°N
Global revisit time	12 days at the equator (one satellite) 6 days at the equator (two satellites)

To meet all requirements the Sentinel-1 satellites are equipped with a C-band SAR sensor that supports four different acquisition modes. The Interferometric Wide-Swath Mode (IW), operating in ScanSAR mode, features a swath width of 250km with a ground range resolution of 5m and an azimuth resolution of 20m. The Wave Mode (WM) provides observations of 20km x 20km with a ground resolution of 5m x 5m using single strip map mode. Data acquired through Strip Map Mode (SM) provide 5m x 5m ground resolution covering an area of 80km. The Extra Wide-swath Mode (EW), implemented as ScanSAR mode, features data of 20m x 40m medium ground resolution, while extending the swath width to 410km. Except WM, which is operating with single polarisation (HH, VV), all modes support dual polarisation (HH+HV, VV+HH) (Torres et al., 2012).

Sentinel-1 data is available in three different processing stages. Level-0 data products include compressed unfocused SAR raw data. Level-1 data are either Single Look Complex (SLC) or Ground Range Detected (GRD) products. The SLC product features geo-referenced focused SAR data in zero-Doppler slant-range geometry and provides the phase information needed for SAR Interferometry. The GRD product provides projected to ground range, multi-looked, focused SAR data with square pixels in different resolutions according to the acquisition mode. Level-2 Ocean products (OCN) contain Ocean Swell Spectra (OSW), Ocean Wind Fields (OWF) and Surface Radial Velocities (RVL) (Suhet, 2013).

For both test sites of this study VV and VH polarized S1 Level-1 GRD products acquired in IW mode are used. 30 images between 3 March 2015 and 12 March 2016 for the Peruvian study area and 26 images between 3 January 2016 and 28 December 2016 for the Gabonese study area are downloaded. A list of all acquired images can be found in the Annex of this thesis.

4.1.2 Sentinel-2

The Sentinel-2 mission provides high resolution multi-spectral earth observation data for environmental and security monitoring applications. The first Sentinel-2 satellite, Sentinel-2A, was launched on 23 June 2015. Approximately two years later, on 7 March 2017, its twin, Sentinel-2B, followed. The most important key characteristics of the Sentinel-2 mission are listed in Table 4-2. Operating simultaneously in a sun-synchronous near-polar orbit at 786km altitude they maintain a revisit interval of 5 days at the equator. They provide a global coverage of land surface, coastal areas, inland waters and islands larger than 100km² from 56°S to 84°N latitude. The local time of the descending node (LTDN) at 10:30 am is similar to the local times of Landsat and SPOT, enabling the possibility to integrate satellite imagery of all three missions in one combined time series. Consequently, data availability increases leading to improved long-time environmental monitoring. Both Sentinel-2 satellites carry a Multi Spectral Instrument (MSI) with 13 spectral bands at different spatial resolutions covering a wide range of the electromagnetic spectrum. Figure 4-1 depicts the characteristics of the spectral bands. It shows that the three bands sensitive to the visible domain and one sensitive to the near infrared (NIR) domain respectively have a spatial resolution of 10m. To improve vegetation mapping and monitoring, three bands, B5 (705nm), B6 (740nm), and B7 (783nm) with a spatial resolution of 20m are provided which are sensitive to the so called red-edge area of the electromagnetic spectrum as this area provides information of vegetation types and status. With a spatial resolution of 60m, B1 (443nm), B9 (945nm) and

B10 (1380nm) are introduced to enhance atmospheric correction and cloud screening (Aschbacher and Milagro-Pérez, 2012; Drusch et al., 2012; Fletcher, 2012; Main-Knorn et al., 2015; Martimort et al., 2007).

Table 4-2: Key characteristics of the Sentinel-2 mission (Drusch et al., 2012)

Mission characteristics	Data
Mission lifetime	15 years
Number of satellites	2
Nominal in-orbit satellite lifetime	7,25 years with consumables for additional 5 years
Orbit	Near-polar sun-synchronous at 786km (mean altitude), 10:30 LTDN
Land Coverage	57°S to 84°N
Global revisit time	10 days at the equator (one satellite) 5 days at the equator (two satellites)
On-board sensors	Multi Spectral Instrument (MSI)

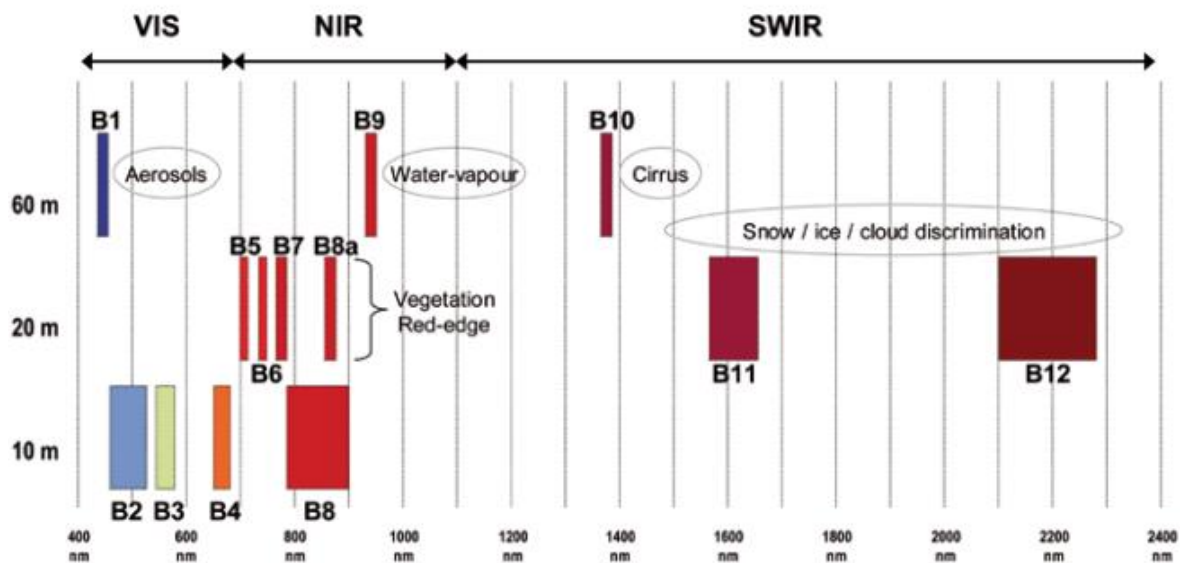


Figure 4-1: Sentinel-2 band characteristics (Fletcher, 2012)

There are different Sentinel-2 data products regarding the data processing level provided for users. Level-1B products include 25km (across track) and 23km (along track) granules (minimum data unit of a product) with Top-of-atmosphere (TOA) radiances in sensor geometry. Level-1C products are orthorectified images in UTM/WGS84 projection covering an area of 100km² with TOA radiance values. Level-2A products as well consist of ortho-images in UTM/WGS84 projection with equal coverage, but pixel values are representing BOA reflectance values. These products are not available directly. Through the provided

Sen2Cor processor Level-2A products can be generated by users, using the available Level-1C product. Further outputs of Level-2A processing are an Aerosol Thickness Map, a Water Vapour Map, a Cloud probabilistic mask, a Snow probabilistic mask and a Scene Classification Map. Additionally, the Sen2Cor processor supports topographic correction of the imagery. To process terrain correction access to the 90m SRTM Digital Elevation Database from CGIAR-CSI and the commercial 90m DEM from PlanetDEM is provided (Drusch et al., 2012; Main-Knorn et al., 2015; Mueller-Wilm, 2017; Suhet, 2015).

For both test sites of this thesis S2 Level-1C products are downloaded, four images between 22 October 2015 and 10 March 2016 for the Peruvian study area and ten images between 15 January 2016 and 16 December 2016 for the Gabonese study area. A list of all acquired images can be found in the Annex of this thesis.

4.2 Landsat 8

With the first satellite successfully launched in 1972, the Landsat satellite mission, which is conducted by the U.S. Geological Survey (USGS) and the National Aeronautics and Space Administration (NASA), provides continuous EO data for more than four decades. Since 2008 the Landsat Programme supports an open data policy, making Landsat data available and accessible free of charge for all users. Due to this temporal extent and the moderate spatial resolution, it is one of the most used satellite data sources regarding mapping and monitoring of land cover and land use dynamics based on image time series. Initially named Landsat Data Continuity Mission (LDCM), Landsat 8, the most recent satellite in the series, has been launched on 11 February 2013 (Roy et al., 2014; Wulder et al., 2012). An overview of the most important Landsat 8 mission characteristics is given in Table 4-3.

Table 4-3: Key characteristics of the Landsat 8 mission (Roy et al., 2014)

Mission characteristics	Data
Nominal in-orbit satellite lifetime	5 years with consumables for additional 5 years
Orbit	Near-polar sun-synchronous at 705km (mean altitude), 10:00 LTDN
Land Coverage	57°S to 84°N
Global revisit time	16 days at the equator
On-board sensors	Operational Land Imager (OLI) Thermal Infrared Sensor (TIRS)

Landsat 8 carries two sensors, the Operational Land Imager (OLI) with nine spectral bands ranging from visible to the short-wave infrared (SWIR) domain of the electromagnetic spectrum, and the Thermal Infrared Sensor (TIRS) with two spectral bands sensitive to the long-wave or thermal infrared domain. A Comparison of spectral band characteristics of the Enhanced Thematic Mapper Plus (ETM+) on board of Landsat 7, OLI and Sentinel-2 MSI is shown in Figure 4-2. All OLI bands have a spatial resolution of 30m except the panchromatic band (15m). Technically, TIRS bands have a spatial resolution of 100m, but are resampled to

30m resolution to maintain data consistency. Compared to the Enhanced Thematic Mapper Plus (ETM+), the sensor carried by its predecessor Landsat 7, OLI has two additional bands, one for coastal and aerosol applications and one to enhance cirrus detection (Roy et al., 2014). Figure 4-2 also shows that corresponding spectral bands of OLI and MSI cover a similar area of the electromagnetic.

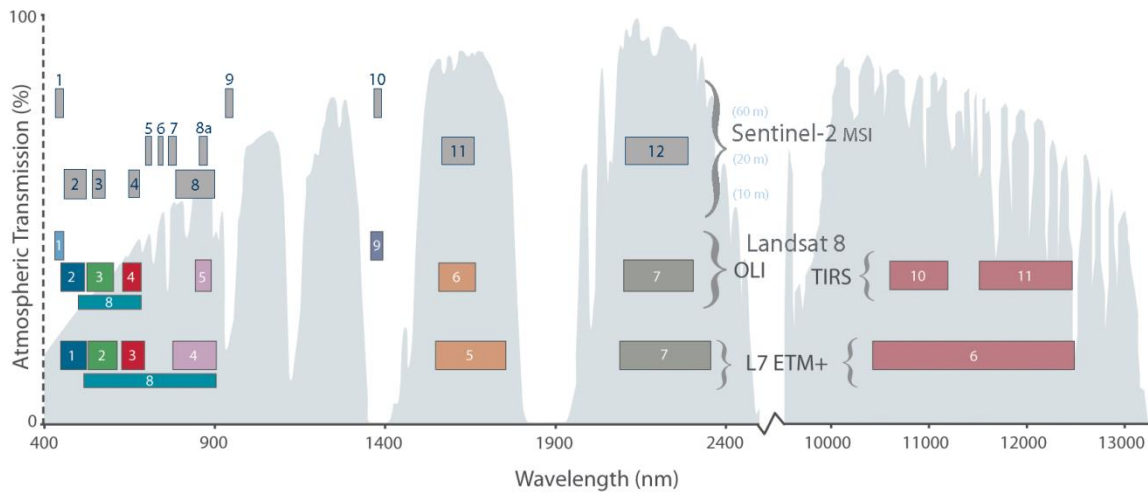


Figure 4-2: Comparison of Landsat 7, Landsat 8 and Sentinel-2 band characteristics (Source: <https://landsat.gsfc.nasa.gov/sentinel-2a-launches-our-compliments-our-complements/>)

Landsat 8 data is available in 2 different processing levels. Both levels provide images in GeoTIFF format with an extent of 185km x 180km referring to the Worldwide Reference System 2 (WRS-2), a gridded system of 233 paths and 248 rows covering the observed areas, which was specifically defined to systematically archive data of the Landsat 4, Landsat 5 and Landsat 7 missions. Level-1 terrain-corrected products (L1T) contain all spectral bands from the OLI and TIRS Sensors in UTM/WGS84 projection. Pixel values represent Digital Numbers (DN). To ensure reliability, land surface studies need data that provide reflectance information of the Earth’s surface. Hence, USGS provides Level-2 products containing all spectral bands with surface reflectance values and three additional bands that provide information about clouds, cloud confidence, pixel saturation and the quality of aerosol retrieval (Irons et al., 2012; U.S. Geological Survey, 2018).

For both test sites of this study L8 Level-2 surface reflectance products are used. 19 images between 20 April 2013 and 23 January 2016 for the Peruvian study area and 9 images between 3 January 2016 and 28 December 2016 for the Gabonese study area are downloaded. A list of all acquired images can be found in the Annex of this thesis.

4.3 Validation Data Sets

To assess the accuracy of classification results, a reference data set representing ground truth is needed. Commonly, if no reference data, either collected during a field campaign or generated through visual interpretation of Very High-Resolution data (VHR), is available,

the collected set of training samples is split and one subset is used for classification and the other one for validation (Lillesand et al., 2015).

For accuracy assessment of the classification results of the Peruvian study area a regular grid of 655 points distributed over the whole study area is generated (see Figure 4-3). All points are visually interpreted using Sentinel-2 and Google Earth data as well as Bing Maps, Planet Explorer and very high resolution (VHR) data from Spot 6 and Rapid Eye sensors. Altogether, 455 out of the 655 points are interpreted being forest and the remaining 191 points representing non-forest. Nine plots cannot be interpreted reliably as no up to date reference data is available leading to a final validation data set of 646 points.

The validation data set for the Gabonese study area is provided by Systèmes d’Information à Référence Spatiale (SIRS), a member of the EOMonDis projects consortium, and produced using the available VHR images which cover 4.75% of the study area (see Figure 4-4). The data set consists of 6000 plots, where 4549 are visually interpreted to represent forest and 1451 representing non-forest.

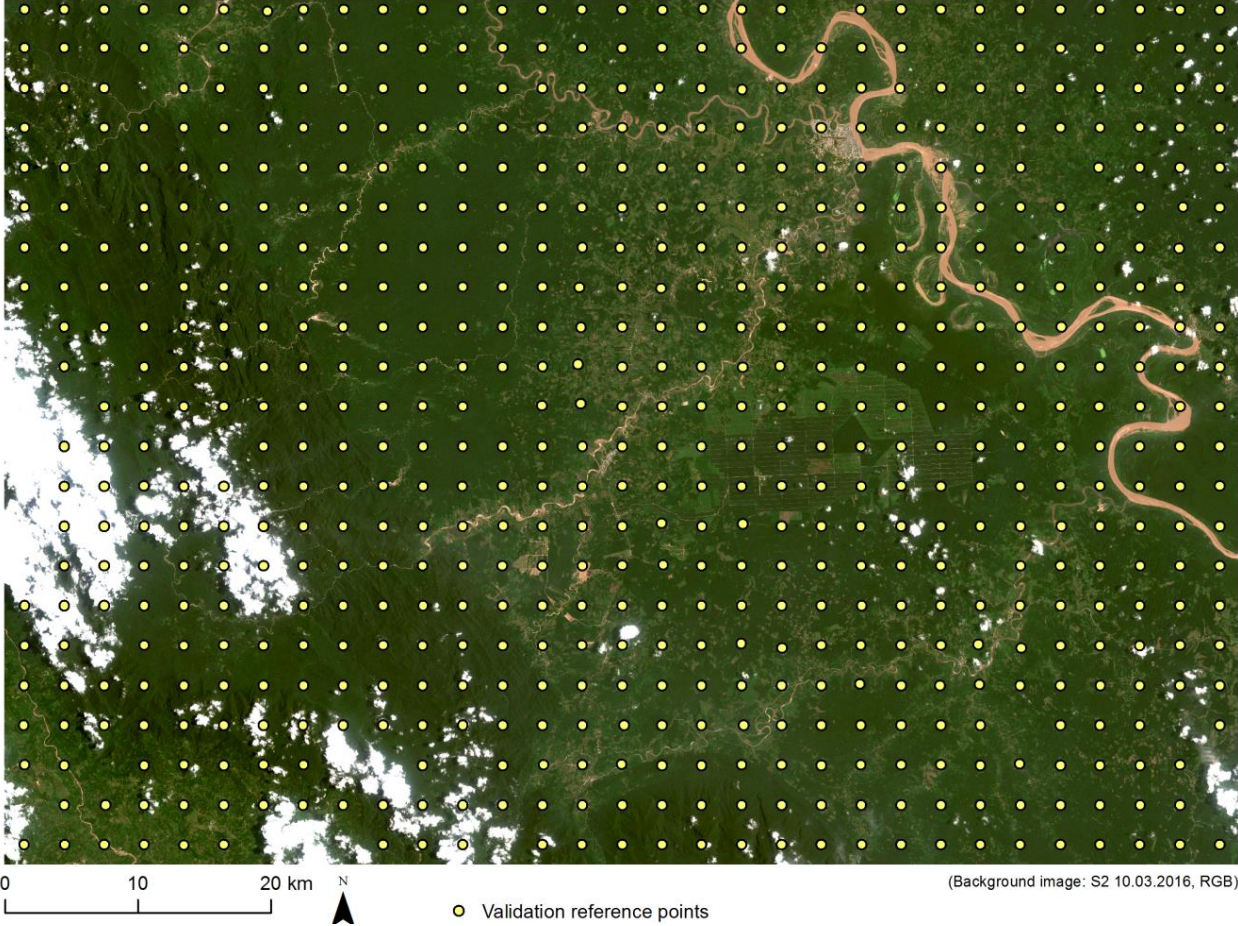


Figure 4-3: Validation data set for accuracy assessment for the Peruvian study area

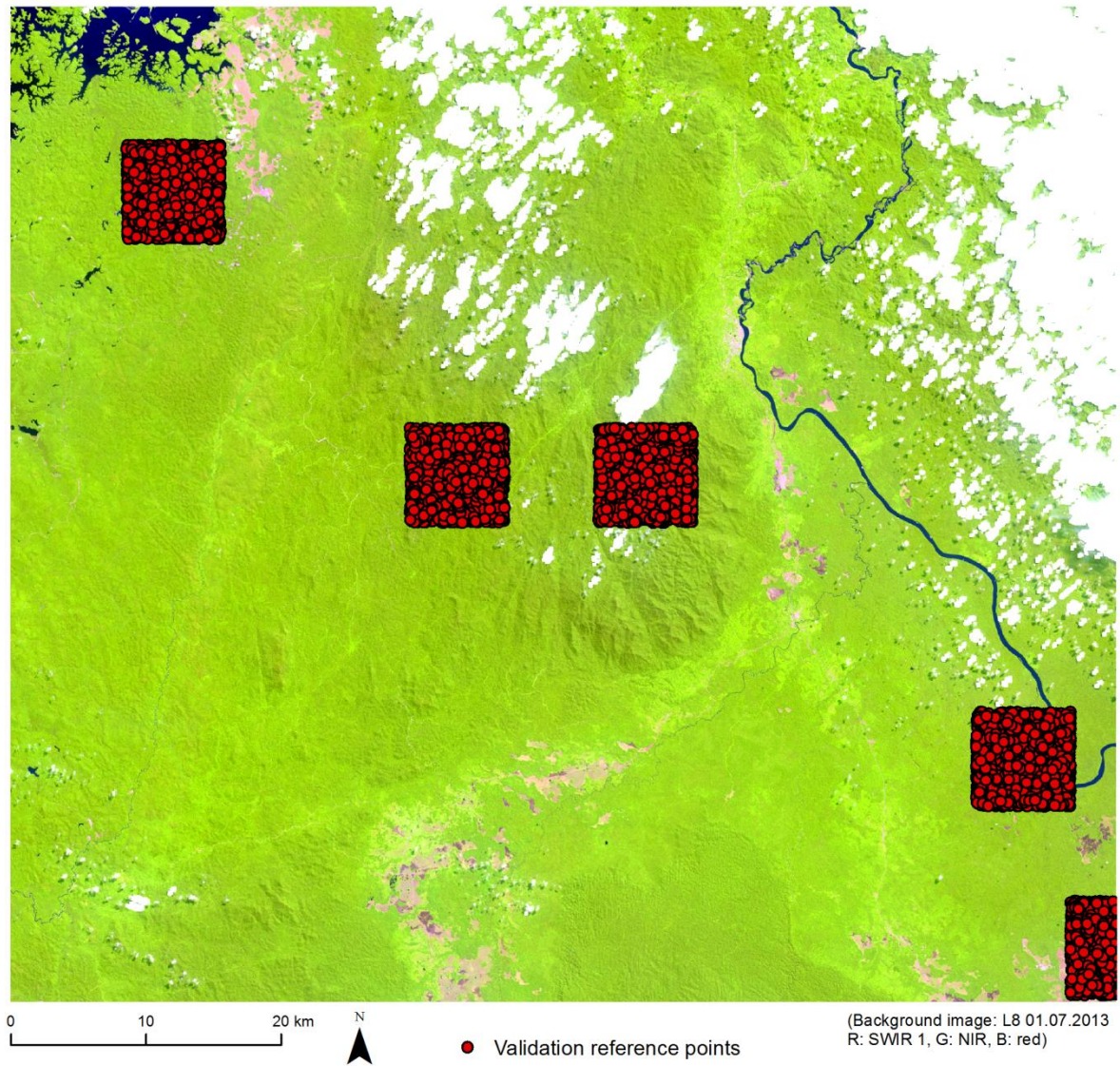


Figure 4-4: Validation data set for accuracy assessment for the Gabonese study area

5 Applied Methodology

This chapter provides a detailed description of all developed and applied forest mapping approaches. A schematic workflow diagram of the entire applied methodology is depicted in Figure 5-1. The utilized Sentinel-1 and Sentinel-2 data are downloaded from the Copernicus Data Hub (<https://scihub.copernicus.eu>) and Landsat 8 Surface Reflectance products are acquired using USGS EarthExplorer (<https://earthexplorer.usgs.gov>). Pre-processing of Sentinel-2 data is done using the Sentinel-2 Reflectance Data Processing module implemented in the JR in-house software IMPACT. In chapter 5.1.1.1 the individual steps are described in more detail. Applied pre-processing steps on Landsat-8 data are explained in chapter 5.1.1.2 and 5.1.1.3. Sentinel-1 data pre-processing is conducted fully automatic using JR RSG software (www.remotesensing.com).

To successfully apply supervised Maximum Likelihood (ML) and Random Forest (RF) classification, a set of training samples is needed for both study areas. These training samples are acquired and evaluated by means of separability analysis using Jeffries-Matusita (JM) distance measure and visual analysis of 2D feature spaces using the Signature Editor module implemented in Erdas IMAGINE software (see chapter 5.2). Erdas IMAGINE is also used to carry out ML classification. RF classification is performed using the Orfeo Toolbox (OTB) version 6.2.0. To ensure comparability, classifications are performed with the exact same classification parameters. Regarding RF classifier, except the tree depth which is set to 10, the default settings provided by the OTB are used.

First, the optical-based mapping approaches are tested. Starting with the result-based approach (see chapter 5.3.1.1), it is investigated if all images of the time series are radiometrically consistent by applying the classification model (ML and RF) based on surface reflectance values of one (reference) scene to the other images and, if not, if relative radiometric adjustment to the reference scene improves mapping results. Furthermore, the impact of the time series extent on classification accuracies is examined. Within the subsequent approaches, merely those images are used which lie within the time series extent that achieves the highest overall accuracy (OA). For the optical data-based approach (see chapter 5.3.1.2) an image stack of all bands of all images as well as the temporal median are utilized as input to calculate classification models. The main reason for using the temporal median only is remaining cloud and cloud shadow pixels in optical data. While the median is robust against outliers other statistical measures, such as minimum, maximum, mean, standard deviation or coefficient of variation, would be affected negatively (Oestreich and Romberg, 2012). Only one data-based approach is developed for forest mapping using SAR time series data (chapter 5.3.2). A mono and a multi-temporal stack of backscatter values as well as an image stack of temporal metrics serve as input variables to perform classification.

Similar to the optical-based approaches, one data-based and one result-based approach is developed to combine optical and SAR time series data for forest mapping (chapter 5.3.3). Those input features that produce the best classification results within the single-sensor mapping approaches are combined in one image stack which is used in a combined optical-SAR data-based approach. The combined result-based approach proposes the combination of two forest probability maps, one derived from optical and one from SAR data, and corresponding forest reliability maps within a Bayesian combination framework.

Accuracy assessment of the classifications results is carried out by means of unbiased error matrices proposed by Olofsson et al. (2013) and conducted using the Verify Classification module implemented in the JR in-house IMPACT software (chapter 5.4).

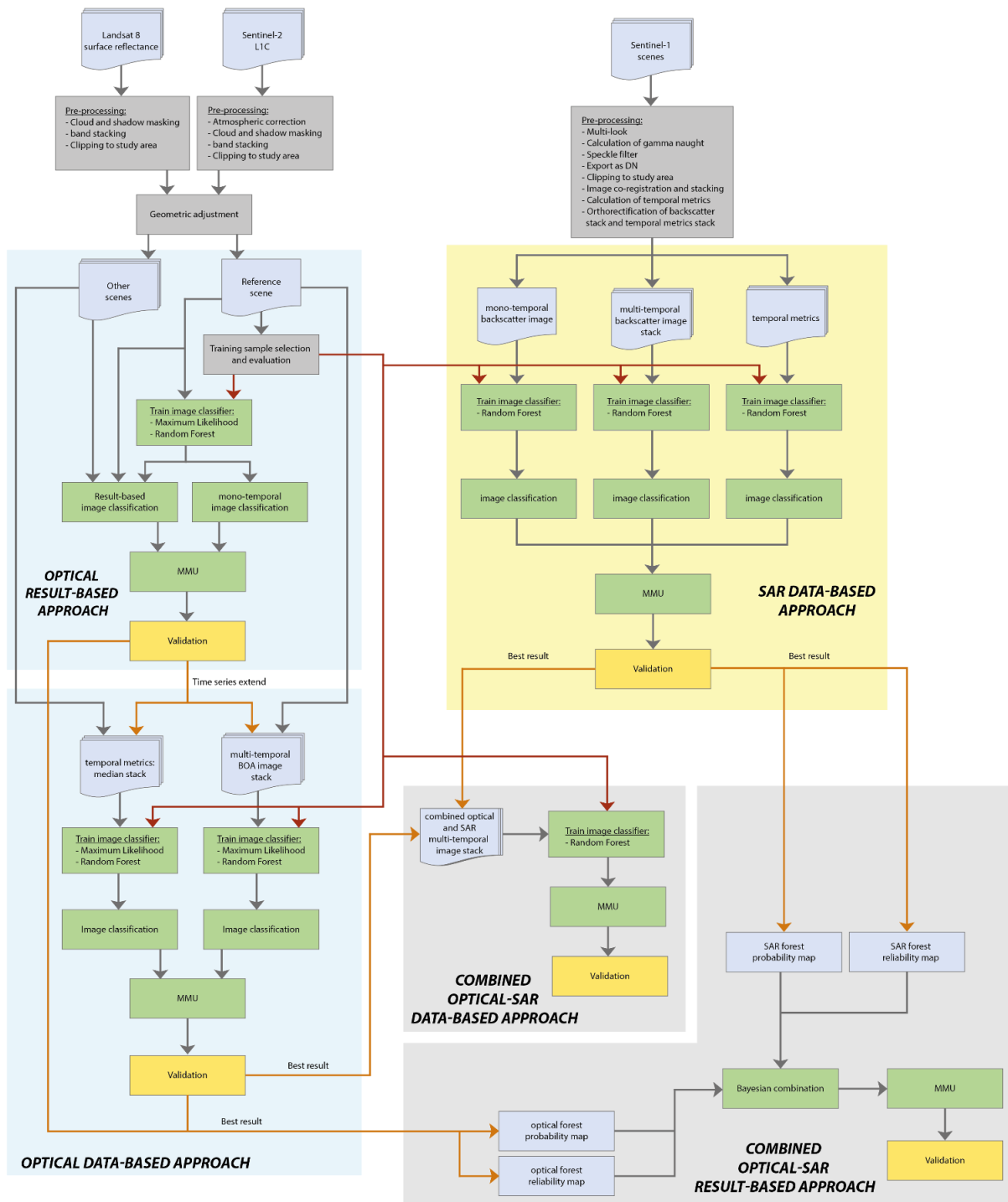


Figure 5-1: Workflow diagram of the applied approaches

5.1 Data Pre-processing

5.1.1 Optical Data

5.1.1.1 Sentinel-2

First, all downloaded Level-1C S2 images are atmospherically corrected to surface reflectance values using the Sen2Cor processor provided by ESA. To obtain BOA reflectance values the radiative transfer in the earth’s atmosphere needs to be modelled. Therefore, the Sen2Cor processor includes the libRadtran library (Richter et al., 2011), which allows to calculate radiances, irradiances and actinic fluxes in the solar and thermal spectral regions for different sensor and solar geometries, ground elevations, and atmospheric parameters (Emde et al., 2016) and stores them in Look up Tables (LUTs). The Sen2Cor processor allows the user to choose between two different aerosol types (rural and maritime) and two different types of atmosphere (mid latitude summer or mid latitude winter) as well as selecting between predefined ozone concentrations which influences the calculation of the look LUTs (Mueller-Wilm, 2017). Due to the location of the two test sites in Peru and Gabon, the aerosol type is set to rural. As all S2 scenes from one test site are processed together, the atmosphere type and ozone content is set to AUTO, leading to an automatic determination by the algorithm (Mueller-Wilm, 2017). Only those bands with 10m and 20m spatial resolution (see Figure 4-1) are atmospherically corrected, the 60m bands will not be included in the classification process. The 20m bands are resampled to 10m.

To avoid misclassifications, clouds and cloud shadows must be masked out prior to classification. Within the process of atmospheric correction, the Sen2Cor processor also generates a scene classification map with 20m spatial resolution consisting of 11 different classes (Mueller-Wilm, 2017) which are listed in Table 5-1.

Table 5-1: Classes of the scene classification map (Mueller-Wilm, 2017)

Label	Class
0	No Data
1	Saturated Or Defective
2	Dark Area Pixels
3	Cloud Shadows
4	Vegetation
5	Not Vegetated
6	Water
7	Cloud Low Probability
8	Cloud Medium Probability
9	Cloud High Probability
10	Thin Cirrus
11	Snow

According to (Mueller-Wilm, 2017), the Sen2Cor scene classification algorithm is mainly based on threshold operations using different single spectral bands, band ratios and indices,

like for instance the Normalized Difference Vegetation Index (NDVI) and the Normalized Difference Snow Index (NDSI), and includes 5 different steps: (1) snow detection, (2) cloud detection, (3) cloud shadow detection (4) cirrus detection and (5) classification map generation. Additionally, snow and cloud probabilities, which serve as quality indicators, are calculated (Mueller-Wilm, 2017). This scene classification map provides the basis for cloud masking as three cloud classes and one shadow class are provided. In the first step, the classification map is resampled to 10m spatial resolution. Then the classes are recoded to a binary image mask consisting of the integer values 1 (no cloud) and 2 (cloud). Within the implemented default settings, only pixels either flagged as class 8 or class 9 are considered as clouds, but classes 3 (cloud shadow), 7 (cloud low probability) and 10 (thin cirrus) may be included optionally. This binary image is then further processed by applying an erode operation on cloud regions using 5 pixels to eliminate small elongated cloud areas as these patches frequently represent water regions that are misclassified as cloud shadows. A dilate operation on cloud regions using 5 pixels is performed next to close small no-cloud patches within clouds. Additionally, the user can define a minimum cloud size in pixels. All cloud patches smaller than the selected threshold are removed. A second dilate operation can optionally be performed after that, to close gaps between cloud areas. Finally, non-cloud areas within clouds that are smaller than a user defined number of pixels can optionally be removed as they usually represent clouds too. The applied parameter settings to generate the cloud and cloud shadow mask are adapted for each image individually. The last process comprises the assignment of no-data to all pixels of the image stack which are clouds according to the generated cloud mask. The final pre-processing step of S2 data is the adaption of extent of all images to the extent of the study areas.

5.1.1.2 Landsat 8

Pre-processing of L8 data is not as much time consuming as S2 data due to the availability of L8 Level-2 surface reflectance products. The separately delivered bands of each date are stacked to one image and cloud areas are set to 0 according to the cloud mask. The available cloud mask is computed using the CFMask algorithm which is the C version of the Function of Mask (FMask) algorithm developed by (Zhu and Woodcock, 2012), originally implemented in a Matrix Laboratory environment (MATLAB) and performs an automated object-based cloud and cloud shadow detection in Landsat images (U.S. Geological Survey (USGS), 2018; Zhu and Woodcock, 2012). The FMask algorithm is based on a set of rules to test spectral characteristics to identify potential cloud, cloud shadow and snow pixel. Single spectral bands as well as band ratios, indices and other band combinations are used. Subsequently, potential cloud objects are identified via segmenting the potential cloud layer generated in the first step. Based on the assumption that a cloud and the corresponding cloud shadow have similar shapes and that the sensors view angle, the solar zenith angle, the solar azimuth angle, and the relative height of the cloud are known, location and shape of the cloud shadow is computed (Zhu and Woodcock, 2012). In the last step, the extent of the L8 images is adapted to the study area.

5.1.1.3 Geometric and Radiometric Comparison of Sentinel-2 and Landsat 8

If imagery acquired by different sensors is used in a combined time series data set, geometric consistency is a requisite, because geometric errors almost certainly lead to misclassifications

(Kuenzer et al., 2015). Hence, a visual analysis of the L8 and S2 images is performed to check for geometric errors. Possible errors are corrected using a fully automated multi-modal image matching algorithm that is based on the concept of mutual information maximization to register the L8 scenes to the S2 images. For further information on the algorithm the reader is referred to (Perko et al., 2011).

Generally, to successfully classify different types of LCLU using optical images of different sensors, they do not only need to be consistent regarding their geometry, but also their radiometry. This means that the grey values of the different spectral bands representing a certain thematic class should be similar in all images of the time series, unless a land cover or land use change occurred between the observation dates. As the study areas used in this thesis are located in the humid tropical domain where atmospheric conditions are highly variable and clouds are frequent, it is not possible to select time-stable reference areas that are not influenced by phenology for detailed and reasonable radiometric evaluation across the entire time series. Hence, radiometric consistency is evaluated within the first classification tests using the optical-based mapping approach. Therefore, the same classification model is applied to all images of the image time series using both, radiometrically calibrated as well as not calibrated images. The used method to perform relative radiometric adjustment, implemented in the Impact Toolbox of JR, relies on linear regression. To calculate the coefficients of the regression model the program uses so-called pseudo-invariant features, which can either be defined by an additional mask or they are derived in an automated process based on the evaluation of the correlation coefficient within a certain window size. This enables the use of images with remaining clouds for relative radiometric calibration.

5.1.2 SAR Data

The applied S1 pre-processing workflow is adopted from an existing workflow proposed by (Deutscher et al., 2017) which has already been successfully applied to another study carried out within the frame of the EOMonDis project (Hirschmugl et al., 2017a).

The first step of the pre-processing algorithm chain includes data ingestion and orbit parameter updating which is important for geometric accuracies of the images. To reduce terrain effects on the radiometry, the SRTM DEM is used next to process the backscatter coefficient to gamma naught (γ^0). Usually, the grey value of a single pixel is a combination of many observed scatterers and is described using the backscatter coefficient sigma naught (σ^0) which equals the sum of radar cross sections of all scatterers per unit ground area (Bamler, 2000). To calculate γ^0 the reference area is projected in the plane perpendicular to the line of sight from the sensor (Small, 2011). To reduce speckle noise multi-looking to 10m is performed and a modified Frost filter with a 3x3 window is applied. To perform multi-looking *“several independent images of the same area, produced by using different portions of the synthetic aperture, are averaged together to produce a smoother image”* (Lillesand et al., 2015).

The process of multi-looking averages several images of the same area obtained by splitting the synthetic aperture into different portions together to generate a smoother image (Lillesand et al., 2015). A Frost filter replaces the central pixel of moving window with the weighted sum of adjacent pixels that lie within the moving window. To calculate weighting factors, the distance from the central pixel as well as the grey value variance within the entire

kernel are taken into account (Frost et al., 1982). More information on different speckle filters can be found in (Lee et al., 1994) or (Sheng and Xia, 1996). Then the images are exported as digital numbers (DN) and image co-registration and image stacking is performed. Additionally, a multi-temporal filter is applied to further reduce speckle noise (Quegan, 1998). For the resulting image stack the following temporal metrics are calculated: minimum, maximum, mean, median, standard deviation and coefficient of variation resulting in an image stack of six bands, one for each statistical value. The last step includes orthorectification of the backscatter image stack and the statistics file based on the SRTM DEM. Due to highly variable and unfavourable local incidence angles in mountainous regions as well as the lower spatial resolution of the SRTM (approximately 30m) compared to S1 data it is to be expected, that geometric correction in those areas will be of lower accuracies.

5.2 Training Data Selection

There are some issues that need to be considered when using the same set of training samples to classify all images of an optical time series individually. First, possible land use changes that may occur between observations might change the class a training sample is representing. Moreover, due to cloud and cloud shadow pixels, it is not possible to use the whole set of training samples acquired at one date to classify the other images. Therefore, every image would be classified with a different subset of the available training samples. Furthermore, it might also be possible that not enough training samples would remain for some classes. To overcome this issue, the idea is to use the least cloudy image as reference scene to collect training samples including only valid pixels and train the image classifier. This ensures that the calculation of the classification model is not influenced by atmospheric conditions or missing values. The same classification model is then used to classify all other images.

It needs to be mentioned that this method may hold some sources of errors. One is phenology of different crop types. The fact that only one observation is used to collect training samples and calculate the classifier makes it difficult to cover all phenological stages in the classification model. However, phenology of crops does not show a characteristic annual cycle as climatic conditions in humid tropical regions do not vary as significantly within a year. Therefore, the phenological stage of some crops mainly depends on the time of planting and harvesting. Hence, it is possible to cover more than one phenological stage of the same crop type when using one image for training sample collection. Nonetheless, it is highly impossible to generate a classification model that covers all phenological stages.

As mentioned in chapter 1.2, within the EOMonDis project not only forest status maps, but also land use maps representing the six main IPCC land use classes *forest*, *cropland*, *grassland*, *wetlands*, *settlements* and *other land* (IPCC, 2003) are produced. Hence, the training data is selected and labelled according to IPCC land use class definitions. Sample selection is supported by visually interpreting additional VHR images as well as ESRI basemap, Google Earth, Google Street View and Bing Maps data. The resulting land use classification maps are reclassified to the classes *forest* and *non-forest* in a post-classification process to generate a forest status map. The same set of training samples is used within every classification approach.

Separability analyses are performed to evaluate the potential of the selected training areas to discriminate the different land cover classes in the spectral bands. Therefore, Jeffries-Matusita (JM) distance and visual analysis of the feature space representations is performed using the Erdas IMAGINE 2014 software. JM distance is used to measure the spectral separability between two classes. The calculation integrates the mean values as well as the dispersion of values about the mean value through covariance matrices (Appiah et al., 2015; Daboor et al., 2014). According to the ERDAS Field Guide™ (1999), the Jeffries-Matusita distance ranges between 0 and 1414. The higher the distance value the better the classes are separable. A JM distance of 0 indicates, that classes are inseparable (Appiah et al., 2015).

5.3 Tropical Forest Mapping Approaches

5.3.1 Optical Time Series Approach

As stated in chapter 1.2, two different forest mapping approaches are investigated: a result-based and a data-based approach, which will be described in the following chapters 5.3.1.1 and 5.3.1.2 in more detail. Within both optical approaches the ML as well as the RF classifier is used for supervised image classification, to test their performance and reveal their limits when optical multi-temporal data sets are involved.

5.3.1.1 Result-based Approach

The result-based approach comprises image combination on a semantic level which means that mono-temporal classification of each image of the time series is performed and then the resulting forest/non-forest maps are then combined. A schematic overview of the entire processing chain is depicted in Figure 5-2. The classification model of one reference scene is used to generate mono-temporal forest/non-forest maps of all images of the time series. However, this processing chain implies radiometric consistency and increases the importance of adequate data pre-processing and also stable phenology. Therefore, this step is performed using the original as well as relatively radiometric calibrated images. By visually analysing the resulting classifications, a decision is made if the original or the calibrated images will be used. Input data for the mono-temporal classifications is limited to BOA reflectance values, no additional derived features are used, like for example indices or principal components.

Once the individual classifications are available, the post-classification analysis step can be performed. Let n be the number of used images within the classification process. To generate a combined forest/non-forest map, the n generated mono-temporal forest/non-forest maps are fused in a post-classification analysis based on the calculation of the proportion of forest votes on valid observations. Each pixel has a certain number x of valid classification results depending on image cloud masks, with the maximum number corresponding to n . Furthermore, each pixel has a certain number y of votes for the class forest, ranging from 0 to n . Once x and y are determined for each pixel, they are used to calculate the proportion z of forest votes y on the number of valid pixels x :

$$z = \frac{y}{x} \quad (1)$$

For the final forest/non-forest map a proportion threshold s applied, which means that all pixels with a forest proportion equal or greater than the selected threshold are considered to represent forest and all pixels with a forest proportion lower than the selected threshold are considered to represent non-forest.

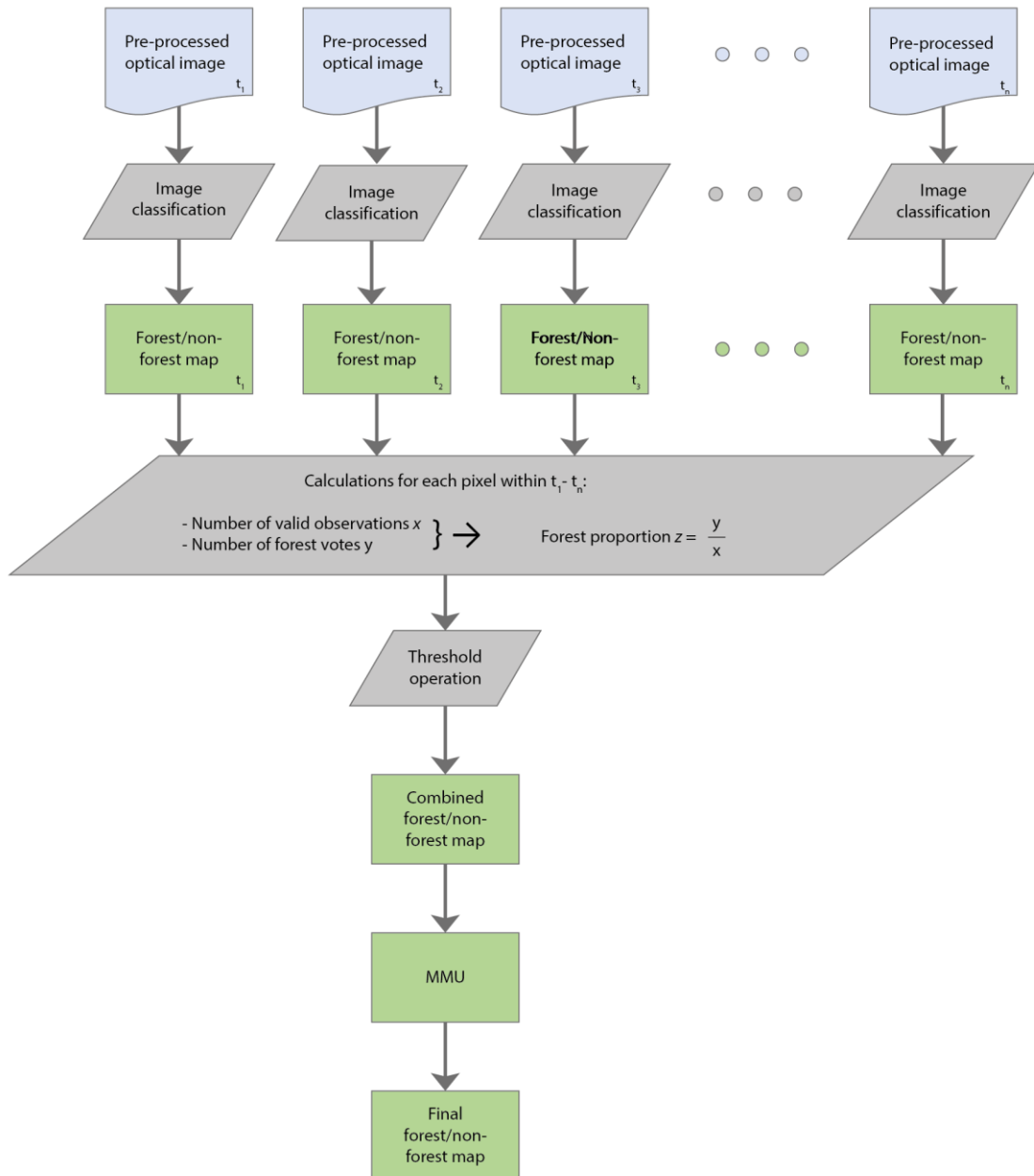


Figure 5-2: Schematic diagram of the result-based approach

A forest status map should be as representative as possible for the specific date or period it is generated. Insufficient data availability at a specific date forces the need to use images that of

a much earlier or later date. However, the further an observation date deviates from the desired status date or period, the higher the probability becomes that LCLU changes occur between these two dates. This results in misclassifications. Hence, the above described result-based approach is conducted using all observations from 2013, where the first OLI images are available, as well as a reduced time series build on only those images acquired within one year.

Forest regeneration might cause classification errors within the proposed result-based approach as illustrated in Figure 5-3. This figure shows the forest votes for one specific pixel within a time series from 2013 to 2016, where 0 denotes a non-forest vote and 1 denotes a forest vote. For simplicity, the number of valid observations corresponds to the number of images. If all available data is used to derive the forest status of 2016, the corresponding forest proportion on valid observations for this pixel is 45%. Hence, in the final forest/non-forest classification map, this pixel is assigned to the class non-forest. A closer look reveals that most of the forest votes are detected during the years 2015 and 2016. This might indicate that the LU class this pixel represents changed from non-forest in 2013 and 2014 to forest due reforestation activities in 2015. Reducing the image time series to observations from 2015 and 2016 leads to a forest proportion of 70%. This reflects the forest status of 2016 much better.

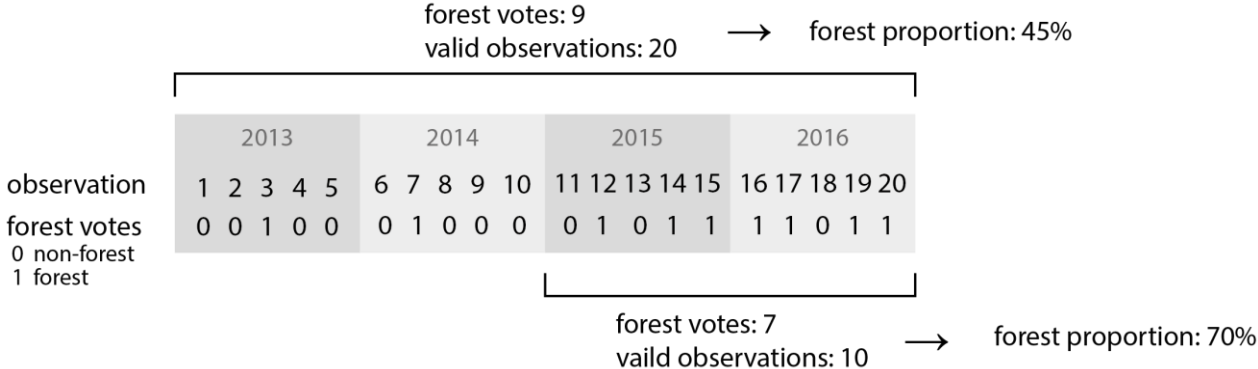


Figure 5-3: Classification example showing a forest regeneration pattern

Of course, this pattern of forest regeneration might also occur in a shorter interval (between 2015 and 2016). A further reduction of the extent of the time series to overcome this issue might not be reasonable as not enough images might remain. Therefore, two different weighting functions are introduced to assign recent observations more influence on forest status mapping than earlier ones. Within the first setting, the time series, which is reduced to observations that lie within one year, is divided into two periods of six months where the observations of the second period are weighted twice as high. To illustrate this more clearly, it is assumed that all observations in Figure 5-3 lie within one year and the first 10 observations within the first six months and the other 10 observations within the second six month. Considering the weighting, the number of forest votes within the second period is doubled from 7 to 14. Now, instead of 9, 16 forest votes are detected within the entire time series. To overcome the issue of receiving a forest proportion greater than 100% also the number of valid observation within the second period is doubled, leading to 30 valid observations. Calculating the forest proportion with the weighted values leads to a result of

53.3% and a forest label in the final classification map. The second weighting divides the time series into three periods of 4 months and assigns double weight to the second and triple weight to the third period.

Altogether 10 different forest mapping results, 5 per classifier, are obtained within the optical result-based approach:

1. Mono-temporal classification
2. Multi-temporal classification (entire available time series)
3. Multi-temporal classification (reduced time series)
4. Multi-temporal classification (reduced time series weighted, 2 periods)
5. Multi-temporal classification (reduced time series weighted, 3 periods)

The highest overall accuracy produced for the result-based approach determines whether the entire available image time series or the reduced time series is used in the following optical data-based approach.

5.3.1.2 Data-based Approach

In contrast to the result-based approach which combines the time series in a post-classification process, the data-based approach combines the time series data before the classification. It is performed by generating a time series image stack consisting of all bands of all surface reflectance images. Technically, to obtain a reliable and accurate classification result when surface reflectance images from multiple dates are used to calculate a ML or RF classification model, time-stable training samples, e.g. they should represent the same thematic class in all images, that do not contain no-data pixels, are needed. In fact, frequent cloud cover within humid tropical regions makes it impossible to generate such a training data set for a multi-temporal image stack. Unfortunately, the lack of adequate handling of missing values during the training process of the classifier as well as the classification process itself is a problem of the available software for ML and the RF classification. Reasons for that can be found in the principal design and functionality of the classifiers. Only a single no-data pixel within a training sample makes it impossible for the ML classifier to calculate statistics for that sample, hence omitting that training sample in the training process. The ML classifier is based on the calculation of distances in an n-dimensional feature space, where n corresponds to the number of bands used to generate the classification model. Therefore, it is impossible for the classifier to calculate the distance of a pixel with n-1 valid values in the image stack to the mean values of the thematic classes. Hence, it is not possible to perform ML classification with the BOA reflectance image stack. Regarding the RF classifier, although it can handle missing values during training process (Breiman, 2003), the generated classifier cannot deal with missing values in the data during the classification process properly (Ishwaran et al., 2008). However, a classification result can still be obtained. Therefore, RF classification is performed with the BOA reflectance image stack but the probability of classification errors is very high.

To overcome this issue of missing values the median for each pixel across the entire time series is calculated separately for all spectral bands. The result is an image stack consisting of 10 bands. The main reason for using solely the median and none of the other statistical measures, such as minimum, maximum, mean or standard deviation, is that the median is not sensitive to outliers and therefore provides a more reliable measure (Oestreich and

Romberg, 2012). As no-data pixels only remain when there is no valid observation throughout the whole image time series, the number of no-data pixels is reduced immensely. Hence, ML as well as RF classification is conducted with the temporal median image stack. However, it needs to be mentioned that for those bands that are provided by L8 and S2 data the number of bands available for the calculation of the temporal median corresponds to the number of all acquired optical images. But it might be possible that for the four bands that are only provided by S2 (three red-edge bands and the second NIR band) larger no-data areas due to clouds remain as viewer images are available to calculate the temporal median. This might result in larger areas that cannot be classified by the ML classifier. Additionally, RF classification is carried out with an input image stack consisting of all BOA reflectance images and all temporal median bands to investigate whether the combination contributes to improve classification accuracies.

5.3.2 SAR Time Series Approach

The approach to generate a forest/non-forest map based on a SAR image time series resembles the optical data-based approach due to the fact that the SAR image time series is also combined before the classification. On the one hand, all acquired S1 backscatter images are combined in one image stack and used as input for a classification. On the other hand, temporal statistics are calculated for the multi-temporal SAR image stack as they may reveal specific patterns leading to a better separability of forest and non-forest areas. The statistical values calculated are minimum, maximum and mean backscatter values, standard deviation and coefficient of variation. In contrast to optical data, these statistical metrics are reliable since there are no missing values in SAR data due to clouds or cloud shadows. Which classifier is used depends on previous optical classification results as only the classifier producing the highest overall accuracy will be employed. For completeness as well as the purpose of comparison, also a mono-temporal classification is performed. However, backscatter signals from leaves and small branches of trees show very similar patterns to other vegetation types. Thus, the preliminary assumption can be drawn that mono-temporal SAR image classification will not produce an accurate forest status map.

5.3.3 Combined Optical-SAR Time Series Approach

Analogue to the optical-based approach, forest mapping with a combination of SAR and optical time series data is performed using a data-based approach as well as result-based approach which combines two separately generated forest/non-forest maps.

For the **data-based approach**, which equals the optical and the SAR data-based approaches described in the previous chapters, optical and SAR imagery is combined in one image stack. Whether optical surface reflectance or temporal median data on the one hand and SAR backscatter or statistical values on the other hand are used, depends on the previously performed single-sensor approaches. The data sets producing the best results are included in the combined data-based approach. Classification is performed using the RF classifier, even if within the optical data-based approach it turns out that the ML classification of the temporal median produces the best classification result.. Reason for this is the fact that no

classification result can be obtained for no-data pixels in the optical median although the SAR data does provide reliable information for those pixels.

The combined **result-based approach** is based on the principles of Bayes' theorem which states that the conditional probability of an event can be calculated considering given a priori conditions that might be related to this event (Koch, 1990). This fact is described in the following equation:

$$P(A | B) = \frac{P(B|A) + P(A)}{P(B)} \quad (1)$$

Where A and B are events, P(A) and P(B) are the probabilities to observe A and B, P(A|B) is the conditional probability that A occurs given that B is true and P(B|A) is the conditional probability that B occurs given that A is true. Based on the approach proposed by (Reiche et al., 2015a), Hirschmugl et al. (2018) developed a Bayesian combination approach to combine two conditional probability maps. Therefore, probability maps are generated for optical and SAR time series data separately using so-called probability density functions (pdfs) (Reiche et al., 2015a) which are calculated using training data for the desired classes (Hirschmugl et al., 2018). Additionally, this approach supports the integration of reliability maps. The measurement for the reliability of a map used within this thesis is the overall accuracy derived by means of unbiased error matrices. Once probability and reliability maps have been generated, they are combined using the following equation:

$$P(c | F) = \frac{P(o|F)R(o|F) + P(s|F)R(s|F)}{(R(o|F) + R(s|F))} \quad (2)$$

Where P(o|F) is the conditional forest probability of optical map, P(s|F) is the conditional forest probability of SAR map, R(o|F) and R(s|F) are the reliabilities of the optical and SAR probability maps respectively and P(c|F) corresponds to the combined probability of both maps. The combined forest probability map is converted to a forest/non-forest map by defining a probability threshold of 50%.

5.4 Accuracy Assessment

The accuracy assessment to quantify the agreement between mapping results and the available reference plots described in chapter 4.3 is based on unbiased confusion matrices proposed by Olofsson et al. (2013). Instead of using standard count-based confusion matrices to calculate Overall Accuracy (OA) as well as User's and Producer's Accuracies (UA and PA), this approach corrects the accuracy measures by integrating the proportion between the mapped area of classes (A_i) and total mapped area (A_{tot}). Therefore, the value of each cell of the count-based error matrix is adapted using the following formula (Olofsson et al., 2013):

$$\hat{p}_{ij} = \frac{A_i}{A_{tot}} * \frac{n_{ij}}{n_i} \quad (3)$$

Where n_{ij} denotes the count-based value of the cell with row index i and column index j , n_i corresponds to the total number of points mapped as class i and \hat{p}_{ij} denotes the corrected cell value. Hence, all validation points receive a weight depending on the area proportion of the class they represent. Consequently, considering a point of the validation set which represents a class with a large area proportion on total mapped area, incorrect classification of this point has a greater impact on accuracy than a falsely mapped point of a class with a smaller area proportion. Accuracy measures derived from the new error matrix are calculated using the following formulas (Olofsson et al., 2013):

$$OA = \hat{p}_{11} + \hat{p}_{22} + \dots + \hat{p}_{qq} \quad (4)$$

$$UA = \frac{\hat{p}_{qq}}{\hat{p}_{.q}} \quad (5)$$

$$PA = \frac{\hat{p}_{qq}}{\hat{p}_{.q}} \quad (6)$$

Where \hat{p}_{qq} denotes to the unbiased value of correctly mapped points of class q , $\hat{p}_{.q}$ corresponds to the unbiased value of the total number of points representing class q according to the map and $\hat{p}_{.q}$ corresponds to the unbiased value of the total number of points representing class q according to the validation data set.

6 Results and Discussion

6.1 Peruvian Study Area

The Peruvian study area is used to investigate the performance of all approaches and their different settings described in chapter 5.

6.1.1 Data Pre-Processing

Atmospheric correction and cloud-masking of Sentinel-2 data

Figure 6-1 depicts an example of a S2 scene before (a) and after (b) the application of atmospheric correction and cloud-masking to eliminate cloud and cloud shadow pixels. Compared to the Level 1C product, the surface reflectance image shows a significant haze removal. Regarding the cloud mask (black areas in the right picture), there are three visible deficiencies. First, the algorithm fails to detect small clouds, secondly, detected clouds are not masked completely (indicated by the white edges around the black masked areas) and thirdly, not all masked pixels really do represent clouds, e.g. the river in the eastern part of the scene. The reason for that lies in the inaccuracy of the Sentinel-2 scene classification, as the classification algorithm frequently assigns pixels that represent water bodies to the class *cloud shadows* and bare soils to the class *clouds*.

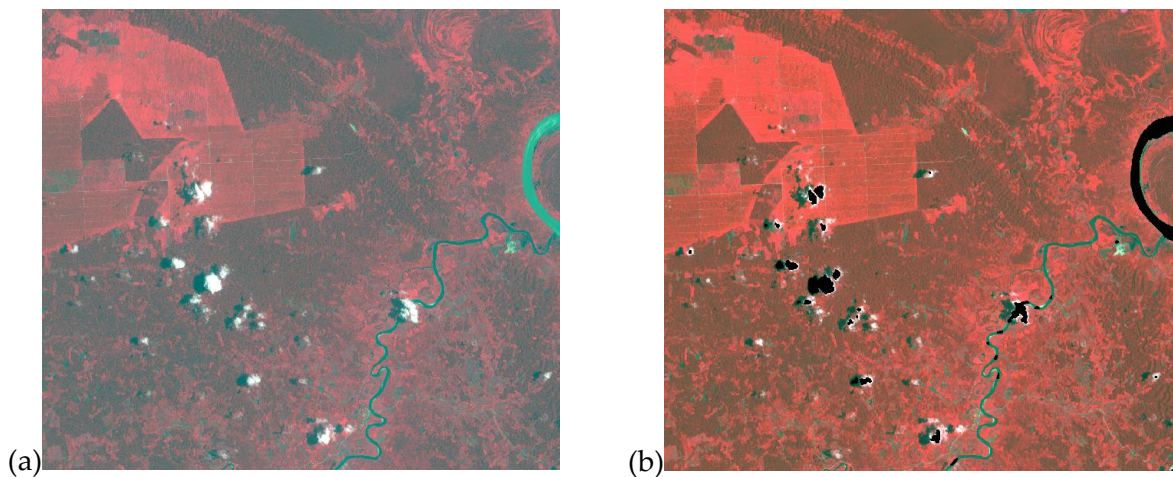


Figure 6-1: Results of atmospheric correction and cloud-masking of S2 data (10.03.2016; R: NIR, G: red, B: green): (a) Level 1C TOA, (b) Level 2A BOA. Both images have the same look up table stretch (black pixels: cloud mask)

Geometric evaluation of S2 and L8

To avoid classification errors due to geometric distortion, S2 and L8 scenes are visually analysed regarding their geometric consistency. Figure 6-2 (a1) and (a2) reveal a significant north-south shift between the images. Hence, geometric adjustment using the proposed multi-modal image matching algorithm, with the S2 scene as reference, is applied to all

acquired L8 scenes. The results are shown in Figure 6-2 (b1) and (b2) and indicate a successful geometric correction.

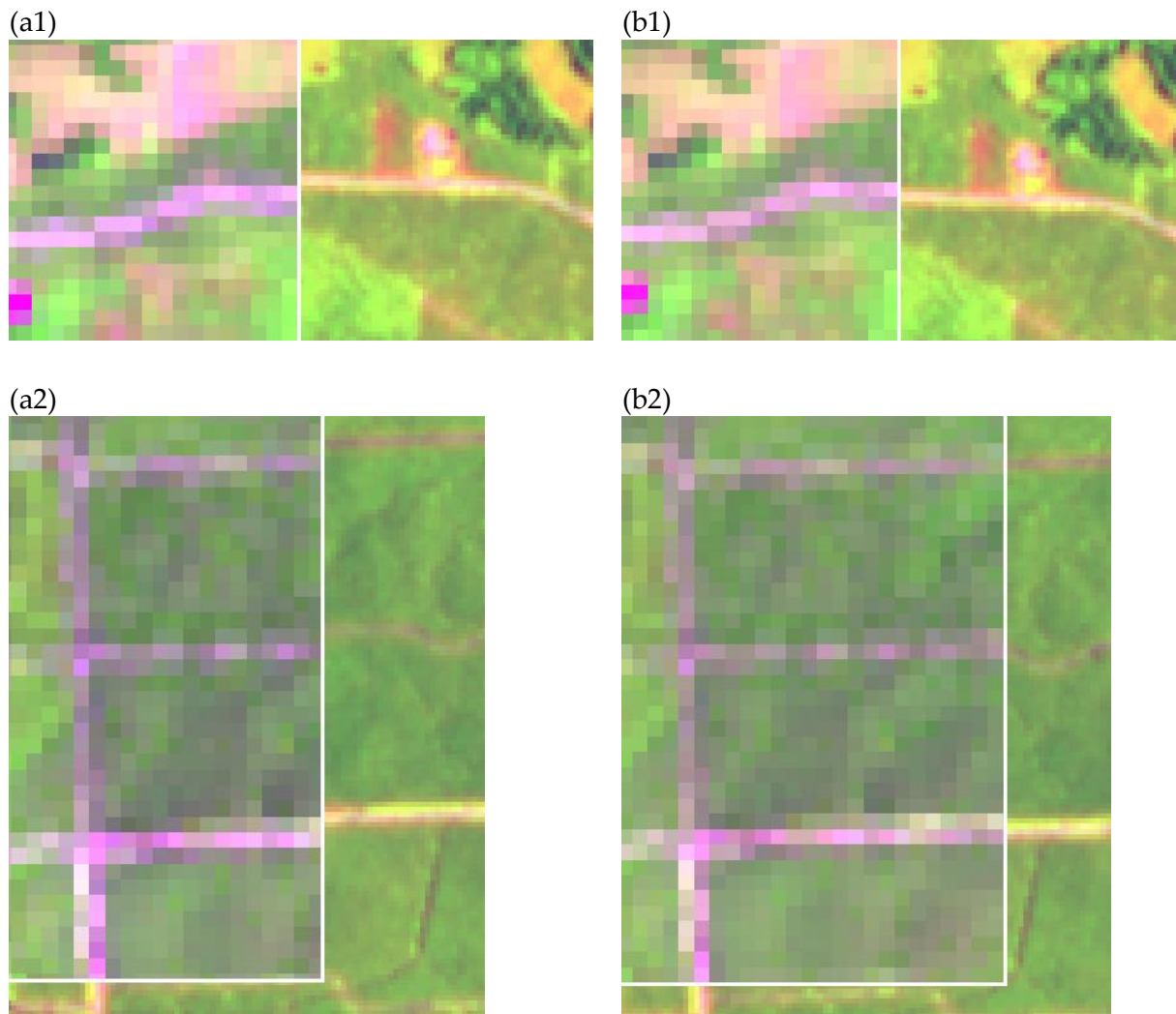


Figure 6-2: Comparison of Sentinel-2 and Landsat 8: (a) prior and (b) after geometric adjustment

Pre-processing of S1 data

Pre-processing of SAR data has been done according to the description in chapter 5.1.2. Figure 6-3 and Figure 6-4 show the different stages of pre-processing of a subset of the S1 scene from 12.03.2016. Comparing the SAR image before (Figure 6-3 (a)) and after (Figure 6-3 (b)) radiometric calibration to gamma naught and the application of a Modified Frost filter and orthorectification (Figure 6-3 (c)), SAR geometry effects, especially shadow effects are reduced significantly. However, they do remain in the mountainous area. Regarding speckle noise, a considerable reduction is achieved with the application of the Modified Frost filter (Figure 6-4 (a)). Figure 6-4 (c) reveals a slight additional speckle noise reduction after the application of the multi temporal filter.

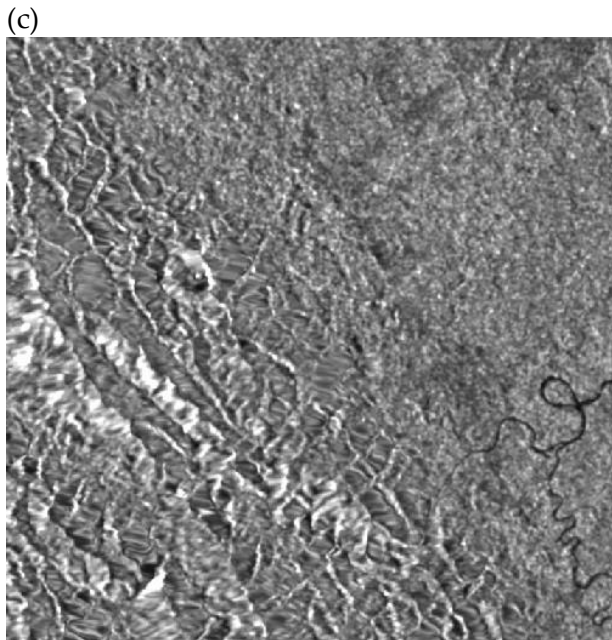
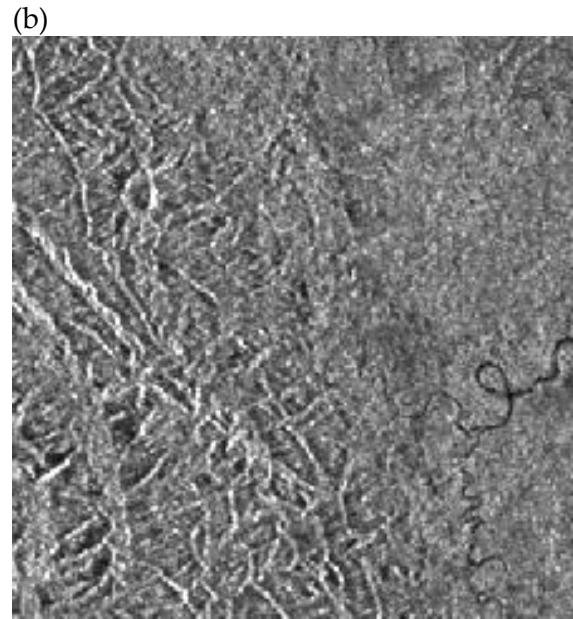
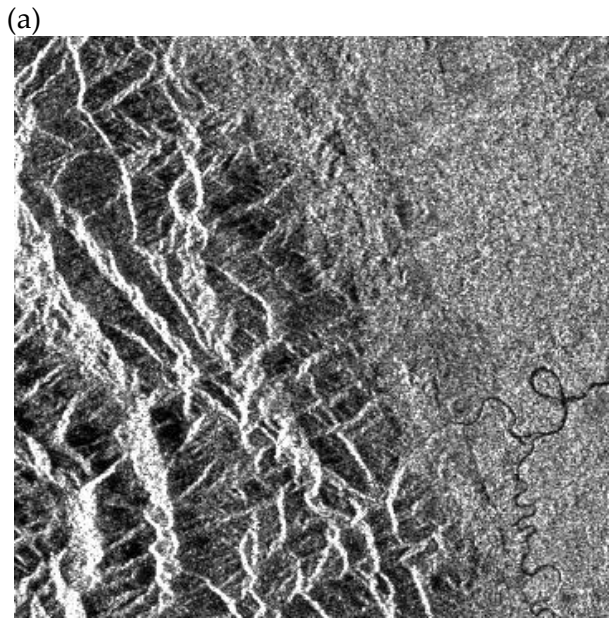


Figure 6-3: Sentinel-1 pre-processing: (a) ingested image, (b) converted to gamma naught and speckle filtering (Modified Frost filter), (c) multi-temporal filtered and orthorectified image

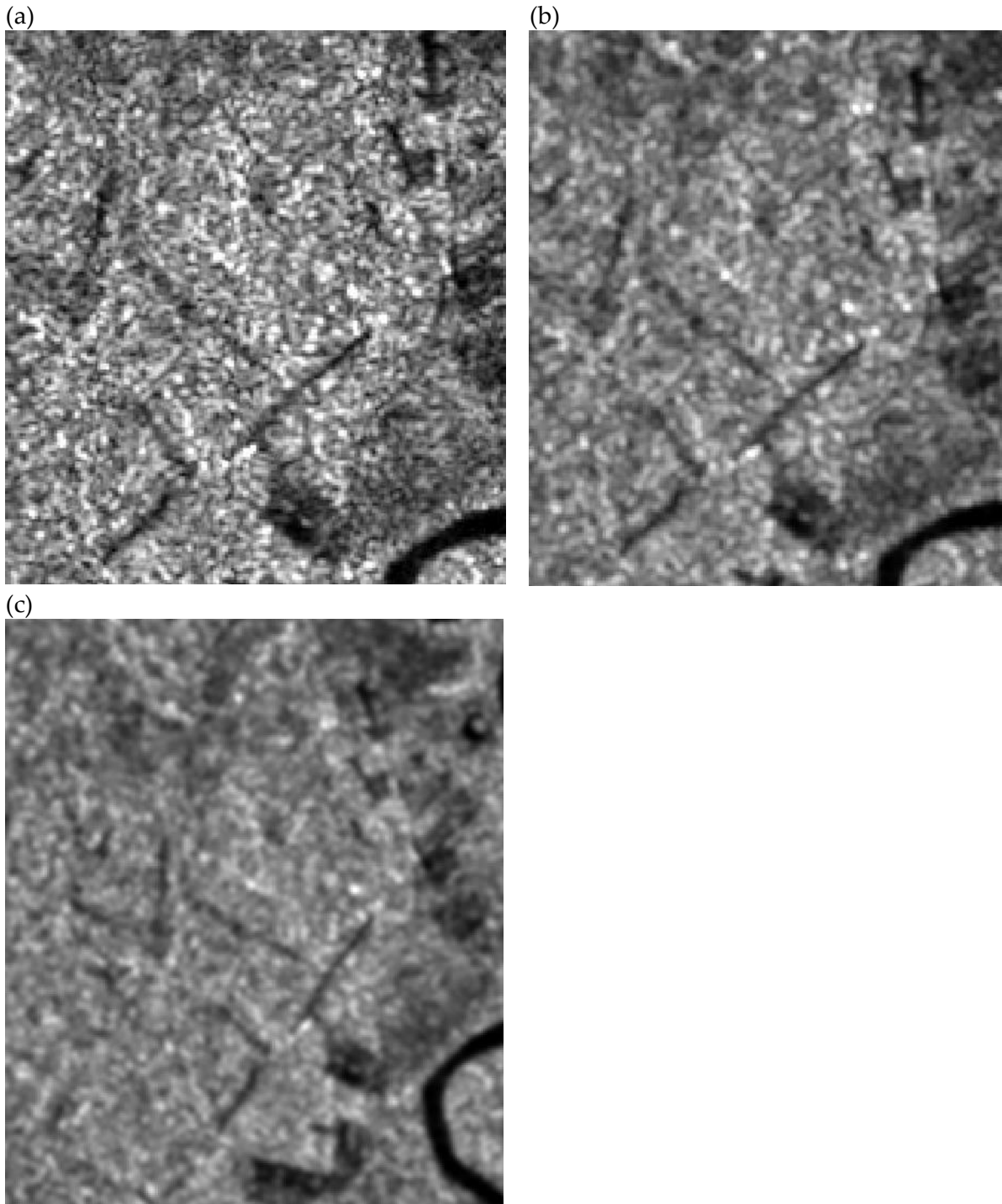


Figure 6-4: S1 (12.03.2016) speckle noise reduction: (a) ingested image (a) image filtered with modified Frost filter, (b) image filtered with the multi-temporal filter and orthorectification

In Figure 6-5 a subset of the S1 backscatter image from 12.03.2016 and the calculated temporal metrics minimum, maximum, mean, median, standard deviation and coefficient of variation are shown. This figure demonstrates the fact that temporal metrics of SAR backscatter values reduce the signals ambiguity and reveal certain surface structures. For example, a visual comparison of the mono-temporal backscatter image (a) with the mean (d)

or median (e) shows that the contrast between the backscatter signals of different land cover types is enhanced in the mean and median (darker versus brighter areas).

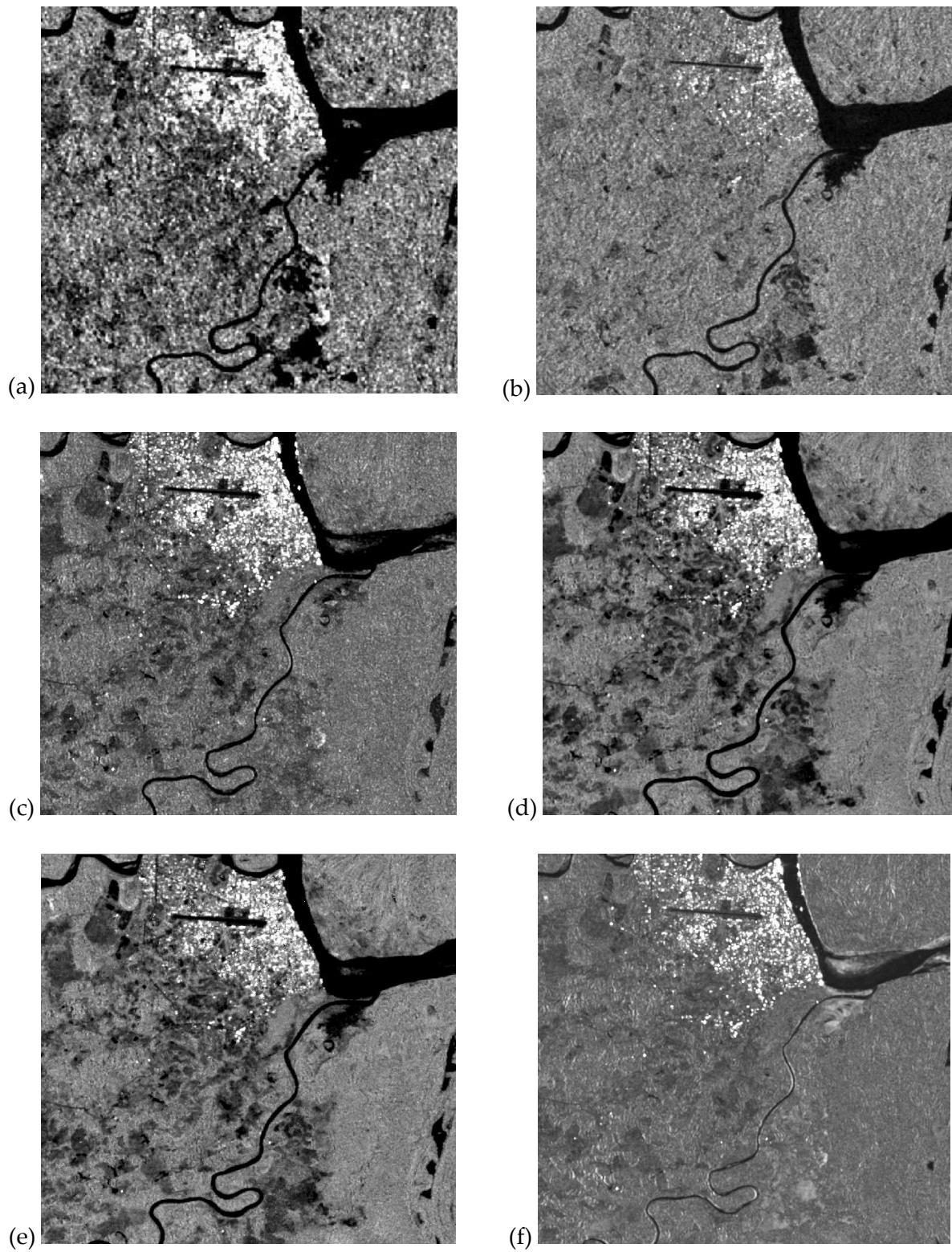


Figure 6-5: S1 (a) mono-temporal backscatter image (12.03.2016) and temporal metrics: (b) minimum, (c) maximum, (d) mean, (e) median, (f) standard deviation

6.1.2 Training Sample Selection and Evaluation

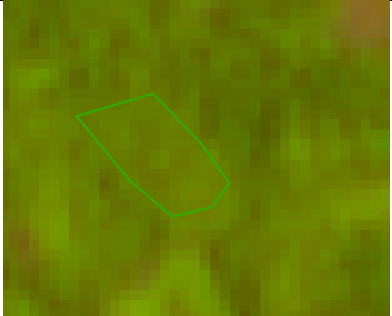
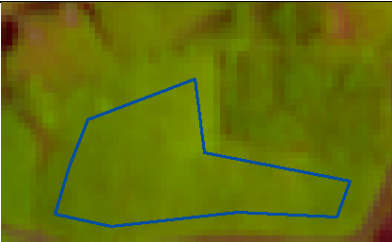
The S2 scene from 10.03.2016 is chosen as reference scene to manually select training samples because it is the scene with the best atmospheric condition. Besides, using a S2 scene as reference image allows to integrate all ten S2 bands in the mono-temporal classification. If a L8 scene would be selected as master scene, only those six corresponding bands which cover the same area of the electromagnetic spectrum (blue, green, red, NIR, SWIR1 and SWIR2, see Figure 4-2) could be used to classify the S2 scenes, omitting the additional red-edge and NIR2 bands.

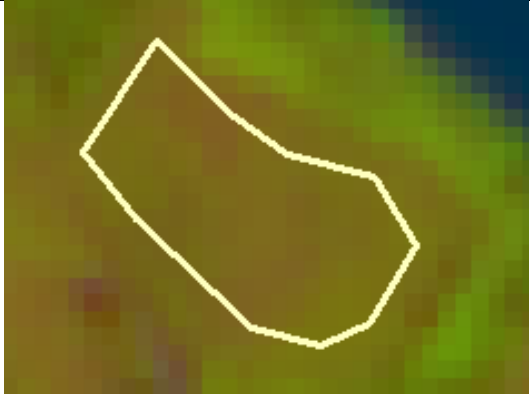
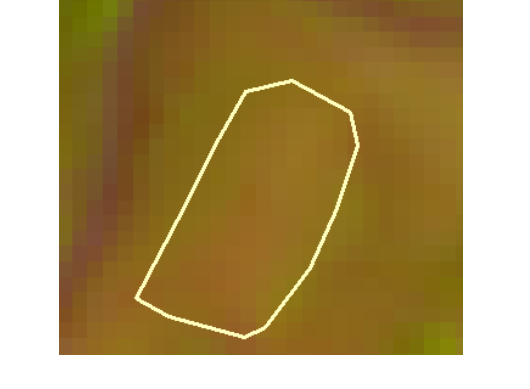
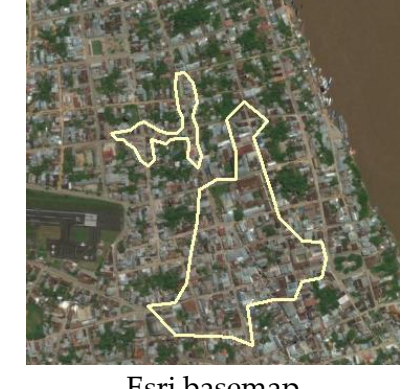
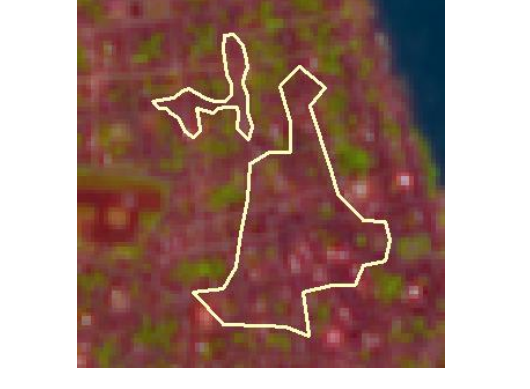
Examples of training data polygons for all IPCC LU classes are depicted in Figure 6-6. It needs to be mentioned that VHR images were not available for the entire test site, thus limiting the search area for the training data selection and impeding a distribution of training samples across the entire scene. Furthermore, the time gap between VHR images and the S2 scene needs to be considered in the selection process and polygons need to be geometrically adjusted as precise as possible to the S2 scene. The example for the class *other land* given in Figure 6-6 shows very well the time dependency of certain land use categories such as bare soil. Whereas the training sample completely represents the class *other land* in the S2 image from 10.03.2016, it represents *other land* as well as *wetlands* in the VHR image which was acquired not even four months later. Considering the time dependency as well as frequent cloud cover, it is obvious that the selection of stable and cloud-free LU classes across a time series of optical images is challenging in humid tropical regions.

Due to visible spectral variances within the LU category, the class *forest* has been divided into two subclasses and the class *cropland* into three subclasses during the selection process (see Table 6-1). This step has been introduced in order to derive detailed and representative spectral signatures. For the final forest status map, the classification result is reclassified by merging all non-forest classes. All in all, 197 training samples are collected (see Table 6-1)

Table 6-1: Classification key and number of training samples per LU class

Class ID	Class name	Subclass ID	Subclass name	Number of samples
10	Forest	11	Forest1	33
		12	Forest2	15
20	Cropland	21	Plantation	39
		22	Cropland1	22
		23	Cropland2	11
30	Grassland			27
40	Wetlands			21
50	Settlements			13
60	Other land			16
				Σ 197

Class	VHR Image	S2 Image (10.03.2016)
Forest1	 <p data-bbox="422 604 790 678">Esri basemap (World View 02, 20.06.2015)</p>	
Forest2	 <p data-bbox="491 996 722 1032">Spot 6, 07.09.2015</p>	
Plantation	 <p data-bbox="422 1182 790 1256">Esri basemap (World View 02, 20.06.2015)</p>	
	 <p data-bbox="422 1500 790 1576">Esri basemap (World View 02, 20.06.2015)</p>	
Cropland 1	 <p data-bbox="422 1877 790 1948">Esri basemap (World View 02, 20.06.2015)</p>	

<p>Cropland 2</p>		
	<p>Spot 6, 07.09.2015</p>	
<p>Grassland</p>		
	<p>Esri basemap (World View 02, 20.06.2015)</p>	
<p>Wetlands</p>		
	<p>Esri basemap (World View 02, 05.05.2011)</p>	
<p>Settlements</p>		
	<p>Esri basemap (World View 02, 20.06.2015)</p>	

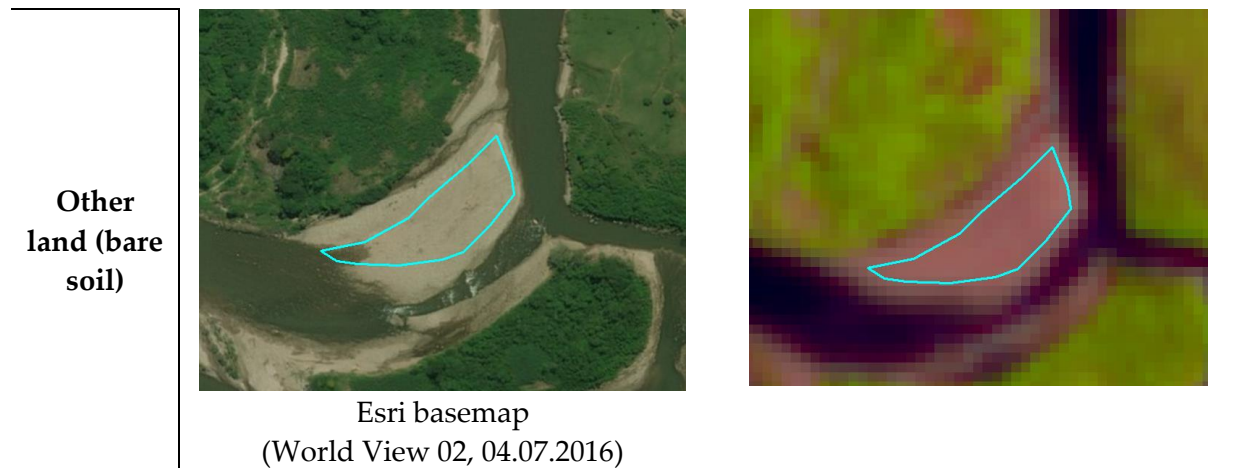


Figure 6-6: Examples of training samples

The separability analysis of the training samples of all LU classes using JMD measure reveals that B12 and B11 are most suitable for discrimination, followed by all three bands that cover the visible region of the electromagnetic spectrum and B5 in the red-edge domain (see Table 6-2). Separability is also analysed for different numbers of bands (three to ten) and band combinations to evaluate, if the elimination of certain bands may improve the classification results. For each number of bands considered, only the best separability result is listed in Table 6-3. The results show that all ten bands provide the greatest information content to discriminate the different LU classes. The separability decreases if more bands are eliminated. However, reducing the number of bands down to 5, leads to only slightly worse separability results compared to using all 10 bands.

For the objectives of this thesis, it is important that the two forest classes can be distinguished from all other non-forest LU classes. Therefore, all further separability and feature space analyses of the training samples are focusing on the two forest classes. According the first and second row of Table 6-4 the two forest classes are spectrally separable from the classes *grassland*, *wetlands*, *settlement* and *other land*, as the maximum JMD corresponds to 1414. The JMD value between *forest2* and *plantation* indicates a spectral similarity between those two classes which is also confirmed by the 2D feature space representations in Figure 6-7. Of the entire 45 feature spaces, only a selection of band combinations is presented here. Figure 6-7 shows an example of feature spaces considering S2 B12 combined with B2, B3, B4, B5, B8a and B11. The ellipses are plotted with a standard deviation of two. All combinations reveal a significant spectral similarity between the classes *forest2* and *plantation*. However, analysis of the spectral separability using JMD (see Table 6-5) shows that the more bands are integrated into the calculation, the better the two classes are spectrally separable.

Based on these analyses, the conclusion can be drawn that no band can be eliminated without the loss of information (see Table 6-3 and Table 6-5). Moreover, it can be assumed that a confusion of *forest2* and *plantation* in the classification results is probable and resulting classification errors in the forest status map have to be expected.

Table 6-2: Separability JMD S2 10.03.2016

S-2 Band	Spectral Region	Average
B2	Blue	1156
B3	Green	1144
B4	Red	1163
B5	Red-edge	1144
B6	Red-edge	927
B7	Red-edge	971
B8	NIR	950
B8a	Red-edge	1006
B11	SWIR	1170
B12	SWIR	1221

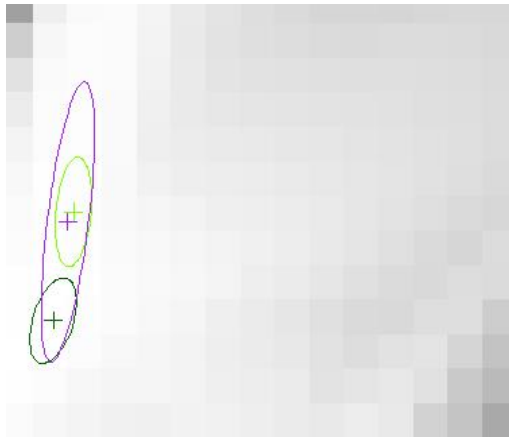
Table 6-3: Separability analysis using different band combinations

S-2 Band combinations	Average Separability
All bands	1410
B3, B4, B5, B6, B7, B8, B8a B11, B12	1409
B3, B4, B5, B6, B7, B8, B11, B12	1409
B3, B4, B5, B6, B7, B11, B12	1408
B4, B5, B6, B7, B11, B12	1407
B5, B6, B7, B11, B12	1405
B5, B6, B11, B12	1397
B5, B11, B12	1384

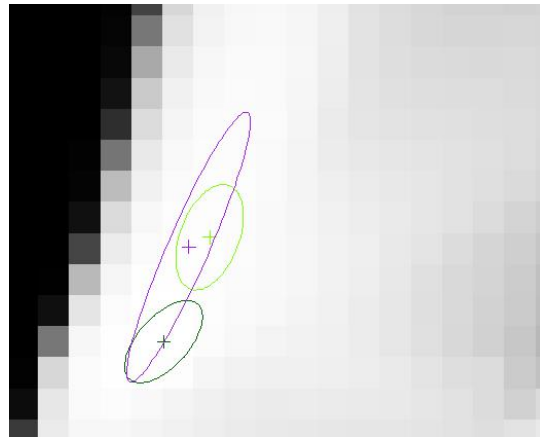
Table 6-4: Separability measure with all bands

Class or Subclass ID	11	12	21	22	23	30	40	50	60
11	0	1377	1408	1413	1414	1414	1414	1414	1414
12	1377	0	1317	1412	1414	1412	1414	1414	1414
21	1408	1317	0	1414	1414	1412	1414	1414	1414
22	1413	1412	1414	0	1414	1401	1414	1413	1414
23	1414	1414	1414	1414	0	1411	1414	1414	1414
30	1414	1412	1412	1401	1411	0	1414	1414	1414
40	1414	1414	1414	1414	1414	1414	0	1414	1414
50	1414	1414	1414	1413	1414	1414	1414	0	1414
60	1414	1414	1414	1414	1414	1414	1414	1414	0

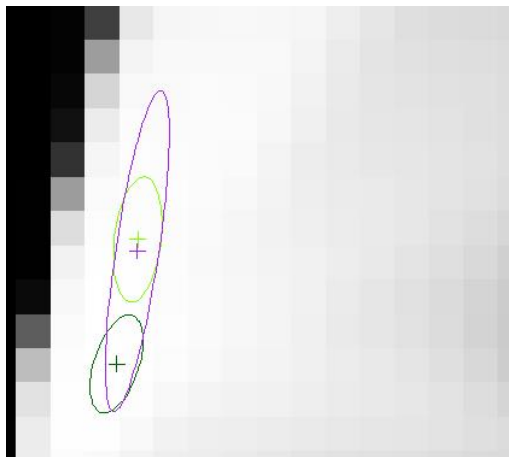
-  Forest1
-  Forest2
-  Plantation
-  Mean



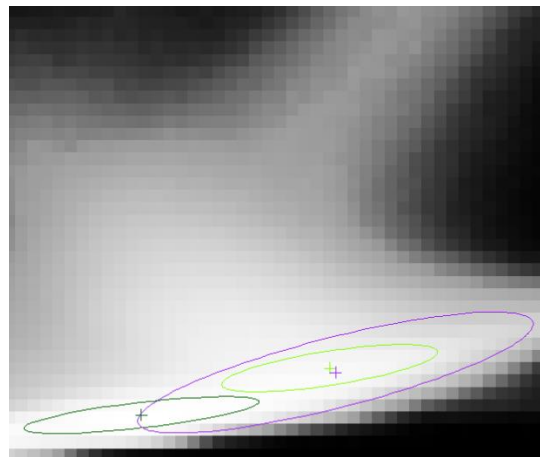
(a) Feature space: x-axis B2, y-axis B12



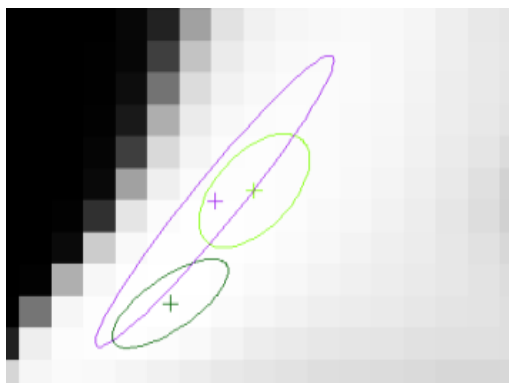
(b) Feature space: x-axis B3, y-axis B12



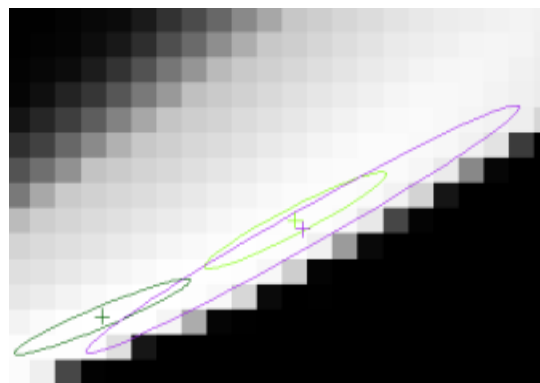
(c) Feature space: x-axis B4, y-axis B12



(d) Feature space: x-axis B5, y-axis B12



(e) Feature space: x-axis B8a, y-axis B12



(f) Feature space: x-axis B11, y-axis B12

Figure 6-7: Feature spaces with land use data considering B12 combined with B2, B3, B4, B5, B8a, B11

Table 6-5: Separability analysis of the classes forest2 and plantation using different band combinations

S-2 band combinations	Separability
All bands	1317
B3, B4, B5, B6, B7, B8, B8a B11, B12	1314
B3, B4, B5, B6, B7, B8, B11, B12	1306
B3, B4, B5, B6, B7, B11, B12	1295
B3, B4, B6, B7, B11, B12	1277
B5, B6, B7, B11, B12	1256
B5, B6, B11, B12	1233
B6, B7, B11	1175
B5, B9	1012
B5	635

6.1.3 Forest Mapping Results

6.1.3.1 Optical Time Series Approach

The used image time series consists of 23 images between April 2013 and March 2016. For the reduced time series, only observations between March 2015 and March 2016 are considered (13 images). However, it needs to be mentioned that within all approaches that consider the reduced time series, no classification result can be obtained for 8.54km² (ca. 0.14%) of the study area, as they are covered by clouds in all 13 images.

Result-based approach

The first step of the result-based approach is to assess the radiometric consistency between the images of the time series through applying the ML classification model of the S2 reference scene to other used scenes. Figure 6-8 shows the mono-temporal classification results of the S2 from 22.10.2015 with (a) the original surface reflectance values and (b) after relative radiometric adjustment to the S2 reference scene. Comparing both forest classifications, it can be seen that the forest mask produced with the relative radiometric adjusted images has fewer gaps. Hence, by using the relative radiometric adjusted image a more accurate and homogenous forest classification is achieved.

However, the necessity of relative radiometric becomes even clearer by the classification results obtained with L8. Although a major part of the image shown in Figure 6-9 (a) is affected by cloud and haze, at least for the area south of the plantation a reliable forest/non-forest classification result can be expected. However, the original surface reflectance image produces a classification result where nearly the whole scene is assigned to the class *non-forest* (see Figure 6-9 (b)), while with the radiometrically adjusted image the expected result is achieved (see Figure 6-9 (c)). Thus, the decision is made to perform mono-temporal ML and RF classification with the radiometrically calibrated images.

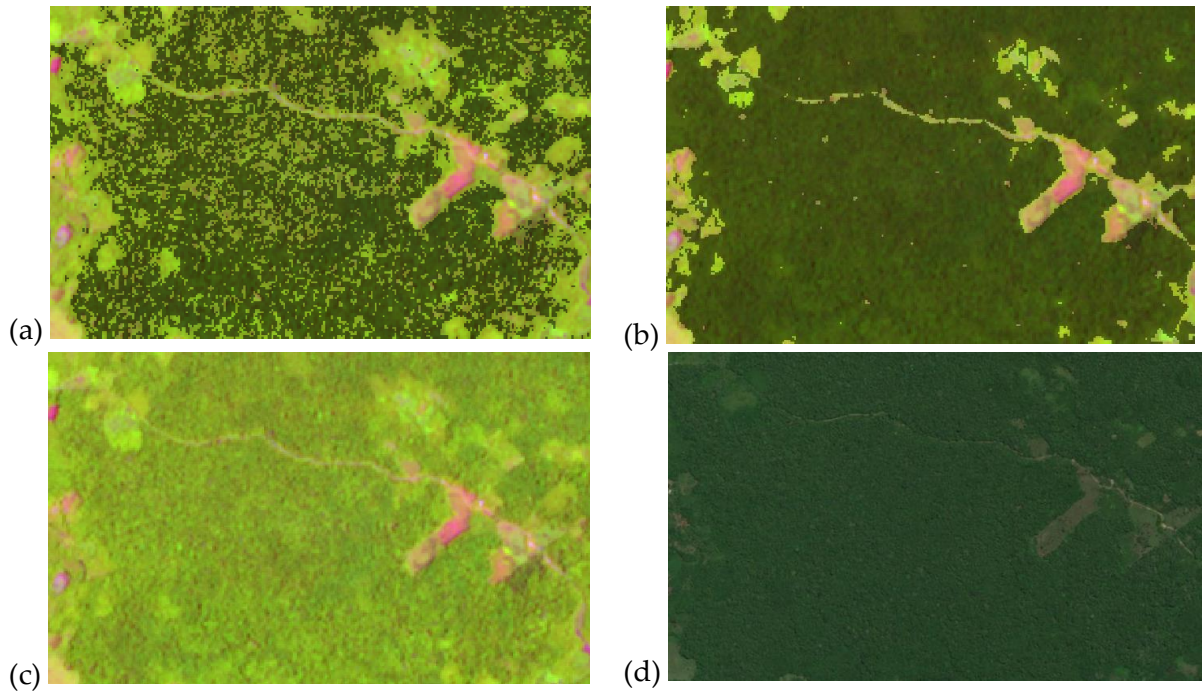


Figure 6-8: Example forest/non-forest map for a subset of the study are: (a) input not radiometrically calibrated, (b) input relative calibrated, (c) S2 image from 22.10.2015 (R: SWIR1, G: NIR, B: red), (d) Esri basemap (World View 02, 20.06.2015)

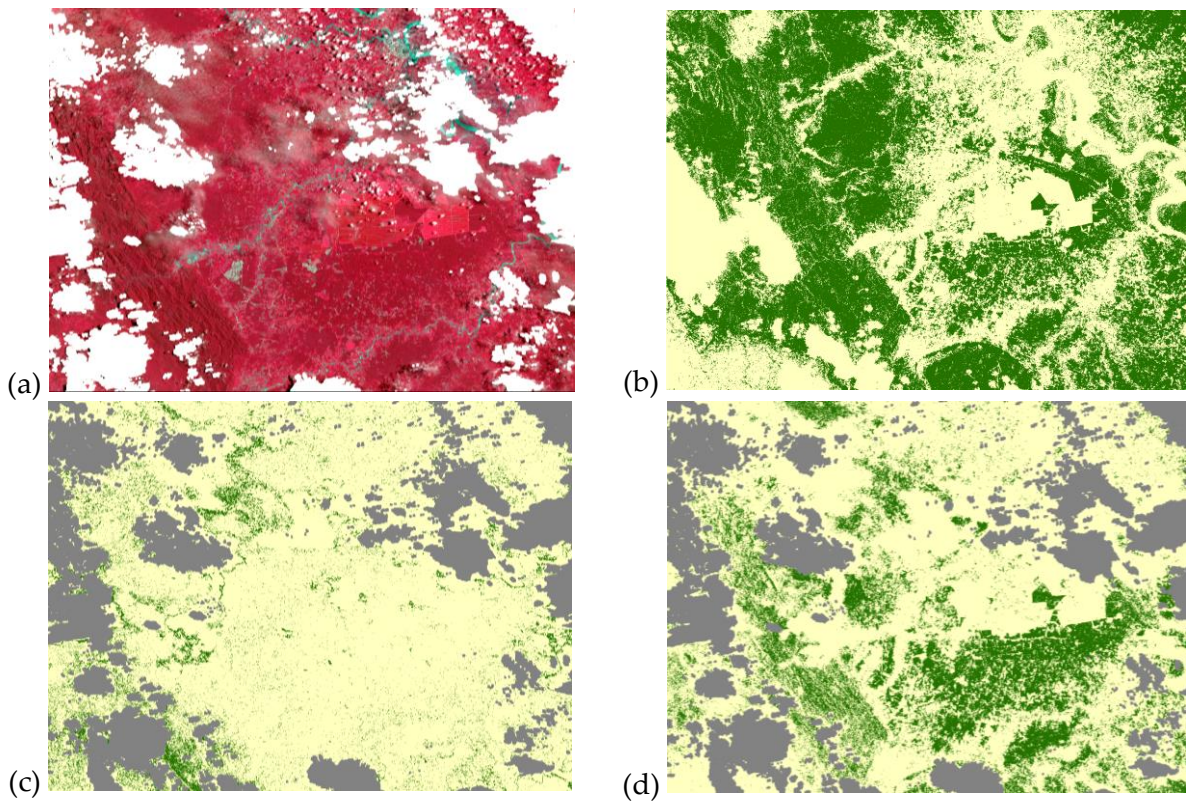


Figure 6-9: Forest/non-forest map of the L8 scene from 25.03.2015: (a) L8 image (R: NIR, G: red, B: green), (b) forest/non-forest map of S2 10.03.2016, (c) input not calibrated, (d) input calibrated

Table 6-6 lists the overall accuracies of all classification results generated within the result-based approach. Considering only ML classifications, results confirm the previous assumption in chapter 5.3.1.1 that the length of the time series may have a negative effect on classification accuracy. Using all available images between April 2013 and March 2016 leads to a worse OA than mono-temporal classification. However, multi-temporal classification with the reduced time series from March 2015 to March 2016 increases OA by about 6% at maximum compared to mono-temporal classification. Regarding the three approaches that employ the reduced time series, the results show an increase of the OA with the application of the weighting functions from 88.27% when no weighting function is applied to 90.42% when the time series is split into three periods. Table 6-6 also provides the 95% confidence intervals of the accuracy measures. The 95% confidence interval provides the range of values within which the actual accuracy lies with a probability of 95% (Foody, 2009). Therefore, if the 95% confidence interval of the three OAs achieved with the reduced time series is considered, it is possible that the actual accuracies are very similar.

On the contrary, RF classification accuracy measures reveal a completely different pattern. The worst OA is obtained within the mono-temporal classification (86.79%) and the highest OA (90.50%) when using the reduced time series from March 2015 to March 2016 without weighting. The application of weighting functions does not give any added value to classification accuracies as OA decreases by about 1% when the time series is split into two periods and by about 3% when the time series is split into three periods. However, also for RF classification results apply that, if the 95% confidence interval is considered, actual OAs might be very similar.

Regarding UAs and PAs, ML always provides higher forest UAs and non-forest PAs whereas RF always provides higher non-forest UAs and forest PAs. A closer look reveals that within all RF classification results non-forest PA never exceeds 72.37% which leads to the conclusion that within the tested workflow the RF classifier tends to overestimate the forest area. However, both classifiers show a significant uncertainty of non-forest UAs and PAs compared to Forest UAs and PAs as the 95% confidence interval nearly always exceeds 5 %.

Considering the results presented in Table 6-6, it can be concluded that using a multi-temporal classification approach integrating the time series within a post-classification analysis does produce a more accurate forest status map compared to the mono-temporal classification result. The fact that highest OAs are obtained with the reduced time series, confirms the assumption made in chapter 5.3.1.1 that the expansion of the data acquisition period has a negative impact on classification accuracies due to possible land use changes. Thus, only observations between March 2015 to March 2016 are considered within the following optical data-based, SAR and combined approaches. Regarding the comparison of ML and RF classifier, no explicit conclusion can be drawn which classifier performs better as almost identical OAs are achieved. However, from the perspective of implementation and computation time, the RF classifier can be recommended as the need to implement a weighting function is omitted.

Table 6-6: Accuracy measures and their 95% confidence interval of the optical result-based approach using ML and RF classifier

Classifier	Input data	NoI*	OA [%]	UA Forest [%]	UA Non-forest [%]	PA Forest [%]	PA Non-forest [%]
ML	Mono-temporal (10.03.2016)	1	84.87 (±2.61)	92.55 (±2.53)	69.57 (±5.96)	85.83 (±2.40)	82.41 (±5.09)
	Multi-temporal (04/2013-03/2016)	23	82.76 (±2.46)	98.83 (±1.14)	61.72 (±5.48)	77.18 (±2.52)	97.58 (±2.32)
	Multi-temporal (03/2015-03/2016)	13	88.27 (±2.32)	94.95 (±2.11)	74.24 (±5.68)	88.57 (±2.24)	87.49 (±4.65)
	Multi-temporal (03/2015-03/2016) weighted 2 periods	6/7	89.62 (±2.28)	93.03 (±2.37)	80.00 (±5.56)	92.90 (±1.84)	80.32 (±5.48)
	Multi-temporal (03/2015-03/2016) weighted 3 periods	4/4/5	90.42 (±2.23)	92.37 (±2.43)	83.87 (±5.30)	95.05 (±1.55)	76.65 (±5.81)
RF	Mono-temporal (10.03.2016)	1	86.79 (±2.65)	89.32 (±2.89)	78.44 (±6.26)	93.18 (±1.85)	69.01 (±6.01)
	Multi-temporal (04/2013-03/2016)	23	87.80 (±2.50)	89.45 (±2.77)	81.89 (±5.76)	94.6 (±1.63)	68.74 (±5.81)
	Multi-temporal (03/2015-03/2016)	13	90.50 (±2.27)	91.00 (±2.5)	88.62 (±4.83)	96.78 (±1.32)	72.37 (±5.79)
	Multi-temporal (03/2015-03/2016) weighted 2 periods	6/7	89.38 (±2.41)	89.09 (±2.75)	90.73 (±4.64)	97.86 (±1.05)	63.64 (±5.92)
	Multi-temporal (03/2015-03/2016) weighted 3 periods	4/4/5	87.64 (±2.53)	88.06 (±2.86)	87.42 (±5.31)	96.83 (±1.29)	62.62 (±5.74)

*NoI = Number of images

Data-based approach

Within the data-based approach, a multi-temporal surface reflectance image stack and an image stack consisting of the temporal median of each spectral band are used as input data sets for forest mapping. A visual inspection of the temporal median (as an example, the median of the red band is shown in Figure 6-10) confirms the fact that the median is robust against outliers as the image seems to be unaffected by clouds. Regarding the calculation of the temporal median, it needs to be mentioned that larger no-data areas due to clouds remain for the four bands that are only provided by S2 (three red-edge bands and the second

NIR band), because only four S2 images are available to calculate the median. Due to the deficiencies in no-data handling discussed in chapter 5.3.1.2, using the median of the three S2 red-edge bands and the additional NIR band for ML classification increases the unclassified area to about 185.579km² (ca. 3%) of the total mapped area. Moreover, a visual analysis of the temporal median of each spectral band reveals a radiometric error in the median of the blue band with a characteristic rectangular pattern over the mountainous region of the study area (see Figure 6-11). To investigate the reason for this error, the blue band of all L8 and S2 surface reflectance products is visually examined. It turns out that the blue band of nearly all L8 surface reflectance products shows a radiometric error with the same characteristic pattern. To test the impact of this error on results, ML and RF classification are performed twice. One time the median of the blue band is integrated in the input data stack and a second time the band is omitted.



Figure 6-10: Temporal median of the red band (red: no-data areas)

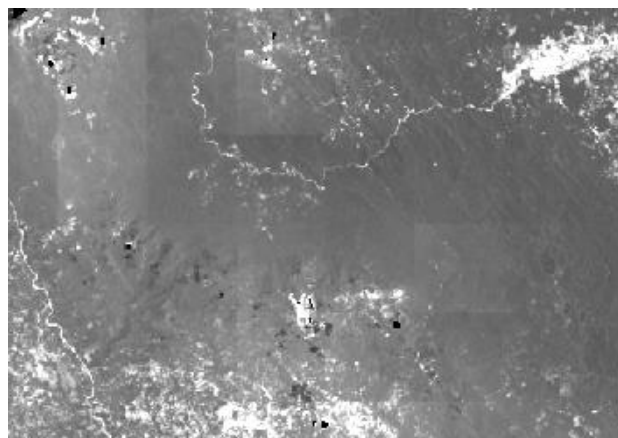


Figure 6-11: Temporal median of the blue band of a subset of the study area (black areas: no-data)

In Table 6-7 the OAs obtained with both classifiers within the data-based approach are listed. ML classification can only be conducted with the median image as the ML classifier cannot handle no-data values properly within calculation of the classification model if no-data values occur within training areas (see chapter 5.3.1.2). The highest OA (90.23%) is achieved with the RF classifier and the stack of median bands (without the blue median). The result is more than 6% higher compared to the RF classification result obtained with the multi-temporal BOA reflectance image stack. However, the combined stack of BOA reflectance values and the temporal median achieves a similar result compared to the multi-temporal BOA reflectance stack. One possible reason can be found in the generation process of the decision trees of the RF classifier. As described in chapter 2.3.2, at each node a random sample of all available predictor variables is selected to define the splitting criterion. The combined BOA reflectance and temporal median image stack consists of 112 bands, including 103 BOA reflectance and 9 median bands. Hence, the probability that a BOA reflectance band is selected within the generation process is higher than the probability to select a median band. Consequently, BOA reflectance bands have more influence on the calculation of the RF classification model than the median bands.

The investigation of the effects of integration or exclusion of the blue band temporal median reveals significant differences for both classifiers. Eliminating the blue median within ML classification increases the OA by more than 7%, from 80.26% to 87.90%. In contrast, integrating the defective blue band within the RF classification does not affect classification accuracies as significantly (88.56% versus 90.23%). Considering the 95% confidence interval, it might be possible that the blue median does not affect mapping accuracy at all. A possible explanation for this lies in the fact that the split criterion in each node corresponds to the best split among a random sample of predictor variables. Even if the blue median is selected, another predictor variable might provide a better split criterion. Thus, the influence of the blue temporal median on the classification result is reduced through the modality of the generation of the RF classifier.

UAs and PAs of both classifiers show the same pattern as within the result-based approach. Comparing both results obtained with the median stack, while forest UA and non-forest PA are higher for the ML results, non-forest UA and forest PA are higher for the RF results. The 95% confidence interval for non-forest UAs and PAs indicate a higher uncertainty in the classification of non-forest areas compared the class forest.

Comparing the mono-temporal RF classification result listed in Table 6-6 and the RF classification result obtained with the multi-temporal BOA reflectance image stack, the mono-temporal classification result achieves an OA about 3% higher (86.79% versus 83.73%). The main reason for this might be the fact that the training samples are adapted to the S2 scene of 10.03.2016 and are not screened for missing values and their temporal stability between March 2015 and March 2016. Besides, no-data values in the image stack are likely to cause classification errors. However, when using the temporal median to perform RF classification, OA increases by 2% and 3% (without the median of the blue band) respectively, compared to the mono-temporal result. The same pattern is also observed when comparing the mono-temporal ML classification result with the median result (without the blue band) (84.59 versus 87.26%). Therefore, the previous conclusion drawn from the results of the optical result-based approach, that time series data comprise comprehensive information to map the forest status more accurately in humid tropical regions, is confirmed.

Comparison of the best OAs achieved within the data-based approach and the result-based approach shows that both approaches can achieve similar results as the OAs do not even differ by 1% (90.23% data-based and 90.50% result-based). Regarding UAs and PAs, the result-based approach produces higher UA for non-forest and higher PA for forest, whereas UA for forest and PA for non-forest are higher for the data-based approach.

Since the RF classifier achieves higher OAs compared to the ML classifier, the RF classifier is considered to outperform the ML classifier and will therefore be used within all following approaches.

Table 6-7: Accuracy measures and their 95% confidence interval of the optical data-based approach using ML and RF classifier

Classifier	Input data	NoB*	OA [%]	UA Forest [%]	UA Non-forest [%]	PA Forest [%]	PA Non-forest [%]
ML	Temporal median (03/2015-03/2016)	10	80.26 (±2.71)	94.32 (±2.36)	61.82 (±2.36)	78.61 (±2.56)	87.98 (±4.45)
	Temporal median (03/2015-03/2016) without blue	9	87.90 (±2.38)	94.80 (±2.17)	73.68 (±5.73)	88.12 (±2.29)	87.32 (±4.71)
RF	BOA reflectance (03/2015-03/2016)	103	83.73 (±2.62)	96.05 (±1.96)	66.17 (±5.70)	80.18 (±2.69)	92.17 (±3.66)
	Temporal median (03/2015-03/2016)	10	88.56 (±2.27)	93.23 (±2.34)	79.31 (±5.59)	92.65 (±1.84)	80.72 (±4.49)
	Temporal median (03/2015-03/2015) without blue	9	90.23 (±2.22)	93.11 (±2.34)	81.63 (±5.43)	93.81 (±1.72)	79.86 (±5.57)
	BOA reflectance & temporal median (03/2015-03/2016)	112	83.56 (±2.65)	95.81 (±2.01)	66.29 (±5.71)	80.04 (±2.72)	91.82 (±3.68)

*NoB = Number of Bands

6.1.3.2 SAR Time Series Approach

Table 6-8 provides the accuracy measures of the three forest status maps (mono-temporal, image stack and temporal metrics) derived from SAR data. The multi-temporal backscatter image stack produces the best classification result. As the visual examination of the mono-temporal S1 scene shows an ambiguity in the backscatter signal, whereas temporal metrics reveal different surface structures, significant lower accuracies for the mono-temporal classification might be expected. However, comparing the OAs, the stack of temporal metrics achieves a slightly worse result than the mono-temporal image (about 0.5%), leading to the

conclusion, that temporal metrics do not comprise any added value to improve forest mapping. But, a closer look at forest and non-forest PAs relativizes this statement. The low UA and high PA for forest (64.16 and 97.89% respectively) as well as the extreme low PA for non-forest (7.86%) of the mono-temporal classification result indicate that the class forest is overrepresented, whereas non-forest is underrepresented. Using the temporal statistics as input variables for RF classification decreases the forest PA by about 11% to 86.95% but increases the PA for non-forest by more than 17% to 24.54%. This value is still extremely low but shows that the temporal metrics provide better information to discriminate forest from non-forest, as also the PA obtained with the multi-temporal backscatter image stack is about 7% lower. Figure 6-12 (c) shows the forest cover status map produced with S1 temporal metrics for a subset of the study area. It clearly reveals the reason for the low PA of non-forest. Whereas in the optical S2 image (a) it is easy to discriminate different land cover types visually, they all show a similar signal pattern in the SAR image (b).

Comparing the OAs obtained with one single S1 scene and the multi-temporal backscatter stack shows that the utilization of an image time series slightly improves classification accuracies. Generally, from the obtained results within the SAR-based mapping approach it can be concluded that neither the utilization of mono-temporal nor multi-temporal backscatter data or temporal metrics derived from the backscatter time series produce a forest status map with an acceptable accuracy. This result is in line with results from previous studies that either use mono-temporal or multi-temporal SAR data for tropical LCLU and or forest mapping (Clerici et al., 2017; Hirschmugl et al., 2018; Vaglio Laurin et al., 2013). The main reason for this lies in the similarity of received backscatter C-band signal from forest areas and other vegetated areas. However, the achieved accuracies for the three maps indicate an added value of time series data for forest mapping with SAR data as the multi-temporal backscatter image stack produces the highest OA..

Table 6-8: Accuracy measures and their 95% confidence interval of the SAR data-based approach using RF classifier

RF	NoB	OA [%]	UA Forest [%]	UA Non-forest [%]	PA Forest [%]	PA Non-forest [%]
Mono-temporal (12.03.2016)	1	64.16 (±3.71)	63.90 (±3.80)	70.00 (±16.68)	97.98 (±1.09)	7.86 (±0.97)
backscatter (3/2015-3/2016)	30	66.47 (±3.66)	66.32 (±3.88)	68.00 (±10.63)	95.23 (±1.53)	17.33 (±2.06)
Temporal metrics (3/2015-3/2016)	6	63.68 (±3.70)	65.96 (±4.08)	52.80 (±8.79)	86.95 (±2.25)	24.54 (±3.12)

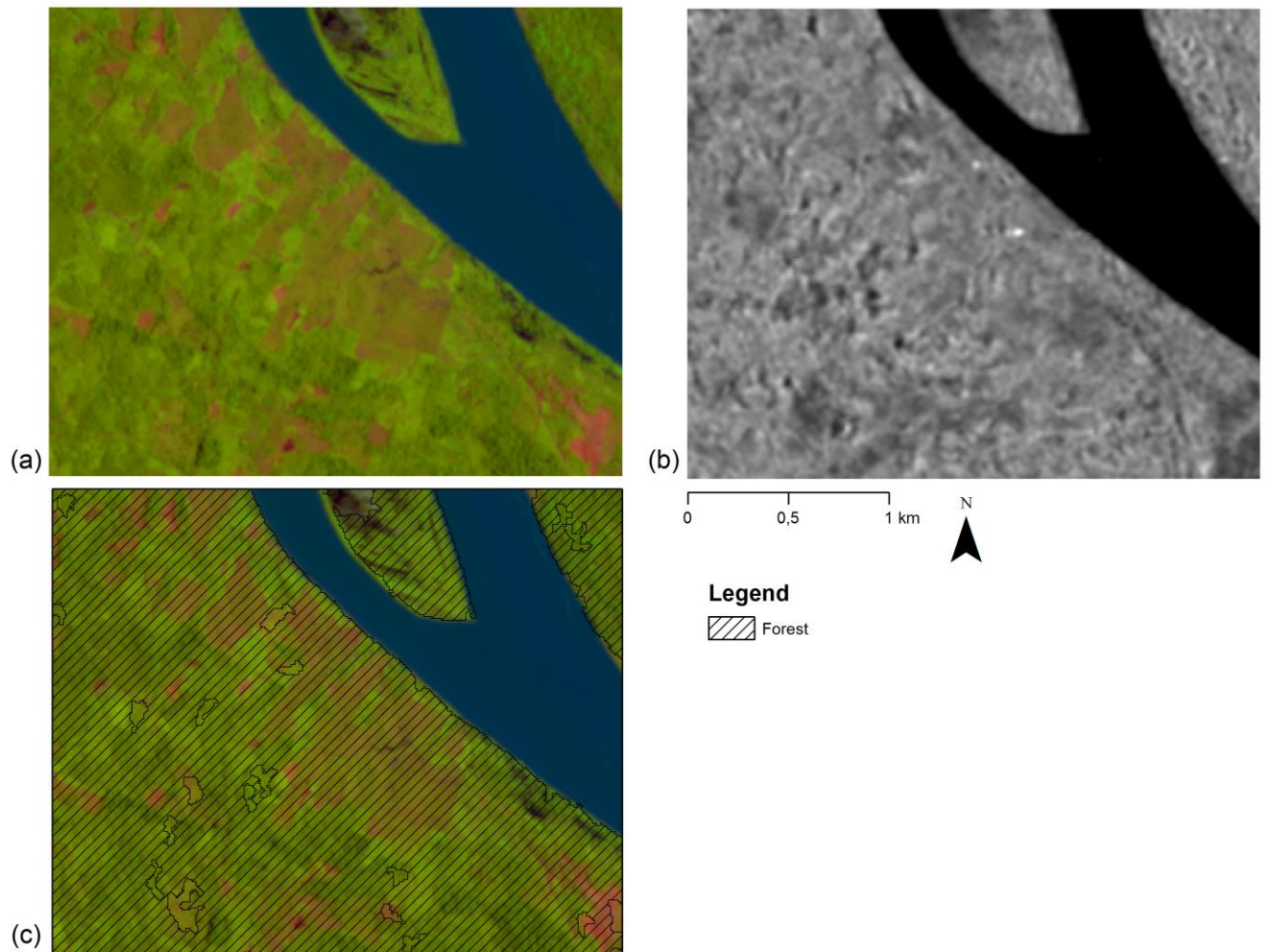


Figure 6-12: Subset of forest status map produced with S1 temporal statistics: (a) S2 10.03.2016 (R: SWIR1, G: NIR, B: red), (b) S1 temporal mean 03/2015-03/2016, (c) forest status map

6.1.3.3 Combined Optical-SAR Approaches

Table 6-9: Overview of the tested combined optical-SAR approaches

	Approach	Used data	Classification Method
Test 1	Data-based approach	Combined optical-SAR image stack	Random Forest classification
Test 2	Result-based approach	Forest probability and reliability maps produced with optical and SAR time series data separately	Bayesian combination

Table 6-9: Overview of the tested combined optical-SAR approaches provides a brief summary of the tested data-based and result-based approaches using combined optical-SAR time series data. Concerning the combined data-based approach, based on the results achieved within optical and SAR time series approaches, the input data stack to calculate the

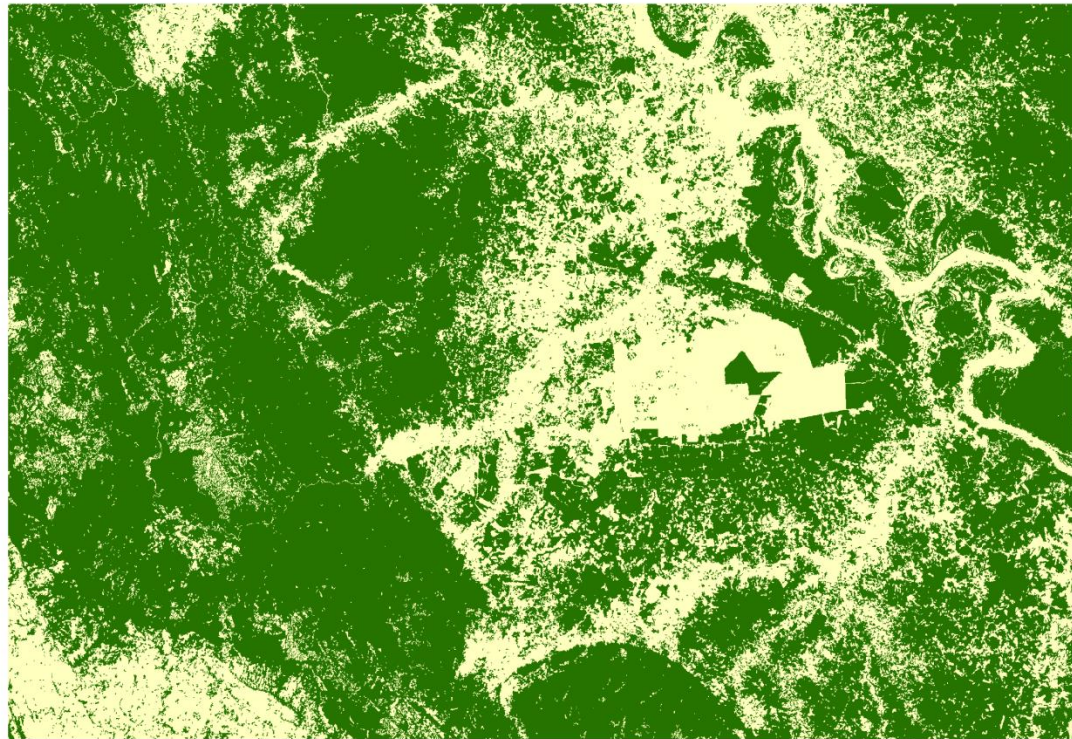
RF classification model is composed of the optical temporal median (the blue median is omitted) and the multi-temporal SAR backscatter stack. Input maps to perform the Bayesian combination approach are the forest status map derived within the optical result-based approach, as this one achieved the highest OA within all optical approaches, and the SAR classification result produced with the multi-temporal backscatter image stack. As the Bayesian combination approach is based on forest probability maps, the calculated forest proportion on valid pixels serves as auxiliary optical forest probability. As the OTB facilitates the generation of classification confidence maps, the SAR forest probability map is derived within the RF classification procedure. The OAs of the forest status maps obtained with these datasets separately serve as reliability measure for the optical and SAR probability maps respectively. However, it should be mentioned that the reliability of the forest probability might vary for different pixels. For example, SAR pixels that are affected by geometry effects cannot be mapped with the same reliability as pixels that are not influenced by those effects. Regarding the optical reliability map, those areas that could not be mapped due to clouds are assigned a reliability of zero, in order to eliminate optical probability in equation (2). This ensures that only SAR forest probability and reliability define the result.

Table 6-10 shows a significant difference between the performances of the two applied approaches. While the data-based approach achieves an OA of 91.97%, the OA obtained with the Bayesian combination approach is about 10% lower. Furthermore, the Bayesian combination approach achieves a significant high forest PA and low non-forest PA. This might be explained by the fact that, according to the results obtained with the SAR approach, the initial SAR probability map comprises a high forest PA and a low non-forest PA (see Table 6-8).

The comparison of the RF OAs of the data-based approaches obtained with the optical temporal median only as well as in combination with the SAR multi-temporal backscatter stack shows that the additional use of SAR data slightly improves classification accuracies (about 1.74%). If the 95% confidence interval is considered, it must be concluded that actual classification accuracies might be identical. Nevertheless, it needs to be mentioned that the forest status map with the highest OA produced within the optical-based approaches possesses data gaps due to clouds, whereas the utilization of SAR data ensures that a classification result is obtained for all pixels. Thus, the combined optical-SAR data-based approach is considered to produce the best classification result and will therefore be applied to the Gabonese study area. Figure 6-13 shows the final forest status map of the Peruvian study area.

Table 6-10: Accuracy measures and their 95% confidence interval of the combined data-based and result-based approaches

	OA [%]	UA Forest [%]	UA Non-forest [%]	PA Forest [%]	PA Non-forest [%]
Data-based combination	91.97 (±2.02)	93.52 (±2.41)	88.93 (±3.94)	94.33 (±1.91)	87.45 (±4.11)
Result-based combination	81.77 (±3.03)	80.43 (±3.59)	86.78 (±5.05)	95.77 (±1.56)	54.40 (±4.71)



Legend
■ forest
■ non-forest

0 10 20 km



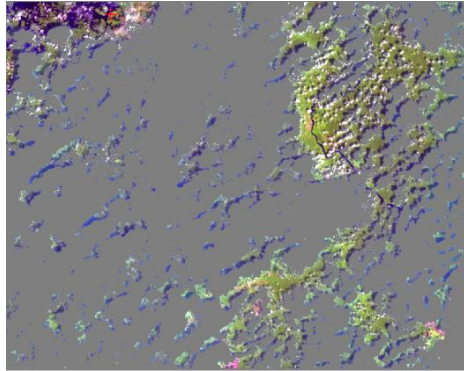
Figure 6-13: Final forest status map of the Peruvian study area

6.2 Gabonese Study Area

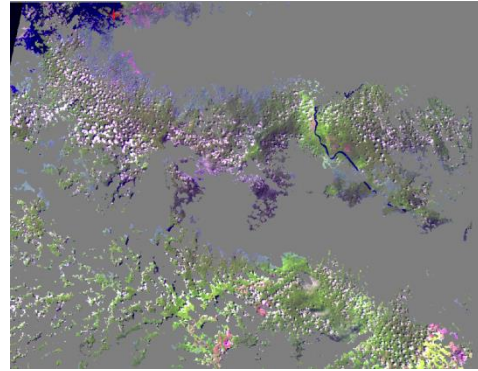
Based on the results obtained for the Peruvian study area, a forest status map of the Gabonese study area is produced using a combined multi-temporal data stack consisting of the optical temporal median of each band and SAR backscatter images as input data set for RF classification. However, to be able to assess and quantify the added value of the combined use of optical and SAR data for Gabon, the data-based approach is also conducted with the optical temporal median only. The utilized optical time series consists of nine L8 and ten S2 images as well as 26 S1 scenes (in VH and VV polarization) acquired between January and December 2016.

6.2.1 Data Pre-processing

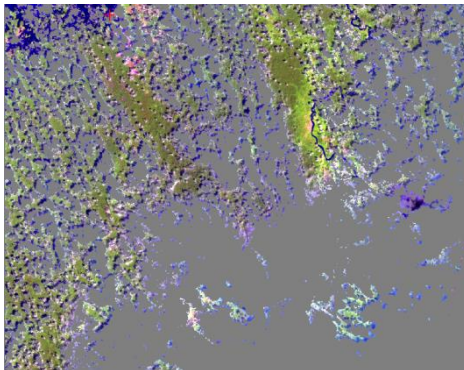
Pre-processing of all L8, S2 and S1 images is performed according to the method described in chapter 5.1. Visual analysis of the optical images reveals the same geometric north-south shift between S2 and L8 images as observed in Peru. The distortion is corrected successfully by the proposed image matching algorithm. Unfortunately, the visual examination of L8 and S2 images also uncovers that image quality for the Gabonese study area is even worse than for Peru, due to extremely high rates of cloud cover and haze throughout the whole year (see Figure 6-14). Consequently, the number of valid observations per pixel available for the calculation of the temporal median is very low across the whole scene. In fact, for 0.01% (5.9471km²) of the whole study area not a single valid observation exists within the entire optical time series and for more than 12% (848.2648km²) less than 4 valid observations is available. Moreover, Figure 6-14 also shows that the L8 and S2 cloud masks lack accuracy, resulting in a great number of remaining cloud and cloud shadow pixels after the application of the cloud-masking workflow. Thus, the probability increases that the temporal median is influenced by outliers. This assumption is confirmed by Figure 6-15. Unlike the temporal median of the red band of the Peruvian study (Figure 6-10) which seems to be unaffected by clouds, the red median for a subset of the Gabonese study area shown in Figure 6-15 contains cloudy pixels. As the blue bands of the acquired L8 images show a radiometric error very similar to the one observed for the Peruvian L8 images, the temporal median of the blue band is omitted.



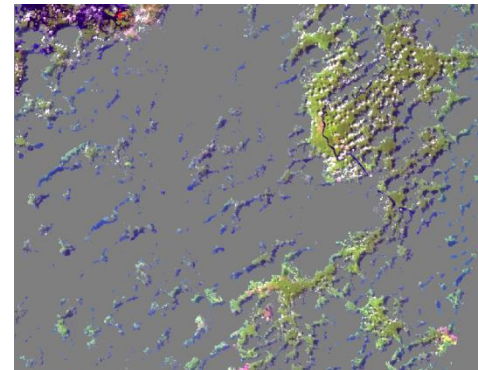
S2 08.01.2016



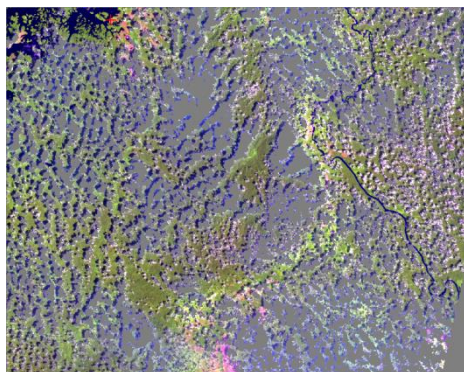
L8 15.01.2016



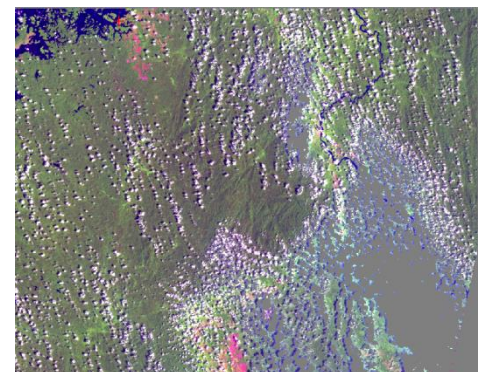
S2 18.01.2016



S2 07.02.2016



L8 16.02.2016



S2 17.02.2016

Figure 6-14: Examples of optical L8 and S2 data available for forest mapping



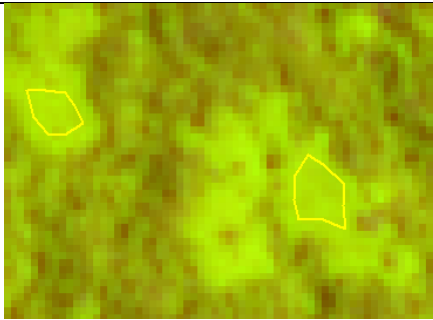
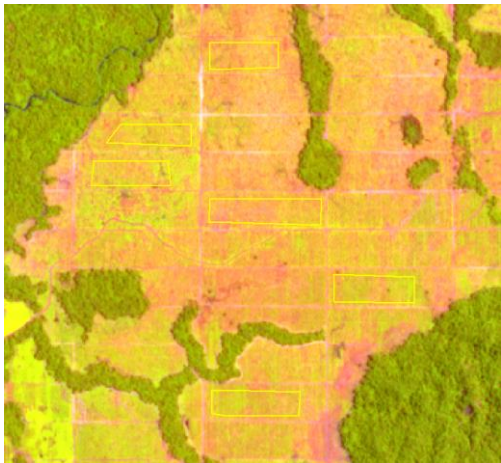
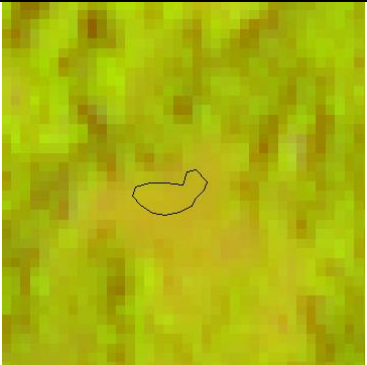
Figure 6-15: Temporal median of the red band (subset of the Gabonese study area)

6.2.2 Training Sample Selection and Evaluation

Due to poor data availability, training sample selection is extremely difficult and cannot be conducted based on one single reference S2 or L8 scene as no image provides the quality to collect enough training samples for all classes. Furthermore, utilizing the median image is not possible either due to bad image quality. Hence, training sample selection is performed using all available S2 and L8 images. Therefore, evaluation of training samples based on JMD and feature space analysis cannot be conducted. Moreover, VHR images are not available for the entire Gabonese study area which additionally restricts the search area. Visible spectral variances lead to the definition of two forest and two cropland classes, in order to derive detailed and representative spectral signatures. All in all, 233 training samples are collected (see Table 6-1). Examples of training data polygons are illustrated in Figure 6-16.

Table 6-11: Classification key and number of training samples per land use class

Class ID	Class name	Subclass ID	Subclass name	Number of samples
10	Forest	11	Forest1	30
		12	Forest2	42
20	Cropland	21	Plantation	29
		22	Cropland1	8
30	Grassland			20
40	Wetlands			32
50	Settlements			19
60	Other land			53
				Σ 233

Class	VHR Image	S2 Image (02.04.2017)
Forest1	 <p data-bbox="485 600 766 636">Rapid Eye 15.02.2015</p>	
Forest2	 <p data-bbox="510 954 740 994">Spot 6 02.04.2017</p>	
Plantation		
Cropland1	 <p data-bbox="510 1886 740 1924">Spot 6 02.04.2017</p>	

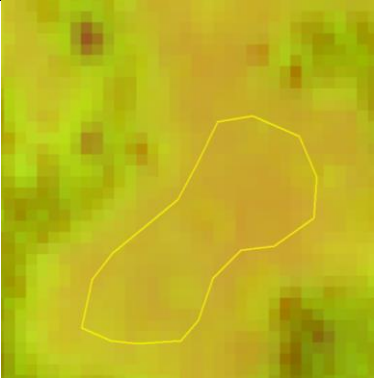
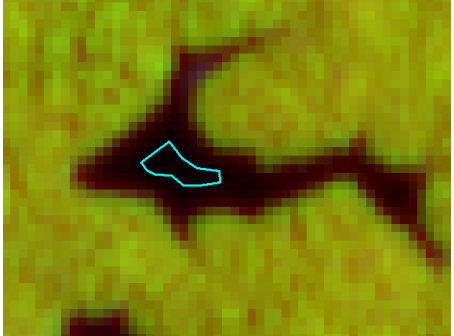
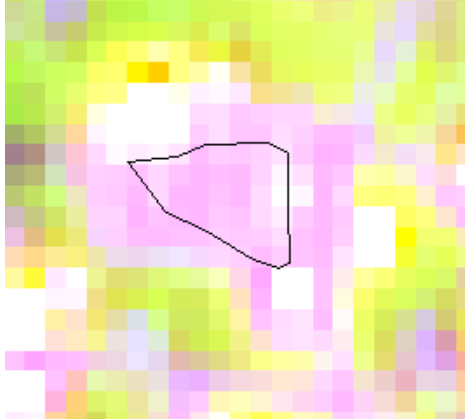
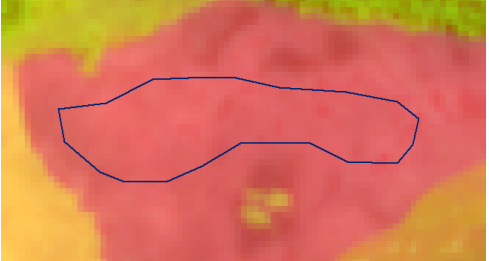
<p>Grassland</p>	 <p>Esri basemap (World View 2 26.03.2011)</p>	
<p>Wetlands</p>	 <p>Rapid Eye 15.02.2015</p>	
<p>Settlements</p>	 <p>Esri basemap (World View 2 07.03.2013)</p>	
<p>Other land</p>	 <p>Esri basemap (World View 2 26.03.2011)</p>	

Figure 6-16: Examples of training samples for each LU class

6.2.3 Forest Mapping Results

Table 6-12 lists the accuracy measures obtained with the two different approaches. The comparison of the optical and combined data-based approaches reveals that the additional integration of a time series of SAR backscatter images increases the OA by about 7%. In contrast to the conclusion drawn from the results for the Peruvian study area, this shows more clearly that the combined use of optical and SAR data improves forest mapping accuracies. A visual analysis of the forest status maps of the entire study area (see Figure 6-17) as well as a small subset (see Figure 6-18) obtained by the two applied approaches reveals that the influence of cloud pixels in the temporal median is reduced significantly in the result of the combined approach. Figure 6-18 does not only confirm the reduction of the influence of cloud pixels, but also shows the advantage of the combined optical-SAR approach that a classification result is obtained for all pixels and no data gaps remain due to clouds.

While the OA, forest and non-forest UAs as well as forest PA increase, non-forest PA shows a considerable decrease for the combined data-based approach compared to the optical data-based approach. Figure 6-19 provides a possible explanation. In this figure the forest mapping results over a plantation in the south-eastern region of the study area, which is also covered by validation samples, is shown. As the SAR backscatter signal from the plantation is very similar to the signal received from forest areas, the probability to assign a pixel that represent the plantation to the class forest is very high for SAR data. Since the combined data stack includes more SAR bands than optical bands (52 versus 9) it is very likely that the influence of SAR data on the generation of the RF classifier is stronger as each split criterion is based on a random subset of the input features.

Table 6-12: Accuracy measures and their 95% confidence interval of the optical and combined data-based approaches

	NoB	OA [%]	UA Forest [%]	UA Non-forest [%]	PA Forest [%]	PA Non-forest [%]
Optical data-based approach	9	81.07 (±0.96)	87.62 (±0.96)	61.61 (±2.51)	87.16 (±0.75)	62.58 (±2.04)
Combined optical-SAR data-based approach	61	88.47 (±0.81)	88.73 (±0.83)	85.04 (±3.41)	98.75 (±0.28)	36.12 (±1.80)

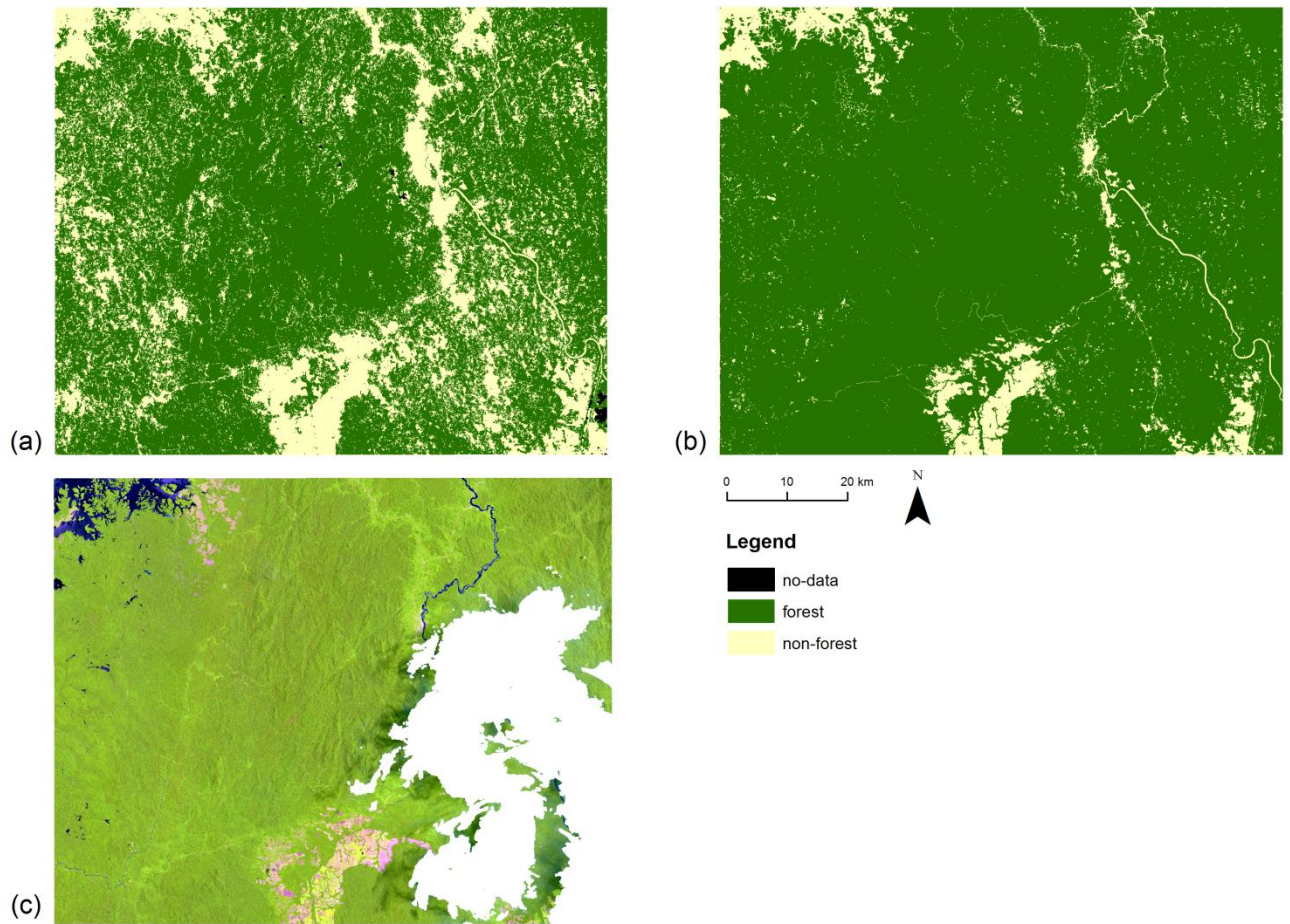


Figure 6-17: Forest status maps of the study: (a) optical approach, (b) combined approach, (c) S2 02.04.2017

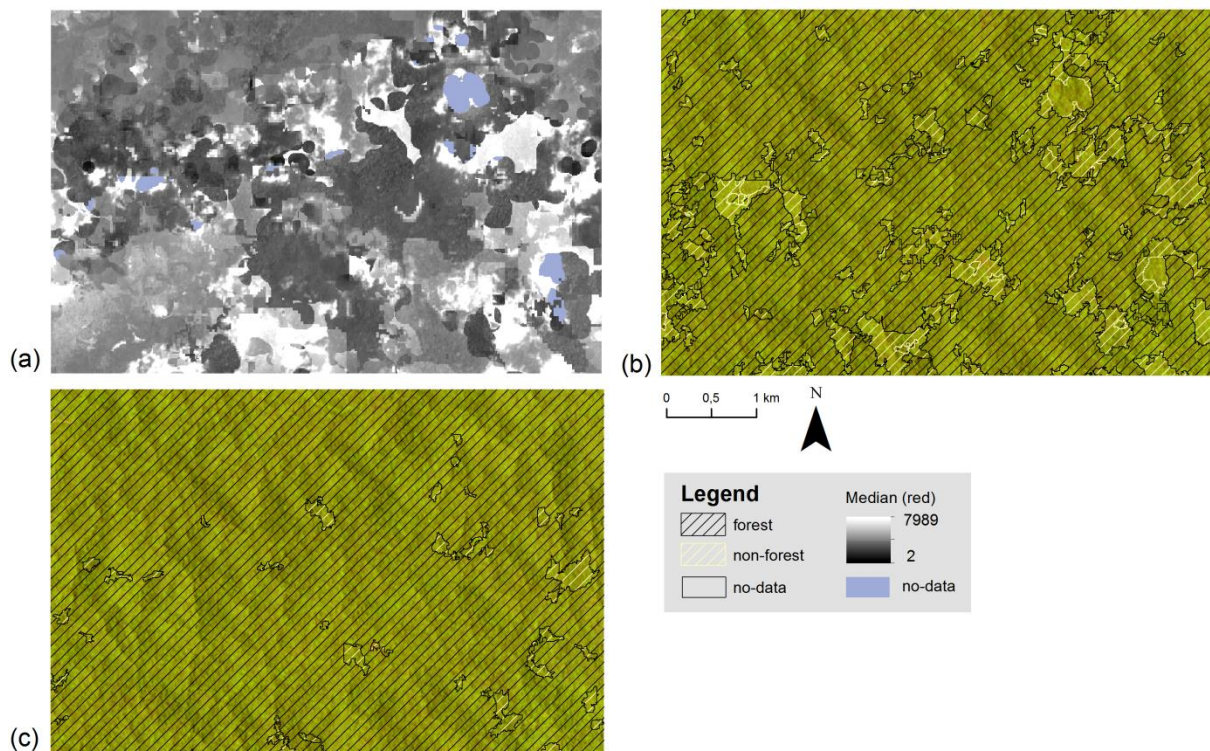


Figure 6-18: Forest mapping results for a subset of the study area: (a) temporal median of the red band, (b) optical approach, (c) combined approach

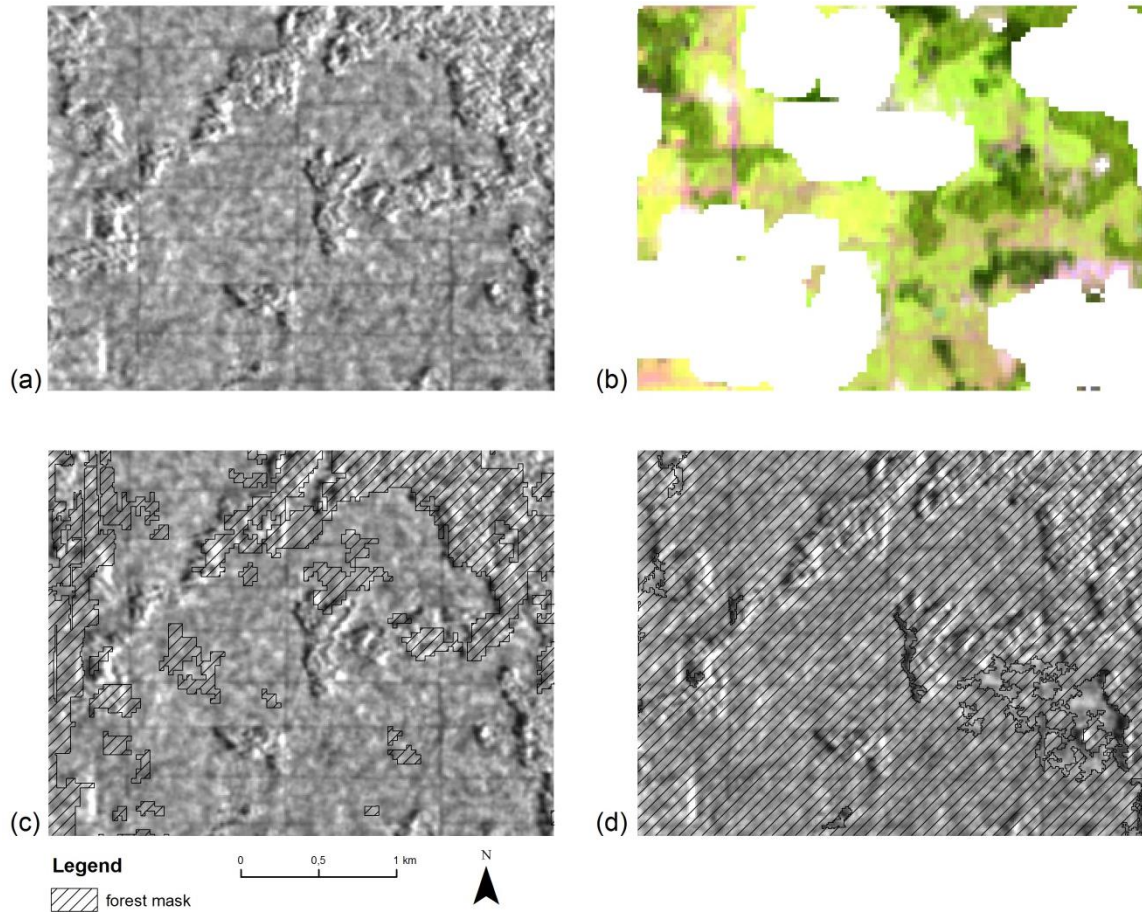


Figure 6-19: Classification results over the plantation in the southeast part of the study area: (a) S1 image 26.12.2016, (b) L8 06.03.2017, (c) optical data-based approach, (d) combined data-based approach

7 Conclusion

This thesis evaluates the performance of different forest mapping approaches based on optical (Sentinel-2 and Landsat 8) and SAR (Sentinel-1) satellite image time series. To generate a forest status map in humid tropical regions, single-sensor approaches as well as approaches using combined optical and SAR time series data are applied. Objects of investigation are:

1. The added value of time series data compared to mono-temporal data
2. The effects of the time series extent variations
3. The differences in performance of Maximum Likelihood and Random Forest classifiers
4. Differences in performance of a data-based and a result-based approach
5. The added value of the combination of optical and SAR time series data
6. Methods transferability

Objectives 1 to 5 are investigated in Peru. The second study area in Gabon is used to test the methods transferability.

Regarding the added value of time series data, forest mapping results for both, optical and SAR data, show that time series data produces higher accuracies in comparison to mono-temporal classification results. Additionally, the results achieved for the optical time series show that this applies for ML and RF classifier. The differences in obtained accuracies are more significant for optical data compared to SAR data.

To assess the impact of the time series extent, the optical result-based approach is used. All available 23 optical images between April 2013 and March 2016 are compared to a reduced time series involving images acquired within one year only. To capture possible forest loss and regrowth dynamics, two different weighting functions, dividing the time series into two and three periods respectively, are applied. These weighting functions assign observation of the second and third period more influence on classification results. The obtained results show that the selected time series extent is a critical component when the ML classifier is employed. The OA produced with all available data is lower compared to mono-temporal and the reduced time series. The RF mapping result achieved with the entire available time series data is better than the mono-temporal result, but lower than the results obtained with the reduced time series. Therefore, the conclusion can be drawn that the time series extent should be considered carefully. Too long observation periods might cause classification errors due to possible land cover changes. Regarding the application of weights, while ML produces the highest OA when the time series is divided into three periods and weighting functions are applied to the second and third period, the best RF result is achieved with the reduced time series without the use of any weights. This leads to the conclusion that the contribution of weights to improve classification results depends on the used classifier.

The differences in performance of the ML and RF classifier are tested with the optical time series data-based and result-based approach. For the result-based approach with the reduced time series, both classifiers perform equally well as the obtained OAs are almost identical. In contrast, within the data-based approach, classification accuracies obtained with the RF classifier are higher than the results obtained with the ML classifier. Moreover, the investigation of the impact of the defective blue temporal median reveals that the RF classifier is more robust against defective data. While classification accuracy increases

significantly for ML classifier, only a slight increase is observed for RF. From these findings it can be concluded that the RF classifier is more suitable for tropical forest mapping with time series data in Peru.

Within a forest mapping workflow incorporating image time series, the time series can be combined before the classification (data-based) or in a post-classification (result-based) step. In order to investigate the differences a data-based and a result-based approach is applied utilizing the optical time series as well as the combined time series. For the optical data-based approach a data stack of BOA reflectance bands and a stack of the temporal median of each spectral band are provided as input data for supervised classification. The median is chosen because of its robustness against outliers. Due to high rates of cloud cover in tropical regions the BOA reflectance stack is comprised by data gaps that do affect the calculation of ML and RF classification models and cause classification errors. While missing values within training samples make it impossible to calculate a ML classification model, the RF classifier can handle them during the generation of the classifier, but not the classification itself. Thus, a classification result is obtained with the RF classifier, but the probability of classification errors is very high. The optical result-based approach builds on mono-temporal forest/non-forest maps which are then combined in a post-classification analysis based on the proportion of forest votes on valid pixels. A comparison of the best results of both optical approaches reveals that no explicit conclusion can be drawn if the integration of time series data within a pre-classification analysis or post-classification analysis performs better when an optical time series is used as both approaches produce similar OAs. In contrast, mapping results for the combined data-based and result-based approach show a considerable difference. For the combined data-based approach the optical temporal median (without the blue band) and the SAR time series backscatter are combined in one image stack and used as classification input. The combined result-based approach is based on a Bayesian combination of two initial forest probability maps, one derived from optical and one from SAR data, and two maps that specify their reliability. A comparison of the results of both combined approaches shows that the data-based approach is more suitable to produce acceptable forest mapping accuracies than the Bayesian combination approach.

From the comparison of the results achieved with optical, SAR and combined time series data three conclusions can be drawn. First, considering the results achieved with the SAR time series, neither mono-temporal nor the used time series data are capable to produce a forest map with acceptable accuracies. The main reason for this can be found in the similarities in backscatter signals from forest and other land use classes. Secondly, results achieved for both optical time series approaches demonstrate the possibility to derive a forest status map with an acceptable overall accuracy. However, small data gaps due to clouds still remain. And third, the use of a combined optical-SAR time series within the data-based approach produces higher classification accuracies compared to optical and SAR time series results. However, in Peru, the result differs only slightly from the most promising results of the optical approaches.

In order to test the transferability of the method which produces the most promising result for Peru is applied to a second study area located in Gabon. As it produces the most accurate forest map according to OA, the combined data-based approach using the optical temporal median and SAR backscatter time series is applied to the second study area in Gabon. For comparison the data-based approach is also performed with the optical median only. In

contrast to Peru, results for Gabon clearly accentuate the benefits of the combination of optical and SAR data to improve forest mapping. The main reason for this lies in the availability and quality of optical satellite data, which is much worse for the Gabonese study area due to extremely high rates of cloud cover. Additionally, the cloud masks of S2 and L8 images lack accuracy, leading to a great number of remaining cloud and cloud shadow pixels. Consequently, the quality of the temporal median is much worse compared to the temporal median obtained for the Peruvian study area.

Finally, there are still some interesting points which could be investigated in further studies. Regarding optical data, further research needs to be done if the integration of dimensionality reduction and/or the utilization of classification input additional features such as indices would produce higher classification accuracies. The same applies to SAR data, where it would be worth investigating if the integration of textural and/or polarimetric features would improve forest mapping. As the combined optical-SAR result-based approach is based on initial maps produced using single sensor approaches, it can be assumed that a more accurate SAR-based forest status map is very likely to increase the classification accuracy. Furthermore, as RF classification is always performed with default parameters provided by the OTB, the effects of a modification of parameters settings on classification results needs to be investigated.

References

- Achard, F., Stibig, H.-J., Eva, H.D., Lindquist, E.J., Bouvet, A., Arino, O., Mayaux, P., 2010. Estimating tropical deforestation from Earth observation data. *Carbon Management* 1, 271–287.
- Almeida-Filho, R., Rosenqvist, A., Shimabukuro, Y., Silva-Gomez, R., 2007. Detecting deforestation with multitemporal L-band SAR imagery: A case study in western Brazilian Amazonia. *International Journal of Remote Sensing* 28, 1383–1390.
- Alparone, L., Aiazzi, B., Baronti, S., Garzelli, A., 2015. *Remote Sensing Image Fusion*. CRC Press.
- Antropov, O., Rauste, Y., Seifert, F.M., Hame, T., 2015. Selective logging of tropical forests observed using L- and C-band SAR satellite data, in: 2015 IEEE International Geoscience and Remote Sensing Symposium (IGARSS). Institute of Electrical and Electronics Engineers (IEEE).
- Appiah, D., Schröder, D., Forkuo, E., Bugri, J., 2015. Application of Geo-Information Techniques in Land Use and Land Cover Change Analysis in a Peri-Urban District of Ghana. *ISPRS International Journal of Geo-Information* 4, 1265–1289.
- Aschbacher, J., Milagro-Pérez, M.P., 2012. The European Earth monitoring (GMES) programme: Status and perspectives. *Remote Sensing of Environment* 120, 3–8.
- Asner, G.P., 2001. Cloud cover in Landsat observations of the Brazilian Amazon. *International Journal of Remote Sensing* 22, 3855–3862.
- Bamler, R., 2000. Principles Of Synthetic Aperture Radar. *Surveys in Geophysics* 21, 147–157.
- Banskota, A., Kayastha, N., Falkowski, M.J., Wulder, M.A., Froese, R.E., White, J.C., 2014. Forest Monitoring Using Landsat Time Series Data: A Review. *Canadian Journal of Remote Sensing* 40, 362–384.
- Belgiu, M., Drăguț, L., 2016. Random forest in remote sensing: A review of applications and future directions. *ISPRS Journal of Photogrammetry and Remote Sensing* 114, 24–31.
- Berger, M., Moreno, J., Johannessen, J.A., Levelt, P.F., Hanssen, R.F., 2012. ESA's sentinel missions in support of Earth system science. *Remote Sensing of Environment* 120, 84–90.
- Breiman, L., 2003. Manual-Setting Up, Using, And Understanding Random Forests V4.0. URL: https://www.stat.berkeley.edu/~breiman/Using_random_forests_v4.0.pdf
- Breiman, L., 2001. Random Forests. *Machine Learning* 45, 5–32.
- Broich, M., Hansen, M.C., Potapov, P., Adusei, B., Lindquist, E., Stehman, S.V., 2011. Time-series analysis of multi-resolution optical imagery for quantifying forest cover loss in Sumatra and Kalimantan, Indonesia. *International Journal of Applied Earth Observation and Geoinformation* 13, 277–291.
- Campbell, J.B., 1996. *Introduction to remote sensing*, 2. ed. ed. Taylor & Francis and The Guilford Press, London and New York.

- Carreiras, J.M.B., Jones, J., Lucas, R.M., Shimabukuro, Y.E., 2017. Mapping major land cover types and retrieving the age of secondary forests in the Brazilian Amazon by combining single-date optical and radar remote sensing data. *Remote Sensing of Environment* 194, 16–32.
- Clark, M.L., Aide, T.M., Grau, H.R., Riner, G., 2010. A scalable approach to mapping annual land cover at 250 m using MODIS time series data: A case study in the Dry Chaco ecoregion of South America. *Remote Sensing of Environment* 114, 2816–2832.
- Clauss, K., Ottinger, M., Kuenzer, C., 2018. Mapping rice areas with Sentinel-1 time series and superpixel segmentation. *International Journal of Remote Sensing* 39, 1399–1420.
- Clerici, N., Calderón, C.A.V., Posada, J.M., 2017. Fusion of Sentinel-1A and Sentinel-2A data for land cover mapping: a case study in the lower Magdalena region, Colombia. *Journal of Maps* 13, 718–726.
- Colditz, R.R., 2015. An evaluation of different training sample allocation schemes for discrete and continuous land cover classification using decision tree-based algorithms. *Remote Sensing* 7, 9655–9681.
- Collomb, J.-G., Mikissa, J.-B., Minnemeyer, S. (Eds.), 2000. A first look at logging in Gabon: a Global Forest Watch report. World Resources Institute, Washington, DC.
- Daboor, M., Howell, S., Shokr, M., Yackel, J., 2014. The Jeffries–Matusita distance for the case of complex Wishart distribution as a separability criterion for fully polarimetric SAR data. *International Journal of Remote Sensing* 35, 6859–6873.
- Dalponte, M., Ørka, H.O., Gobakken, T., Gianelle, D., Næsset, E., 2013. Tree species classification in boreal forests with hyperspectral data. *IEEE Transactions on Geoscience and Remote Sensing* 51, 2632–2645.
- Delgado-Aguilar, M.J., Fassnacht, F.E., Peralvo, M., Gross, C.P., Schmitt, C.B., 2017. Potential of TerraSAR-X and Sentinel 1 imagery to map deforested areas and derive degradation status in complex rain forests of Ecuador. *International Forestry Review* 19, 102–118.
- Deutscher, J., Gutjahr, K., Perko, R., Raggam, H., Hirschmugl, M., Schardt, M., 2017. Humid tropical forest monitoring with multi-temporal L-, C- and X-band SAR data, in: 2017 9th International Workshop on the Analysis of Multitemporal Remote Sensing Images (MultiTemp). IEEE, pp. 1–4.
- DeVries, B., Verbesselt, J., Kooistra, L., Herold, M., 2015. Robust monitoring of small-scale forest disturbances in a tropical montane forest using Landsat time series. *Remote Sensing of Environment* 161, 107–121.
- Drusch, M., Del Bello, U., Carlier, S., Colin, O., Fernandez, V., Gascon, F., Hoersch, B., Isola, C., Laberinti, P., Martimort, P., Meygret, A., Spoto, F., Sy, O., Marchese, F., Bargellini, P., 2012. Sentinel-2: ESA's Optical High-Resolution Mission for GMES Operational Services. *Remote Sensing of Environment* 120, 25–36.
- Emde, C., Buras-Schnell, R., Kylling, A., Mayer, B., Gasteiger, J., Hamann, U., Kylling, J., Richter, B., Pause, C., Dowling, T., Bugliaro, L., 2016. The libRadtran software

- package for radiative transfer calculations (version 2.0.1). *Geoscientific Model Development* 9, 1647–1672.
- Erinjeri, J.J., Singh, M., Kent, R., 2018. Mapping and assessment of vegetation types in the tropical rainforests of the Western Ghats using multispectral Sentinel-2 and SAR Sentinel-1 satellite imagery. *Remote Sensing of Environment* 216, 345–354.
- FAO, 2015. *Global Forest Resources Assessment 2015. How are the world's forests changing?*, Second edition. ed, Global forest resources assessment. URL: <http://www.fao.org/3/a-i4793e.pdf>
- FAO, 2000. *Global Forest Resources Assessment 2000*. URL: <http://www.fao.org/docrep/004/Y1997E/y1997e1m.htm#bm58>
- Fernandez-Beltran, R., Haut, J.M., Paoletti, M.E., Plaza, J., Plaza, A., Pla, F., 2018. Multimodal Probabilistic Latent Semantic Analysis for Sentinel-1 and Sentinel-2 Image Fusion. *IEEE Geoscience and Remote Sensing Letters* 1–5.
- Fletcher, K. (Ed.), 2012. *ESA's optical high-resolution mission for GMES operational services*, ESA SP. ESA Communications, Noordwijk.
- Foody, G.M., 2009. Classification accuracy comparison: Hypothesis tests and the use of confidence intervals in evaluations of difference, equivalence and non-inferiority. *Remote Sensing of Environment* 113, 1658–1663.
- Franklin, S.E., Ahmed, O.S., Wulder, M.A., White, J.C., Hermosilla, T., Coops, N.C., 2015. Large Area Mapping of Annual Land Cover Dynamics Using Multitemporal Change Detection and Classification of Landsat Time Series Data. *Canadian Journal of Remote Sensing* 41, 293–314.
- Frost, V.S., Stiles, J.A., Shanmugan, K.S., Holtzman, J.C., 1982. A Model for Radar Images and Its Application to Adaptive Digital Filtering of Multiplicative Noise. *IEEE Transactions on Pattern Analysis and Machine Intelligence PAMI-4*, 157–166.
- Gao, F., Masek, J., Schwaller, M., Hall, F., 2006. On the blending of the Landsat and MODIS surface reflectance: predicting daily Landsat surface reflectance. *IEEE Transactions on Geoscience and Remote Sensing* 44, 2207–2218.
- Gao, F., Morisette, J.T., Wolfe, R.E., Ederer, G., Pedelty, J., Masuoka, E., Myneni, R., Tan, B., Nightingale, J., 2008. An Algorithm to Produce Temporally and Spatially Continuous MODIS-LAI Time Series. *IEEE Geoscience and Remote Sensing Letters* 5, 60–64.
- Gardner, T.A., Barlow, J., Chazdon, R., Ewers, R.M., Harvey, C.A., Peres, C.A., Sodhi, N.S., 2009. Prospects for tropical forest biodiversity in a human-modified world. *Ecology Letters* 12, 561–582.
- Gebhardt, S., Wehrmann, T., Ruiz, M., Maeda, P., Bishop, J., Schramm, M., Kopeinig, R., Cartus, O., Kellndorfer, J., Ressl, R., Santos, L., Schmidt, M., 2014. MAD-MEX: Automatic Wall-to-Wall Land Cover Monitoring for the Mexican REDD-MRV Program Using All Landsat Data. *Remote Sensing* 6, 3923–3943.
- Geist, H.J., Lambin, E.F., 2002. Proximate Causes and Underlying Driving Forces of Tropical Deforestation. *BioScience* 52, 143.

- Glanz, H., Carvalho, L., Sulla-Menashe, D., Friedl, M.A., 2014. A parametric model for classifying land cover and evaluating training data based on multi-temporal remote sensing data. *ISPRS Journal of Photogrammetry and Remote Sensing* 97, 219–228.
- GOFC-GOLD, 2016. A sourcebook of methods and procedures for monitoring and reporting anthropogenic greenhouse gas emissions and removals caused by deforestation, gains and losses of carbon stocks in forests remaining forests, and forestation. GOFC-GOLD Report version COP22-1, (GOFC-GOLD Land Cover Project Office, Wageningen University, The Netherlands).
- GOFC-GOLD, 2014. A sourcebook of methods and procedures for monitoring and reporting anthropogenic greenhouse gas emissions and removals caused by deforestation, gains and losses of carbon stocks in forests remaining forests, and forestation.
- Gómez, C., White, J.C., Wulder, M.A., 2016. Optical remotely sensed time series data for land cover classification: A review. *ISPRS Journal of Photogrammetry and Remote Sensing* 116, 55–72.
- Hagensieker, R., Waske, B., 2017. Synergetic potentials of C-band SAR and multi-spectral imagery for tropical classifications in Northern Mato Grosso (BR), in: 2017 IEEE International Geoscience and Remote Sensing Symposium (IGARSS). Presented at the 2017 IEEE International Geoscience and Remote Sensing Symposium (IGARSS), IEEE, Fort Worth, TX, pp. 5486–5489.
- Hame, T., Kilpi, J., Ahola, H.A., Rauste, Y., Antropov, O., Rautiainen, M., Sirro, L., Bounpone, S., 2013. Improved Mapping of Tropical Forests With Optical and SAR Imagery, Part I: Forest Cover and Accuracy Assessment Using Multi-Resolution Data. *IEEE Journal of Selected Topics in Applied Earth Observations and Remote Sensing* 6, 74–91.
- Hansen, M.C., Krylov, A., Tyukavina, A., Potapov, P.V., Turubanova, S., Zutta, B., Ifo, S., Margono, B., Stolle, F., Moore, R., 2016. Humid tropical forest disturbance alerts using Landsat data. *Environmental Research Letters* 11, 034008.
- Hansen, M.C., Potapov, P.V., Moore, R., Hancher, M., Turubanova, S.A., Tyukavina, A., Thau, D., Stehman, S.V., Goetz, S.J., Loveland, T.R., Kommareddy, A., Egorov, A., Chini, L., Justice, C.O., Townshend, J.R.G., 2013. High-resolution global maps of 21st-century forest cover change. *Science (New York, N.Y.)* 342, 850–853.
- Hansen, M.C., Roy, D.P., Lindquist, E., Adusei, B., Justice, C.O., Altstatt, A., 2008a. A method for integrating MODIS and Landsat data for systematic monitoring of forest cover and change in the Congo Basin. *Remote Sensing of Environment* 112, 2495–2513.
- Hansen, M.C., Stehman, S.V., Potapov, P.V., Loveland, T.R., Townshend, J.R.G., DeFries, R.S., Pittman, K.W., Arunarwati, B., Stolle, F., Steininger, M.K., Carroll, M., Dimiceli, C., 2008b. Humid tropical forest clearing from 2000 to 2005 quantified by using multitemporal and multiresolution remotely sensed data. *Proceedings of the National Academy of Sciences of the United States of America* 105, 9439–9444.
- Herold, M., 2009. An assessment of national forest monitoring capabilities in tropical non-Annex I countries: Recommendations for capacity building.

- Hirschmugl, M., Deutscher, J., Gutjahr, K.-H., Sobe, C., Schardt, M., 2017a. Combined use of SAR and optical time series data for near real-time forest disturbance mapping, in: 2017 9th International Workshop on the Analysis of Multitemporal Remote Sensing Images (MultiTemp). IEEE, pp. 1–4.
- Hirschmugl, M., Gallaun, H., Dees, M., Datta, P., Deutscher, J., Koutsias, N., Schardt, M., 2017b. Methods for Mapping Forest Disturbance and Degradation from Optical Earth Observation Data: a Review. *Current Forestry Reports* 3, 32–45.
- Hirschmugl, M., Steinegger, M., Gallaun, H., Schardt, M., 2014. Mapping Forest Degradation due to Selective Logging by Means of Time Series Analysis: Case Studies in Central Africa. *Remote Sensing* 6, 756–775.
- Hirschmugl, M., Sobe, C., Deutscher, J., Schardt, M., 2018. Combined Use of Optical and Synthetic Aperture Radar Data for REDD+ Applications in Malawi. *Land* 7(4),116.
- Hoan, N.T., Tateishi, R., Alsaaidh, B., Ngigi, T., Alimuddin, I., Johnson, B., 2013. Tropical forest mapping using a combination of optical and microwave data of ALOS. *International Journal of Remote Sensing* 34, 139–153.
- Horning, N., 2010. Random Forests : An algorithm for image classification and generation of continuous fields data sets, in: *Proceedings of the International Conference on Geoinformatics for Spatial Infrastructure Development in Earth and Allied Sciences*, Osaka, Japan.
- Hosonuma, N., Herold, M., de Sy, V., de Fries, R.S., Brockhaus, M., Verchot, L., Angelsen, A., Romijn, E., 2012. An assessment of deforestation and forest degradation drivers in developing countries. *Environmental Research Letters* 7, 044009.
- IPCC, 2006. Guidelines for National Greenhouse Gas Inventories, Volume 4: Agriculture, Forestry and Other Land Use. URL: <http://www.ipcc-nggip.iges.or.jp/public/2006gl/index.html>
- IPCC, 2003. Good Practice Guidance for Land Use, Land-Use Change and Forestry (GPG-LULUCF). URL: http://www.ipcc-nggip.iges.or.jp/public/gpglulucf/gpglulucf_contents.html
- Irons, J.R., Dwyer, J.L., Barsi, J.A., 2012. The next Landsat satellite: The Landsat Data Continuity Mission. *Remote Sensing of Environment* 122, 11–21.
- Ishwaran, H., Kogalur, U.B., Blackstone, E.H., Lauer, M.S., 2008. Random survival forests. *The Annals of Applied Statistics* 2, 841–860.
- Jia, K., Liang, S., Zhang, L., Wei, X., Yao, Y., Xie, X., 2014. Forest cover classification using Landsat ETM+ data and time series MODIS NDVI data. *International Journal of Applied Earth Observation and Geoinformation* 33, 32–38.
- Jönsson, P., Cai, Z., Melaas, E., Friedl, M., Eklundh, L., 2018. A Method for Robust Estimation of Vegetation Seasonality from Landsat and Sentinel-2 Time Series Data. *Remote Sensing* 10, 635.
- Joshi, N., Baumann, M., Ehammer, A., Fensholt, R., Grogan, K., Hostert, P., Jepsen, M.R., Kuemmerle, T., Meyfroidt, P., Mitchard, E.T., others, 2016. A review of the

- application of optical and radar remote sensing data fusion to land use mapping and monitoring. *Remote Sensing* 8, 70.
- Joshi, N., Mitchard, E.T., Woo, N., Torres, J., Moll-Rocek, J., Ehammer, A., Collins, M., Jepsen, M.R., Fensholt, R., 2015. Mapping dynamics of deforestation and forest degradation in tropical forests using radar satellite data. *Environmental Research Letters* 10, 034014.
- Keenan, R.J., Reams, G.A., Achard, F., de Freitas, J.V., Grainger, A., Lindquist, E., 2015. Dynamics of global forest area: Results from the FAO Global Forest Resources Assessment 2015. *Forest Ecology and Management* 352, 9–20.
- Kissinger, G. b., Herold, M. b., de Sy, V. b., 2012. Drivers of deforestation and forest degradation: A synthesis report for REDD+ policymakers. The Government of the UK and Norway.
- Koch, K.-R., 1990. Bayes' Theorem, in: *Bayesian Inference with Geodetic Applications*. Springer Berlin Heidelberg, Berlin, Heidelberg, pp. 4–8.
- Kontgis, C., Warren, M.S., Skillman, S.W., Chartrand, R., Moody, D.I., 2017. Leveraging Sentinel-1 time-series data for mapping agricultural land cover and land use in the tropics, in: *2017 9th International Workshop on the Analysis of Multitemporal Remote Sensing Images (MultiTemp)*. Presented at the 2017 9th International Workshop on the Analysis of Multitemporal Remote Sensing Images (MultiTemp), IEEE, Brugge, Belgium, pp. 1–4.
- Kuenzer, C., Dech, S., Wagner, W., 2015. Remote Sensing Time Series Revealing Land Surface Dynamics: Status Quo and the Pathway Ahead, in: Kuenzer, C., Dech, S., Wagner, W. (Eds.), *Remote Sensing Time Series, Remote Sensing and Digital Image Processing*. Springer International Publishing, Cham, pp. 1–24.
- Kuplich, T.M., 2006. Classifying regenerating forest stages in Amazonia using remotely sensed images and a neural network. *Forest Ecology and Management* 234, 1–9.
- Lambert, M.-J., Traoré, P.C.S., Blaes, X., Baret, P., Defourny, P., 2018. Estimating smallholder crops production at village level from Sentinel-2 time series in Mali's cotton belt. *Remote Sensing of Environment* 216, 647–657.
- Lambin, E.F., Gibbs, H.K., Heilmayr, R., Carlson, K.M., Fleck, L.C., Garrett, R.D., Le Polain de Waroux, Y., McDermott, C.L., McLaughlin, D., Newton, P., Nolte, C., Pacheco, P., Rausch, L.L., Streck, C., Thorlakson, T., Walker, N.F., 2018. The role of supply-chain initiatives in reducing deforestation. *Nature Climate Change* 8, 109–116.
- Langner, A., Miettinen, J., Kukkonen, M., Vancutsem, C., Simonetti, D., Vieilledent, G., Verhegghen, A., Gallego, J., Stibig, H.-J., 2018. Towards Operational Monitoring of Forest Canopy Disturbance in Evergreen Rain Forests: A Test Case in Continental Southeast Asia. *Remote Sensing* 10, 544.
- Laurance, W.F., Alonso, A., Lee, M., Campbell, P., 2006. Challenges for forest conservation in Gabon, Central Africa. *Futures* 38, 454–470.
- Lee, J.-S., Jurkevich, L., Dewaele, P., Wambacq, P., Oosterlinck, A., 1994. Speckle filtering of synthetic aperture radar images: A review. *Remote Sensing Reviews* 8, 313–340.

- Li, G., Lu, D., Moran, E., Dutra, L., Batistella, M., 2012. A comparative analysis of ALOS PALSAR L-band and RADARSAT-2 C-band data for land-cover classification in a tropical moist region. *ISPRS Journal of Photogrammetry and Remote Sensing* 70, 26–38.
- Liaw, A., Wiener, M., 2002. Classification and Regression by RandomForest. *R NEWS* 18–23.
- Lillesand, T.M., Kiefer, R.W., Chipman, J.W., 2015. Remote sensing and image interpretation, Seventh edition. ed. John Wiley & Sons, Inc, Hoboken, N.J.
- Liu, D., Cai, S., 2012. A Spatial-Temporal Modeling Approach to Reconstructing Land-Cover Change Trajectories from Multi-temporal Satellite Imagery. *Annals of the Association of American Geographers* 102, 1329–1347.
- López-Caloca, A.A., Tapia-Silva, F.O., Rivera, G., 2018. Sentinel-1 Satellite Data as a Tool for Monitoring Inundation Areas near Urban Areas in the Mexican Tropical Wet, in: Glavan, M. (Ed.), *Water Challenges of an Urbanizing World*.
- Lu, M., Hamunyela, E., Verbesselt, J., Pebesma, E., 2017. Dimension Reduction of Multi-Spectral Satellite Image Time Series to Improve Deforestation Monitoring. *Remote Sensing* 9, 1025.
- Main-Knorn, M., Pflug, B., Debaecker, V., Louis, J., 2015. Calibration and validation plan for the LA processor and products of the Sentinel-2 Mission. *ISPRS - International Archives of the Photogrammetry, Remote Sensing and Spatial Information Sciences XL-7/W3*, 1249–1255.
- Mandanici, E., Bitelli, G., 2016. Preliminary Comparison of Sentinel-2 and Landsat 8 Imagery for a Combined Use. *Remote Sensing* 8, 1014.
- Martimort, P., Arino, O., Berger, M., Biasutti, R., Carnicero, B., Del Bello, U., Fernandez, V., Gascon, F., Greco, B., Silvestrin, P., Spoto, F., Sy, O., 2007. Sentinel-2 optical high resolution mission for GMES operational services, in: 2007 IEEE International Geoscience and Remote Sensing Symposium. IEEE, pp. 2677–2680.
- Martinis, S., Plank, S., Ćwik, K., 2018. The Use of Sentinel-1 Time-Series Data to Improve Flood Monitoring in Arid Areas. *Remote Sensing* 10, 583.
- Medjibe, V.P., Putz, F.E., Starkey, M.P., Ndouna, A.A., Memiaghe, H.R., 2011. Impacts of selective logging on above-ground forest biomass in the Monts de Cristal in Gabon. *Forest Ecology and Management* 262, 1799–1806.
- Mellor, A., Boukir, S., Haywood, A., Jones, S., 2015. Exploring issues of training data imbalance and mislabelling on random forest performance for large area land cover classification using the ensemble margin. *ISPRS Journal of Photogrammetry and Remote Sensing* 105, 155–168.
- Mermoz, S., Le Toan, T., 2016. Forest Disturbances and Regrowth Assessment Using ALOS PALSAR Data from 2007 to 2010 in Vietnam, Cambodia and Lao PDR. *Remote Sensing* 8, 217.

- Motohka, T., Shimada, M., Uryu, Y., Setiabudi, B., 2014. Using time series PALSAR gamma nought mosaics for automatic detection of tropical deforestation: A test study in Riau, Indonesia. *Remote Sensing of Environment* 155, 79–88.
- Mueller-Wilm, U., 2017. S2 MPC. Sen2Cor Configuration and User Manual. URL: http://step.esa.int/thirdparties/sen2cor/2.4.0/Sen2Cor_240_Documentation_PDF/S2-PDGS-MPC-L2A-SUM-V2.4.0.pdf
- Müller, H., Griffiths, P., Hostert, P., 2016. Long-term deforestation dynamics in the Brazilian Amazon—Uncovering historic frontier development along the Cuiabá–Santarém highway. *International Journal of Applied Earth Observation and Geoinformation* 44, 61–69.
- Nicholaides, J.J., Bandy, D.E., Sanchez, P.A., Benites, J.R., Villachica, J.H., Coutu, A.J., Valverde, C.S., 1985. Agricultural Alternatives for the Amazon Basin. *BioScience* 35, 279–285.
- Niculescu, S., Ienco, D., Hanganu, J., 2018. Application of deep learning of multi-temporal Sentinel-1 images for the classification of costal vegetation zone of the Danube delta. *ISPRS - International Archives of the Photogrammetry, Remote Sensing and Spatial Information Sciences XLII-3*, 1311–1318.
- Oestreich, M., Romberg, O., 2012. *Keine Panik vor Statistik!* Vieweg+Teubner Verlag, Wiesbaden.
- Olofsson, P., Foody, G.M., Stehman, S.V., Woodcock, C.E., 2013. Making better use of accuracy data in land change studies: Estimating accuracy and area and quantifying uncertainty using stratified estimation. *Remote Sensing of Environment* 129, 122–131.
- ORFEO Toolbox, 2018. OTB CookBook. TrainImagesClassifier - Train a classifier from multiple images. URL: https://www.orfeo-toolbox.org/CookBook/Applications/app_TrainImagesClassifier.html
- Oshiro, T.M., Perez, P.S., Baranauskas, J.A., 2012. How Many Trees in a Random Forest?, in: Perner, P. (Ed.), *Machine Learning and Data Mining in Pattern Recognition*, Lecture Notes in Computer Science Lecture Notes in Artificial Intelligence. Springer, Berlin, pp. 154–168.
- Ottinger, M., Clauss, K., Kuenzer, C., 2017. Large-Scale Assessment of Coastal Aquaculture Ponds with Sentinel-1 Time Series Data. *Remote Sensing* 9, 440.
- Padoch, C., Pinedo-Vasquez, M., 2010. Saving Slash-and-Burn to Save Biodiversity: Saving Slash-and-Burn. *Biotropica* 42, 550–552.
- Palm, C.A., Alegre, J.C., Arevalo, L., Mutuo, P.K., Mosier, A.R., Coe, R., 2002. Nitrous oxide and methane fluxes in six different land use systems in the Peruvian Amazon: N₂O and CH₄ fluxes from land uses in Amazon. *Global Biogeochemical Cycles* 16, 21-1-21–13.
- Pan, Y., Birdsey, R.A., Fang, J., Houghton, R., Kauppi, P.E., Kurz, W.A., Phillips, O.L., Shvidenko, A., Lewis, S.L., Canadell, J.G., Ciais, P., Jackson, R.B., Pacala, S.W., McGuire, A.D., Piao, S., Rautiainen, A., Sitch, S., Hayes, D., 2011. A large and persistent carbon sink in the world's forests. *Science (New York, N.Y.)* 333, 988–993.

- Parker, C., Mitchell, A., Trivedi, M., Mardas, N., 2009. The Little REDD+ Book: An updated guide to governmental and non-governmental proposals for reducing emissions from deforestation and degradation. URL: <https://theredddesk.org/sites/default/files/resources/pdf/2009/The-Little-Redd-Book.pdf>
- Perko, R., Raggam, H., Gutjahr, K., Schardt, M., 2011. Using worldwide available TerraSAR-X data to calibrate the geo-location accuracy of optical sensors, in: 2011 IEEE International Geoscience and Remote Sensing Symposium. IEEE, Piscataway, NJ, pp. 2551–2554.
- Pohl, C., Loong, C.K., van Genderen, J., 2015. Multisensor approach to oil palm plantation monitoring using data fusion and GIS, in: ACRS 2015 - 36th Asian Conference on Remote Sensing: Fostering Resilient Growth in Asia, Proceedings. Presented at the 36th Asian Conference on Remote Sensing: Fostering Resilient Growth in Asia, ACRS 2015 - Quezon City, Metro Manila, Philippines, Asian Association on Remote Sensing.
- Quegan, T., S. an. Quegan, 1998. Analysing multitemporal SAR images. Anais IX Simposio Brasileiro de Sensoriamento Remoto 1183–1194.
- Reiche, J., 2015. Combining SAR and optical satellite image time series for tropical forest monitoring (PhD thesis). Wageningen University, Wageningen, NL.
- Reiche, J., de Bruin, S., Hoekman, D., Verbesselt, J., Herold, M., 2015a. A Bayesian Approach to Combine Landsat and ALOS PALSAR Time Series for Near Real-Time Deforestation Detection. *Remote Sensing* 7, 4973–4996.
- Reiche, J., Hamunyela, E., Verbesselt, J., Hoekman, D., Herold, M., 2018. Improving near-real time deforestation monitoring in tropical dry forests by combining dense Sentinel-1 time series with Landsat and ALOS-2 PALSAR-2. *Remote Sensing of Environment* 204, 147–161.
- Reiche, J., Verbesselt, J., Hoekman, D., Herold, M., 2015b. Fusing Landsat and SAR time series to detect deforestation in the tropics. *Remote Sensing of Environment* 156, 276–293.
- Richter, R., Lous, J., Berthelot, B., 2011. Sentinel-2 MSI – Level 2A Products Algorithm Theoretical Basis Document.
- Rodriguez-Galiano, V.F., Ghimire, B., Rogan, J., Chica-Olmo, M., Rigol-Sanchez, J.P., 2012. An assessment of the effectiveness of a random forest classifier for land-cover classification. *ISPRS Journal of Photogrammetry and Remote Sensing* 67, 93–104.
- Ron Hagensieker, Björn Waske, 2018. Evaluation of Multi-Frequency SAR Images for Tropical Land Cover Mapping. *Remote Sensing* 10, 257.
- Roy, D.P., Ju, J., Kline, K., Scaramuzza, P.L., Kovalskyy, V., Hansen, M., Loveland, T.R., Vermote, E., Zhang, C., 2010. Web-enabled Landsat Data (WELD): Landsat ETM+ composited mosaics of the conterminous United States. *Remote Sensing of Environment* 114, 35–49.
- Roy, D.P., Wulder, M.A., Loveland, T.R., C.E., W., Allen, R.G., Anderson, M.C., Helder, D., Irons, J.R., Johnson, D.M., Kennedy, R., Scambos, T.A., Schaaf, C.B., Schott, J.R.,

- Sheng, Y., Vermote, E.F., Belward, A.S., Bindschadler, R., Cohen, W.B., Gao, F., Hipple, J.D., Hostert, P., Huntington, J., Justice, C.O., Kilic, A., Kovalsky, V., Lee, Z.P., Lyburner, L., Masek, J.G., McCorkel, J., Shuai, Y., Trezza, R., Vogelmann, J., Wynne, R.H., Zhu, Z., 2014. Landsat-8: Science and product vision for terrestrial global change research. *Remote Sensing of Environment* 145, 154–172.
- Rozenstein, O., Haymann, N., Kaplan, G., Tanny, J., 2018. Estimating cotton water consumption using a time series of Sentinel-2 imagery. *Agricultural Water Management* 207, 44–52.
- Sanchez, P.A., Nureña S., M.A., 1972. Upland rice improvement under shifting cultivation systems in the Amazon Basin of Peru, Tech. bul. / North Carolina Agricultural Experiment Station; no. 210. North Carolina Agricultural Experiment Station and Peruvian Ministry of Agriculture, cooperating, [Raleigh, N.C.].
- Schäfer, P., Pflugmacher, D., Hostert, P., Leser, U., 2018. Classifying land cover from satellite images using time series analytics.
- Schneibel, A., Frantz, D., Röder, A., Stellmes, M., Fischer, K., Hill, J., 2017. Using Annual Landsat Time Series for the Detection of Dry Forest Degradation Processes in South-Central Angola. *Remote Sensing* 9.
- Scholz, I., Schmidt, L., 2008. Reducing Emissions from Deforestation and Forest Degradation in Developing Countries: Meeting the Main Challenges Ahead. Deutsches Institut für Entwicklungspolitik.
- Scott, 2015. The Curse of Dimensionality and Dimension Reduction, in: *Multivariate Density Estimation*. John Wiley & Sons, Inc, Hoboken, NJ, pp. 217–240.
- Sedano, F., Kempeneers, P., Hurtt, G., 2014. A Kalman Filter-Based Method to Generate Continuous Time Series of Medium-Resolution NDVI Images. *Remote Sensing* 6, 12381–12408.
- Sheng, Y., Xia, Z., 1996. Comprehensive Evaluation of Filters for Radar Speckle Suppression; Geoscience and Remote Sensing Symposium. IGARSS '96; Remote Sensing for a Sustainable Future 3, 1559–1561.
- Shimabukuro, Y., 2006. Near real time detection of deforestation in the Brazilian Amazon using MODIS imagery. *Ambiente e Agua - An Interdisciplinary Journal of Applied Science* 1, 37–47.
- Shimada, M., Itoh, T., Motooka, T., Watanabe, M., Shiraishi, T., Thapa, R., Lucas, R., 2014. New global forest/non-forest maps from ALOS PALSAR data (2007–2010). *Remote Sensing of Environment* 155, 13–31.
- Shimizu, K., Ponce-Hernandez, R., Ahmed, O.S., Ota, T., Win, Z.C., Mizoue, N., Yoshida, S., 2017. Using Landsat time series imagery to detect forest disturbance in selectively logged tropical forests in Myanmar. *Canadian Journal of Forest Research* 47, 289–296.
- Simons, H., 2001. FRA 2000. Global Ecological Zoning for the Global Forest Resources Assessment 2000, FRA Working Papers 56. FAO, Rome.

- Small, D., 2011. Flattening Gamma: Radiometric Terrain Correction for SAR Imagery. *IEEE Transactions on Geoscience and Remote Sensing* 49, 3081–3093.
- Sothe, C., Almeida, C.M. de, Liesenberg, V., Schimalski, M.B., 2017. Evaluating Sentinel-2 and Landsat-8 Data to Map Sucessional Forest Stages in a Subtropical Forest in Southern Brazil. *Remote Sensing* 9, 838.
- Souza, J.C., Siqueira, J., Sales, M., Fonseca, A., Ribeiro, J., Numata, I., Cochrane, M., Barber, C., Roberts, D., Barlow, J., 2013. Ten-Year Landsat Classification of Deforestation and Forest Degradation in the Brazilian Amazon. *Remote Sensing* 5, 5493–5513.
- Suhet, 2015. Sentinel-2 User Handbook 1.2. URL: https://sentinels.copernicus.eu/documents/247904/685211/Sentinel-2_User_Handbook
- Suhet, 2013. Sentinel-1 User Handbook. URL: https://sentinel.esa.int/documents/247904/685163/Sentinel-1_User_Handbook
- Sukawattanavijit, C., Chen, J., Zhang, H., 2017. GA-SVM Algorithm for Improving Land-Cover Classification Using SAR and Optical Remote Sensing Data. *IEEE Geoscience and Remote Sensing Letters* 14, 284–288.
- Torbick, N., Chowdhury, D., Salas, W., Qi, J., 2017. Monitoring Rice Agriculture across Myanmar Using Time Series Sentinel-1 Assisted by Landsat-8 and PALSAR-2. *Remote Sensing* 9, 119.
- Torres, R., Snoeij, P., Geudtner, D., Bibby, D., Davidson, M., Attema, E., Potin, P., Rommen, B., Floury, N., Brown, M., Traver, I.N., Deghaye, P., Duesmann, B., Rosich, B., Miranda, N., Bruno, C., L'Abbate, M., Croci, R., Pietropaolo, A., Huchler, M., Rostan, F., 2012. GMES Sentinel-1 mission. *Remote Sensing of Environment* 120, 9–24.
- Turner, B.L., Lambin, E.F., Reenberg, A., 2007. The emergence of land change science for global environmental change and sustainability. *Proceedings of the National Academy of Sciences* 104, 20666–20671.4
- UNFCCC, 2007. Report of the Conference of the Parties on its thirteenth session, held in Bali from 3 to 15 December 2007 Addendum Part Two: Action taken by the Conference of the Parties at its thirteenth session. UNFCCC.
- U.S. Agency for International Development (USAID), 2015. Towards Zero-Deforestation Oil Palm in Peru: Understanding Actors, Markets, and Barriers. Forest Carbon, Markets and Communities (FCMC) Program.
- U.S. Geological Survey (USGS), 2018. Landsat 8 Surface Reflectance Code (LaSRC) Product. URL: https://landsat.usgs.gov/sites/default/files/documents/lasrc_product_guide.pdf
- Vaglio Laurin, G., Liesenberg, V., Chen, Q., Guerriero, L., Del Frate, F., Bartolini, A., Coomes, D., Wilebore, B., Lindsell, J., Valentini, R., 2013. Optical and SAR sensor synergies for forest and land cover mapping in a tropical site in West Africa. *International Journal of Applied Earth Observation and Geoinformation* 21, 7–16.
- van der Werf, G.R., Morton, D.C., Defries, R.S., Olivier, J.G.J., Kasibhatla, P.S., Jackson, R.B., Collatz, G.J., Randerson, J.T., 2009. CO₂ emissions from forest loss. *Nature Geoscience* 2, 737–73.

- Verhegghen, A., Eva, H., Ceccherini, G., Achard, F., Gond, V., Gourlet-Fleury, S., Cerutti, P.O., 2016. The Potential of Sentinel Satellites for Burnt Area Mapping and Monitoring in the Congo Basin Forests. *Remote Sensing* 8, 986.
- Waldner, F., Lambert, M.-J., Li, W., Weiss, M., Demarez, V., Morin, D., Marais-Sicre, C., Hagolle, O., Baret, F., Defourny, P., 2015. Land Cover and Crop Type Classification along the Season Based on Biophysical Variables Retrieved from Multi-Sensor High-Resolution Time Series. *Remote Sensing* 7, 10400.
- Walker, W.S., Stickler, C.M., Kellndorfer, J.M., Kirsch, K.M., Nepstad, D.C., 2010. Large-area classification and mapping of forest and land cover in the Brazilian Amazon: A comparative analysis of ALOS/PALSAR and Landsat data sources. *IEEE Journal of Selected Topics in Applied Earth Observations and Remote Sensing* 3, 594–604.
- Waske, B., van der Linden, S., 2008. Classifying multilevel imagery from SAR and optical sensors by decision fusion. *IEEE Transactions on Geoscience and Remote Sensing* 46, 1457–1466.
- White, J., Wulder, M., Hobart, G., Luther, J., Hermosilla, T., Griffiths, P., Coops, N., Hall, R., Hostert, P., Dyk, A., others, 2014. Pixel-based image compositing for large-area dense time series applications and science. *Canadian Journal of Remote Sensing* 40, 192–212.
- Wulder, M.A., Masek, J.G., Cohen, W.B., Loveland, T.R., Woodcock, C.E., 2012. Opening the archive: How free data has enabled the science and monitoring promise of Landsat. *Remote Sensing of Environment* 122, 2–10.
- Yan, L., Roy, D.P., 2015. Improved time series land cover classification by missing-observation-adaptive nonlinear dimensionality reduction. *Remote Sensing of Environment* 158, 478–491.
- Zhai, Y., Qu, Z., Hao, L., 2018. Land Cover Classification Using Integrated Spectral, Temporal, and Spatial Features Derived from Remotely Sensed Images. *Remote Sensing* 10, 383.
- Zhang, Hui Lin, Yu Li, 2015. Impacts of Feature Normalization on Optical and SAR Data Fusion for Land Use/Land Cover Classification. *IEEE Geoscience and Remote Sensing Letters* 12, 1061–1065.
- Zhang, J., 2010. Multi-source remote sensing data fusion: status and trends. *International Journal of Image and Data Fusion* 1, 5–24.
- Zhang, J., Yang, J., Zhao, Z., Li, H., Zhang, Y., 2010. Block-regression based fusion of optical and SAR imagery for feature enhancement. *International Journal for Remote Sensing* 31, 2325–2345.
- Zhu, X., Chen, J., Gao, F., Chen, X., Masek, J.G., 2010. An enhanced spatial and temporal adaptive reflectance fusion model for complex heterogeneous regions. *Remote Sensing of Environment* 114, 2610–2623.
- Zhu, Z., Woodcock, C.E., 2012. Object-based cloud and cloud shadow detection in Landsat imagery. *Remote Sensing of Environment* 118, 83–94.

Annex: EO Data List

PERU

Table 0-1: Acquired Sentinel-1 Scenes

ASC/DSC Orbit Nr.	Date	Scene IDs	
DSC 69	03.03.2015	S1A_IW_GRDH_1SSV_20150303T104518_20150303T104543_004866_006103_A253.SAFE S1A_IW_GRDH_1SSV_20150303T104543_20150303T104608_004866_006103_403F.SAFE	
	27.03.2015	S1A_IW_GRDH_1SSV_20150327T104518_20150327T104543_005216_006968_F3E4.SAFE S1A_IW_GRDH_1SSV_20150327T104543_20150327T104608_005216_006968_B081.SAFE	
	11.04.2015	S1A_IW_GRDH_1SSV_20150411T232645_20150411T232710_005442_006EFA_4713.SAFE S1A_IW_GRDH_1SSV_20150411T232710_20150411T232735_005442_006EFA_347B.SAFE	
	20.04.2015	S1A_IW_GRDH_1SSV_20150420T104519_20150420T104544_005566_0071F5_A4F6.SAASC 120FE S1A_IW_GRDH_1SSV_20150420T104544_20150420T104609_005566_0071F5_6ADF.SAFE	
	14.05.2015	S1A_IW_GRDH_1SDV_20150514T104520_20150514T104545_005916_0079F6_DF0A.SAFE S1A_IW_GRDH_1SDV_20150514T104545_20150514T104610_005916_0079F6_D5D7.SAFE	
	07.06.2015	S1A_IW_GRDH_1SSV_20150607T104522_20150607T104547_006266_008357_8A0D.SAFE S1A_IW_GRDH_1SSV_20150607T104547_20150607T104612_006266_008357_5EA2.SAFE	
	01.07.2015	S1A_IW_GRDH_1SSV_20150701T104523_20150701T104548_006616_008D2F_384E.SAFE S1A_IW_GRDH_1SSV_20150701T104548_20150701T104613_006616_008D2F_97A2.SAFE	
	25.07.2015	S1A_IW_GRDH_1SSV_20150725T104524_20150725T104549_006966_009715_87C7.SAFE S1A_IW_GRDH_1SSV_20150725T104549_20150725T104614_006966_009715_643A.SAFE	
	18.08.2015	S1A_IW_GRDH_1SSV_20150818T104525_20150818T104550_007316_00A0AF_25F1.SAFE S1A_IW_GRDH_1SSV_20150818T104550_20150818T104615_007316_00A0AF_05D0.SAFE	
	11.09.2015	S1A_IW_GRDH_1SSV_20150911T104526_20150911T104551_007666_00AA3B_CF27.SAFE S1A_IW_GRDH_1SSV_20150911T104551_20150911T104616_007666_00AA3B_BADF.SAFE	
	05.10.2015	S1A_IW_GRDH_1SSV_20151005T104527_20151005T104552_008016_00B38D_D669.SAFE S1A_IW_GRDH_1SSV_20151005T104552_20151005T104617_008016_00B38D_7B3D.SAFE	
	29.10.2015	S1A_IW_GRDH_1SSV_20151029T104527_20151029T104552_008366_00BCFC_5E28.SAFE S1A_IW_GRDH_1SSV_20151122T104521_20151122T104546_008716_00C68D_EB8B.SAFE	
	22.11.2015	S1A_IW_GRDH_1SSV_20151122T104546_20151122T104611_008716_00C68D_278A.SAFE S1A_IW_GRDH_1SSV_20151216T104520_20151216T104545_009066_00D04C_F7C3.SAFE	
	16.12.2015	S1A_IW_GRDH_1SSV_20151216T104545_20151216T104610_009066_00D04C_0DEC.SAFE S1A_IW_GRDH_1SSV_20160109T104519_20160109T104544_009416_00DA47_DF34.SAFE	
	09.01.2016	S1A_IW_GRDH_1SSV_20160109T104544_20160109T104609_009416_00DA47_D348.SAFE S1A_IW_GRDH_1SDV_20160202T104519_20160202T104544_009766_00E46D_0A82.SAFE	
	02.02.2016	S1A_IW_GRDH_1SDV_20160202T104544_20160202T104609_009766_00E46D_5CED.SAFE S1A_IW_GRDH_1SSV_20160226T104518_20160226T104543_010116_00EEA2_CA3B.SAFE	
	26.02.2016	S1A_IW_GRDH_1SSV_20160226T104543_20160226T104608_010116_00EEA2_CD63.SAFE	
	ASC 120	18.03.2015	S1A_IW_GRDH_1SSV_20150318T232644_20150318T232709_005092_006673_BAEC.SAFE S1A_IW_GRDH_1SSV_20150318T232709_20150318T232734_005092_006673_DFE0.SAFE
		05.05.2015	S1A_IW_GRDH_1SSV_20150505T232646_20150505T232711_005792_00771F_ODD1.SAFE S1A_IW_GRDH_1SSV_20150505T232711_20150505T232736_005792_00771F_850A.SAFE
		22.06.2015	S1A_IW_GRDH_1SSV_20150622T232655_20150622T232720_006492_0089D0_C153.SAFE S1A_IW_GRDH_1SSV_20150622T232720_20150622T232745_006492_0089D0_8395.SAFE
		16.07.2015	S1A_IW_GRDH_1SSV_20150716T232655_20150716T232720_006842_00938A_C6B1.SAFE S1A_IW_GRDH_1SSV_20150716T232720_20150716T232745_006842_00938A_1F79.SAFE
		02.09.2015	S1A_IW_GRDH_1SSV_20150902T232657_20150902T232722_007542_00A6D4_0F9B.SAFE S1A_IW_GRDH_1SSV_20150902T232722_20150902T232747_007542_00A6D4_7DB7.SAFE
		26.09.2015	S1A_IW_GRDH_1SSV_20150926T232658_20150926T232723_007892_00B037_50B6.SAFE S1A_IW_GRDH_1SSV_20150926T232723_20150926T232748_007892_00B037_AF5E.SAFE
		20.10.2015	S1A_IW_GRDH_1SSV_20151020T232658_20151020T232723_008242_00B9B8_0CB3.SAFE S1A_IW_GRDH_1SSV_20151020T232723_20151020T232748_008242_00B9B8_A9B9.SAFE
		13.11.2015	S1A_IW_GRDH_1SSV_20151113T232653_20151113T232718_008592_00C30E_584A.SAFE S1A_IW_GRDH_1SSV_20151113T232718_20151113T232718_008592_00C30E_BCB1.SAFE
		07.12.2015	S1A_IW_GRDH_1SSV_20151113T232718_20151113T232743_008592_00C30E_B464.SAFE S1A_IW_GRDH_1SSV_20151113T232718_20151113T232743_008592_00C30E_D663.SAFE
31.12.2015		S1A_IW_GRDH_1SSV_20151207T232652_20151207T232717_008942_00CCEB_C926.SAFE S1A_IW_GRDH_1SSV_20151207T232717_20151207T232742_008942_00CCEB_8E25.SAFE	
			S1A_IW_GRDH_1SSV_20151231T232651_20151231T232716_009292_00D6B8_20DB.SAFE

	S1A_IW_GRDH_1SSV_20151231T232716_20151231T232741_009292_00D6B8_82F2.SAFE
24.01.2016	S1A_IW_GRDH_1SSV_20160124T232650_20160124T232715_009642_00E0D8_EF8E.SAFE
	S1A_IW_GRDH_1SSV_20160124T232715_20160124T232740_009642_00E0D8_490C.SAFE
17.02.2016	S1A_IW_GRDH_1SSV_20160217T232650_20160217T232715_009992_00EB0D_9338.SAFE
	S1A_IW_GRDH_1SSV_20160217T232715_20160217T232740_009992_00EB0D_D046.SAFE
12.03.2016	S1A_IW_GRDH_1SSV_20160312T232650_20160312T232715_010342_00F51C_855C.SAFE
	S1A_IW_GRDH_1SSV_20160312T232715_20160312T232740_010342_00F51C_84B9.SAFE

Table 0-2: Acquired Sentinel-2 Scenes

Date	Grid ID	Scene ID
22.10.2015	18MMU	S2A_OPER_PRD_MSIL1C_PDMC_20160413T132734_R025_V20151022T152922_20151022T152922.SAFE
11.12.2015	18MMU	S2A_OPER_PRD_MSIL1C_PDMC_20151211T221758_R025_V20151211T153732_20151211T153732.SAFE
10.01.2016	18MMU	S2A_OPER_PRD_MSIL1C_PDMC_20160111T025529_R025_V20160110T153727_20160110T153727.SAFE
10.03.2016	18MMU	S2A_OPER_PRD_MSIL1C_PDMC_20160311T185157_R025_V20160310T152711_20160310T152711.SAFE

Table 0-3: Acquired Landsat 8 Scenes

Date	Grid ID	Image ID
20.04.2013	008-064	LC80080642013110-SC20160704054647
06.05.2013	008-064	LC80080642013126-SC20160704053554
26.06.2013	008-064	LC80080642013174-SC20160704055420
11.09.2013	008-064	LC80080642013254-SC20160704055606
27.09.2013	008-064	LC80080642013270-SC20160704060138
29.10.2013	008-064	LC80080642013302-SC20160704055242
26.06.2014	008-064	LC80080642014177-SC20160704060546
12.07.2014	008-064	LC80080642014193-SC20160704055442
30.09.2014	008-064	LC80080642014273-SC20160704055358
19.12.2014	008-064	LC80080642014353-SC20160704060640
25.03.2015	008-064	LC80080642015084-SC20161019110407
13.06.2015	008-064	LC80080642015164-SC20160704055553
29.06.2015	008-064	LC80080642015180-SC20160704054905
31.07.2015	008-064	LC80080642015212-SC20160704061238
16.08.2015	008-064	LC80080642015228-SC20160704060901
17.09.2015	008-064	LC80080642015260-SC20160704061237
20.11.2015	008-064	LC80080642015324-SC20160704055841
06.12.2015	008-064	LC80080642015340-SC20160704060018
23.01.2016	008-064	LC80080642016023-SC20160704055524

GABON

Table 0-4: Acquired Sentinel-1 Scenes

ASC/DSC ORBIT NR	DATE	IMAGE ID
	03.01.2016	S1A_IW_GRDH_1SDV_20160103T045846_20160103T045911_009325_00D7A7_18D3
	15.01.2016	S1A_IW_GRDH_1SDV_20160115T045845_20160115T045910_009500_00DCA8_F104
	27.01.2016	S1A_IW_GRDH_1SDV_20160127T045845_20160127T045910_009675_00E1CA_DB20
	08.02.2016	S1A_IW_GRDH_1SDV_20160208T045845_20160208T045910_009850_00E6CC_933A
	22.02.2016	S1A_IW_GRDH_1SDV_20160220T045845_20160220T045910_010025_00EBFC_826E
	27.03.2016	S1A_IW_GRDH_1SDV_20160327T045845_20160327T045910_010550_00FAE6_A212
	08.04.2016	S1A_IW_GRDH_1SDV_20160408T045846_20160408T045911_010725_01000B_187D
	02.05.2016	S1A_IW_GRDH_1SDV_20160502T045847_20160502T045912_011075_010AD8_8A03
	14.05.2016	S1A_IW_GRDH_1SDV_20160514T045847_20160514T045912_011250_011064_5738
	26.05.2016	S1A_IW_GRDH_1SDV_20160526T045848_20160526T045913_011425_011623_F66E
	01.07.2016	S1A_IW_GRDH_1SDV_20160701T045850_20160701T045915_011950_0126BF_B387
	12.07.2016	S1A_IW_GRDH_1SDV_20160713T045850_20160713T045915_012125_012C7A_0A6F
DSC 153	25.07.2016	S1A_IW_GRDH_1SDV_20160725T045851_20160725T045916_012300_01322E_A0E4
	06.08.2016	S1A_IW_GRDH_1SDV_20160806T045852_20160806T045917_012475_013801_44DA
	18.08.2016	S1A_IW_GRDH_1SDV_20160818T045853_20160818T045918_012650_013DC2_AF35
	30.08.2016	S1A_IW_GRDH_1SDV_20160830T045853_20160830T045918_012825_0143AE_EC08
	11.09.2016	S1A_IW_GRDH_1SDV_20160911T045854_20160911T045919_013000_014952_9869
	23.09.2016	S1A_IW_GRDH_1SDV_20160923T045854_20160923T045919_013175_014F21_2E1B
	05.10.2016	S1A_IW_GRDH_1SDV_20161005T045854_20161005T045919_013350_0154AE_C11C
	17.10.2016	S1A_IW_GRDH_1SDV_20161017T045854_20161017T045919_013525_015A3A_7631
	29.10.2016	S1A_IW_GRDH_1SDV_20161029T045854_20161029T045919_013700_015FA1_6952
	10.11.2016	S1A_IW_GRDH_1SDV_20161110T045854_20161110T045919_013875_016524_CEED
	22.11.2016	S1A_IW_GRDH_1SDV_20161122T045854_20161122T045919_014050_016A7B_C0A9
	04.12.2016	S1A_IW_GRDH_1SDV_20161204T045853_20161204T045918_014225_016FEC_94DD
	16.12.2016	S1A_IW_GRDH_1SDV_20161216T045853_20161216T045918_014400_01757B_A0AB
	28.12.2016	S1A_IW_GRDH_1SDV_20161228T045853_20161228T045918_014575_017AE9_45B8

Table 0-5: Acquired Sentinel-2 Scenes

DATE	GRID ID	IMAGE ID
08.01.2016	32MPD	S2A_OPER_PRD_MSIL1C_PDMC_20160108T175823_R136_V20160108T095223_20160108T095223
18.01.2016	32MPD	S2A_OPER_PRD_MSIL1C_PDMC_20160119T094555_R136_V20160118T095223_20160118T095223
07.02.2016	32MPD	S2A_OPER_PRD_MSIL1C_PDMC_20160207T181735_R136_V20160207T094351_20160207T094351
17.02.2016	32MPD	S2A_OPER_PRD_MSIL1C_PDMC_20160217T191230_R136_V20160217T094917_20160217T094917
06.06.2016	32MPD	S2A_OPER_PRD_MSIL1C_PDMC_20160607T074059_R136_V20160606T094258_20160606T094258
16.06.2016	32MPD	S2A_OPER_PRD_MSIL1C_PDMC_20160617T165514_R136_V20160616T094328_20160616T094328
16.07.2016	32MPD	S2A_OPER_PRD_MSIL1C_PDMC_20160716T164111_R136_V20160716T094301_20160716T094301
26.07.2016	32MPD	S2A_OPER_PRD_MSIL1C_PDMC_20160726T222227_R136_V20160726T095054_20160726T095054
05.08.2016	32MPD	S2A_OPER_PRD_MSIL1C_PDMC_20160805T162553_R136_V20160805T094623_20160805T094623
13.12.2016	32MPD	L1C_T32MPD_A007712_20161213T094709

Table 0-6: Acquired Landsat 8 Scenes

DATE	GRID ID	IMAGE ID
15.01.2016	185-061	LC81850612016015-SC20161215091803
16.02.2016	185-061	LC81850612016047-SC20161215093130
04.04.2016	185-061	LC81850612016095-SC20161215093841
20.04.2016	185-061	LC81850612016111-SC20161215093136
06.05.2016	185-061	LC81850612016127-SC20161215090707
25.07.2016	185-061	LC81850612016207-SC20161215091521
27.09.2016	185-061	LC81850612016271-SC20161215091450
13.10.2016	185-061	LC081850612016101301T2-SC20170719163624
16.12.2016	185-061	LC081850612016121601T2-SC20170719170212